DOE/EC/41187-1

DEVELOPMENT, EXPERIMENTAL VALIDATION, AND APPLICATION OF ADVANCED COMBUSTION SPACE MODELS FOR GLASS MELTING FURNACES

Final Report

Brent W. Webb and Mardson Q. McQuay
Brigham Young University
Provo, UT 84602

DOE Patent Clearance Granted
Mark P. Dvorscak
(630) 252-2393
E-mail: mark.dvorscak@ch.doe.gov
Office of Intellectual Property Law
DOE Chicago Operations Office
Oct 22, 2002
Date

Prepared for
The United States Department of Energy
Under Cooperative Agreement DE-SC02-95CE41122

DISCLAIMER

This report was prepared as an account of work sponsored by an agency of the United States Government. Neither the United States Government nor any agency thereof, nor any of their employees, makes any warranty, express or implied, or assumes any legal liability or responsibility for the accuracy, completeness, or usefulness of any information, apparatus, product, or process disclosed, or represents that its use would not infringe privately owned rights. Reference herein to any specific commercial product, process, or service by trade name, trademark, manufacturer, or otherwise does not necessarily constitute or imply its endorsement, recommendation, or favoring by the United States Government or any agency thereof. The views and opinions of authors expressed herein do not necessarily state or reflect those of the United States Government or any agency thereof.

DISCLAIMER

Portions of this document may be illegible in electronic image products. Images are produced from the best available original document.

Development, Experimental Validation, and Application of Advanced Combustion Space Models for Glass Melting Furnaces

Final Report

Brent W. Webb and Mardson Q. McQuay
Brigham Young University
Provo, UT 84602

Prepared for
The United States Department of Energy
Under Contract No. DE-SC02-95CE41122

Executive Summary

This final report, extensive and comprehensive in nature, documents the accomplishments and contributions of the work performed under DOE contract number DE-SC02-95CE41122 from October 1995 to June 2001. The work was administered and performed at Brigham Young University and The Ford Motor Company Glass Division (subsequently Visteon), was the industrial partner. The objectives of this study were to (1) obtain detailed measurements in the combustion space of an operating industrial furnace, (2) create an advanced furnace model and use the experimental measurements to evaluate the model, and (3) apply the model to other technologies of interest, such as oxygen-firing and staged combustion. In terms of organization, Section 2 will summarize the experimental work results, including measurements before and after the Ford furnace rebuild of local gas temperature, gas composition, gas velocity, radiant heat flux, and glass surface temperature. Section 3 includes results from the modeling effort. The modeling work was initially focused on the combustion space only. In that context, modeling of a port module was first done, followed by two adjacent port modules, and eventually the numerical simulation of a full combustion chamber. Given the sensitivity of the combustion space modeling results to several of the assumed boundary conditions, the modeling work was then extended to a fully coupled model, simulating the combustion space, the glass tank, and the batch melting processes. All of these modeling results will be reported in Section 3, including an extensive comparison of the model predictions with the experimental data. Finally, Section 4 will report on the technology transfer accomplishments of the project. Section 5 summarizes the work and draws several conclusions regarding the effort.

TABLE OF CONTENTS

Executive Summary iii
List of Figures iv
List of Tables ix

1. INTRODUCTION AND OBJECTIVES 1
2. EXPERIMENTS 1
2.1 Pre-Rebuild Combustion Space Measurements 2
2.1.1 Furnace Description 2
2.1.2 Instrumentation 5
2.1.3 Steady-State Measurements 9
2.1.4 Transient Measurements 16
2.1.5 Symmetry Evaluation 19
2.2 Pre- and Post-Rebuild Comparison: Inlet and Exhaust 19
2.2.1 Gas Composition 21
2.2.2 Gas Temperature 26
2.2.3 Gas Velocity 29
2.3 Surface Temperature 32
2.3.1 Instrumentation 32
2.3.2 Physical Phenomena 37
2.3.3 Time-Averaged Measurements 39
2.3.4 Time-Resolved Measurements 40
2.4 Crown Flux 43
2.4.1 Instrumentation 43
2.4.2 Time-Averaged Measurements 45
2.4.3 Non-Firing Measurements 47
2.4.4 Time-Resolved Measurements 47
3. MODELING 53
3.1 Combustion Space 53
3.1.1 Port Module Simulations 54
3.1.2 Full Furnace Simulations 70
3.2 Coupled Modeling 73
3.2.1 Overall Model Methodology 74
3.2.2 Model Enhancements 99
4. TECHNOLOGY TRANSFER 123
4.1 Ford Float Glass Furnace 123
4.2 Fiberglass Unit Melter Furnace 123
4.3 Container Glass Furnace 123
5. CONCLUSIONS 127
6. ACKNOWLEDGMENTS 128
7. REFERENCES 128

List of Figures

Figure 1 Schematic of the side-port, gas-fired, industrial flat-glass furnace where measurements were made and which was simulated by numerical models....3

Figure 2 Schematic showing top and side views of port 3 in the furnace....4

Figure 3 Schematic of the ellipsoidal hemispherical radiometer used for crown incident radiant heat flux measurements....8

Figure 4 Contour plots of gas velocity in the combustion space of the furnace: (a) S-N firing configuration; and (b) N-S firing configuration....10

Figure 5 Gas temperature profiles for access holes 1 and 2 in the combustion space of the furnace for N-S and S-N firing configurations....11

Figure 6 Concentration profiles of major species in the combustion space of the furnace for N-S firing configuration: (a) O_2; (b) CO; and (c) CO_2....13

Figure 7 Concentration profiles of major species in the combustion space of the furnace for S-N firing configuration: (a) O_2; (b) CO; and (c) CO_2....15

Figure 8 Radiant heat flux profile in the combustion space of the furnace for N-S and S-N firing configurations....17

Figure 9 Time-dependent furnace and portneck measurements: (a) velocity, (b) species concentration, and (c) temperature....18

Figure 10 Comparison of portneck O_2 concentration profiles for S-N firing configuration (exhaust) before and after the furnace rebuilding....22

Figure 11 Comparison of portneck CO concentration profiles for S-N firing configuration (exhaust) before and after the furnace rebuilding....23

Figure 12 Comparison of portneck CO_2 concentration profiles for S-N firing configuration (exhaust) before and after the furnace rebuilding....24

Figure 13 Comparison of inlet (N-S firing configuration) and exhaust (S-N firing configuration) gas temperature measurements by port (port 1 is near the batch) before and after the furnace rebuilding....28

Figure 14 Comparison of portneck gas velocity profiles for N-S firing configuration (inlet) before and after the furnace rebuilding....30

Figure 15 Photographs of a typical port (a) before and (b) after the furnace rebuilding....31

Figure 16 Schematics of the two-color pyrometer instrument used for optical glass surface temperature measurements (figure a) and of the detector detail (figure b) 34

Figure 17 Axial profile of net heat flux on the batch/glass surface imposed as boundary conditions in the numerical simulations.....38

Figure 18 Schematic (plan view) of the glass surface in the furnace based on information obtained from specialized video data and visual observations through furnace inspection ports, indicating bubbler location and estimated spring zone position 40

Figure 19 Comparison of measured and predicted average glass surface temperature profile along the furnace axial centerline in the glass tank.....42

Figure 20 Typical time-resolved surface temperature plots acquired during reversal in locations nos. 1, 3, 4, 5 and 6.....44

Figure 21 Schematic of the circular foil radiometer used for crown incident radiant heat flux measurements.....46

Figure 22 Contour plot of the furnace glass surface temperatures used as a boundary condition in the base case numerical simulation.....48

Figure 23 Comparison of measured and predicted average crown incident radiant heat flux along the axial centerline of the furnace during firing cycles.....49

Figure 24 Comparison of time-averaged crown incident radiant heat flux measurements acquired during firing and non-firing periods using the circular foil radiometer.....50

Figure 25 Average firing cycle variation (standard deviation) of measured crown incident radiant heat flux at all crown access locations 52

Figure 26 Cycle variation of measured crown incident radiant heat flux measured with the ellipsoidal radiometer at Location 4 for both firing directions over an entire firing cycle period.....57

Figure 27 Typical time-resolved data of measured crown incident radiant heat flux at several locations during non-firing reversal periods.....59

Figure 28 Schematic representation of the single portneck model 60

Figure 29 Comparison of measured and predicted *u*-velocities in holes 2, 4 and 6.....61

Figure 30 Comparison of measured and predicted gas temperatures in holes 1 and 2 for the north-south firing configuration.....63

Figure 31 Comparison of measured and predicted oxygen concentrations (vol % dry) in holes 2, 4 and 6 64

Figure 32 Comparison of measured and predicted CO concentrations (ppm dry) in holes 2, 4 and 6 65

Figure 33 Comparison of measured and predicted CO_2 concentrations (vol % dry) in holes 2, 4 and 6 69

Figure 34 Comparison of the predicted and measured incident flux on the crown 71

Figure 35 Schematic illustration of the oxygen lance geometry 72

Figure 36 Schematic illustration of oxy/fuel-fired full furnace simulation 77

Figure 37 Schematic illustration of the batch-melting model 79

Figure 38 Velocity vector plots from the glass tank numerical model with and without bubblers in a vertical plane in the tank along the furnace axial centerline 80

Figure 39 Surface velocity vector plots from the glass tank numerical model with and without bubblers 82

Figure 40 Information flow for the coupled solution 84

Figure 41 Predicted glass surface temperature distribution 86

Figure 42 Predicted and measured incident radiative heat flux on the crown 87

Figure 43 Predicted glass surface velocity distribution 88

Figure 44 Predicted and measured profiles of glass/batch surface temperature and crown temperature along the furnace centerline 89

Figure 45 Predicted gas temperature profile in the combustion chamber (100% firing) 94

Figure 46 Predicted gas velocity profiles in the combustion chamber (100% firing) 95

Figure 47 Predicted heat flux distribution from the combustion space to the surface of batch and glass melt (100% firing) 96

Figure 48 Predicted NO_x distribution in the combustion chamber (100% firing) 97

Figure 49 Predicted temperature profile on the glass surface (100% firing) 98

Figure 50 Predicted crown temperatures at the center of the furnace 100

Figure 51 Predicted glass surface temperatures at the center of the tank.....101

Figure 52 Predicted glass bottom temperature at the center of the tank.....102

Figure 53 Predicted gas temperature at the fuel inlet plane with soot radiation included.....103

Figure 54 Predicted net flux to the glass/batch surface with soot radiation included.....107

Figure 55 Predicted glass surface temperatures: (a) without soot (b) with soot.....108

Figure 56 Predicted and measured crown incident radiation flux along the furnace centerline...109

Figure 57 Predicted and measured crown temperature.....110

Figure 58 Predicted and measured glass and batch surface temperature along the furnace centerline.....111

Figure 59 Predicted batch coverage.....112

Figure 60 Predicted batch boundary location for different batch coverage fractions in the batch island zone.....114

Figure 61 Predicted gas temperature distribution in the combustion space at the fuel inlet horizontal plane (85% batch coverage in the batch island zone).....115

Figure 62 Predicted heat flux distribution from the combustion space to the batch and glass melt surfaces (85% batch coverage in the batch island zone).....116

Figure 63 Predicted glass/batch surface temperature distribution (85% batch coverage in the batch island zone).....117

Figure 64 A comparison of predicted and measured glass surface temperatures along the furnace centerline for different batch coverage fractions in the batch island zone (● – experimental data, curve 1 – 80% batch fraction, curve 2 – 85% batch fraction, curve 3 – 90% batch fraction, and curve 4 – 100% batch fraction). Inset panel: Predicted average furnace exhaust temperature as a function of batch coverage fraction in the batch island zone.....118

Figure 65 Predicted velocity vectors on the glass surface (85% batch coverage in the batch island zone).....120

Figure 66 A comparison of predicted and measured crown incident radiation fluxes along the furnace centerline for different batch coverage fractions in the batch island zone (● – experimental data, curve 1 – 80% batch fraction, curve 2 – 85% batch fraction, curve 3 – 90% batch fraction, and curve 4 – 100% batch fraction). Inset panel: Predicted total

heat transfer to batch and melt as a function of batch coverage fraction in the batch island zone 121

Figure 67 A comparison of predicted and measured crown temperatures along the furnace centerline for different batch coverage fractions in the batch island zone (● – experimental data, curve 1 – 80% batch fraction, curve 2 – 85% batch fraction, curve 3 – 90% batch fraction, and curve 4 – 100% batch fraction) 122

Figure 68 Schematic of fiberglass unit melter furnace modeled 124

Figure 69 Schematic of side-charging container glass furnace modeled 125

Figure 70 Illustration of batch feed model modification made for side-charging container glass furnace coupled model 126

List of Tables

Table 1 Furnace operating conditions before and after rebuild....6

Table 2 Evaluation of combustion symmetry....20

Table 3 Combustion analysis based on fuel flow and oxygen and carbon dioxide dry-basis concentration measurements....27

Table 4 Inlet flowrates and temperatures....33

Table 5 Major characteristics of PCGC-3 and FLUENT codes....55

Table 6 Boundary and inlet conditions for the base case model....56

Table 7 Summary of predicted figures of merit for the NO_x reduction technologies studied....68

Table 8 Predicted and measured exhaust compositions....91

Table 9 Inlet natural gas and oxygen flowrates....91

Table 10 Predicted mass percentages of exhaust gas at outlet openings....93

Table 11 Predicted average heat flux and total heat transfer from combustion space to batch blanket....93

Table 12 Predicted average heat flux and total heat transfer from combustion space to glass melt surface....93

Table 13 Predicted exhaust gas variables....93

Table 14 Predicted and measured oxygen concentration....106

Table 15 Predicted and measured carbon dioxide concentration....106

1. INTRODUCTION AND OBJECTIVES

The optimum design of industrial furnaces has become increasingly important from both environmental and economic standpoints. The competing requirements of high efficiency and low emissions are certainly present with glass furnaces.

Glass furnace design is relying increasingly on three-dimensional, numerical modeling of both the combustion space and the glass melt tank to help achieve these requirements. This growing reliance is demonstrated by a large number of recent publications on the subject (Boerstoel *et al.*, 1994, 1995; Carvalho, 1983; Carvalho and Lockwood, 1985, 1990; Carvalho and Nogueira, 1994, 1995a, 1995b; Carvalho *et al.*, 1987, 1988, 1990, 1992, 1995a, 1995b, 1996, 1997a, 1997b, 1997c; Chen and Goodson, 1980; Gosman *et al.*, 1980, 1982, 1995; Hill *et al.*, 2000; Mase and Oda, 1980; McConnell and Goodson, 1979; Megahed, 1978; Novak, 1980; Post, 1988; Semião, 1986; Wang, 1998; Wang *et al.*, 1997a, 1997b, 1997c, 1998b, 1999a, 1999b, 2000a, 2000b).

Unfortunately, the evaluation of numerical glass furnace models is limited by the lack of practical furnace data (Cassiano *et al.*, 1994; Farmer *et al.*, 1992; Victor *et al.*, 1991; Costa *et al.*, 1996). Detailed profile measurements of gas composition, heat flux, gas temperature, gas velocity, wall temperature, and glass surface temperature in the combustion space are needed to demonstrate the modeling technologies and bring them to a state of development where they can be used confidently for furnace design. The objectives of this study were to (1) obtain detailed measurements in the combustion space of an operating industrial furnace, (2) create an advanced furnace model and use the experimental measurements to evaluate the model, and (3) apply the model to other technologies of interest, such as oxygen-firing and staged combustion.

In this document we will report extensively on the main accomplishments and contributions of the worked funded by DOE under contract number DE-SC02-95CE41122. In terms of organization, Section 2 will summarize the experimental work results, including measurements before and after the Ford furnace rebuild. Section 3 includes results from the modeling effort. The modeling work was initially focused on the combustion space only. In that context, modeling of a port module was first done, followed by two adjacent port modules, and eventually the numerical simulation of a full combustion chamber. Given the sensitivity of the combustion space modeling results to several of the assumed boundary conditions, the modeling work was then extended to include a coupled model, simulating the combustion space, the glass tank, and the batch in an iterative and coupled fashion. All of these modeling results will be reported in Section 3, including an extensive comparison of the model predictions with the experimental data. Finally, Section 4 will report on the technology transfer accomplishments of the project.

2. EXPERIMENTS

The experimental effort was an important part of this study, providing important experimental data to be used for validation of the numerical models as well as improved understanding of the complex thermal phenomena in glass furnaces. Variables measured in this study included local gas temperature, gas composition, gas velocity, wall incident heat flux, and glass surface temperature.

These measurements were obtained in several tests in the Ford glass plant in Tulsa, OK. A summary of the main findings of this experimental effort is presented in this section of the report. Limited measurements of gas temperature and composition and wall incident radiant heat flux through six observation ports in the wall of an end-port, oil-fired, regenerative, container-glass furnace were reported by Cassiano *et al.* (1994). Two operating conditions were tested to investigate the effects of throughput and air/fuel ratio. The cyclic operation and three-dimensional nature of the furnace were categorized, but no time-resolved information was given and detailed profile measurements in the combustion space were not obtained. The results of this study became the basis for a new furnace control scheme developed by Farmer *et al.* (1992) and Victor *et al.* (1991). Similar measurements were reported by Costa, *et al.* (1996) in a similar furnace.

In the present study, both pre- and post-rebuild measurements were obtained in an industrial-scale, flat glass furnace. Prior to rebuild, the crown of the furnace was core-drilled to provide access for detailed profile measurements of velocity, temperature, and species concentration (O_2, CO, and CO_2), wall incident radiative heat flux, and glass surface temperature in the combustion space. Similar measurements were also made in the portnecks both before and after rebuild. The measurements have provided the most complete set of practical evaluation data for glass furnace modeling available.

2.1 Pre-Rebuild Combustion Space Measurements

The timing of this study agreed very well with the rebuilding schedule of one of the Ford furnaces in Tulsa, OK. This allowed us to make measurements before the furnace was taken apart (measurements reported in this section of the report) and after the furnace was rebuilt (measurements reported in Section 2.2). In order to avoid unnecessary repetition, all the information common to both studies, such as furnace description, applicable instrumentation, etc., is presented only in this section of the report

2.1.1 Furnace Description

A schematic of a side-port, 550-ton/day, gas-fired, flat-glass furnace is shown in Figure 1. It was approximately 2.6 m high from the glass line to the maximum height of the crown, 11.0 m wide, and 21.5 m long. Regenerators were located on the north and south sides of the furnace. A set of six portnecks approximately 2.9 m long connected each regenerator to the furnace. Figure 2 shows top and side views of a typical portneck. At the regenerator opening, each portneck was nominally 1.2 m wide and 1.3 m high. At the furnace inlet, the height of each portneck narrowed to 0.6 m and the width expanded to 1.7 m. Each portneck had two 4.4-cm-diameter pipe burners of proprietary design located 81.3 cm from the edge of the furnace and 43.2 cm above the glass line. The burners were angled so that their centerlines intersected at the edge of the furnace. Other geometric details were reported elsewhere (Newbold, 1997; Newbold *et al.*, 1997; McQuay *et al.*, 2000).

The furnace operating cycle consisted of a fifteen-minute burn from the north portnecks with exhaust through the south (N-S firing direction), a reversal period (approximately 20 sec) during which no firing occurred, followed by fifteen minutes in the opposite direction (S-N firing direction), and another reversal period. Each portneck was built with one 2.54-cm-diameter access hole on top, located 1.7 m from the breast wall. Six 10.2-cm-diameter holes were core-drilled in the

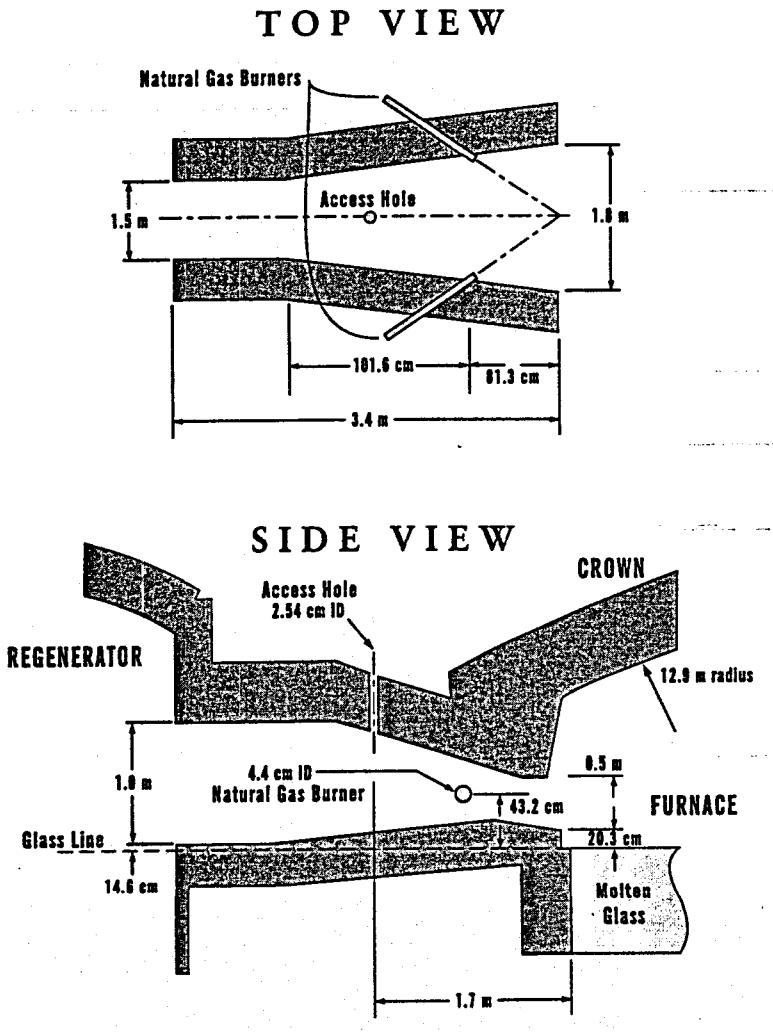

Figure 2. Schematic showing top and side views of port 3 in the furnace.

crown over the centerline of portneck 3 to provide additional access for the measurements. These holes were located at 1.1, 2.3, 3.4, 4.4, 5.3, and 7.6 m from the portneck wall and numbered 1 through 6, respectively, as shown in Figure 1. They were used for vertical insertion of probes into the combustion space. Hole 5, located 5.3 m from the portneck wall, was located just slightly off the crown centerline. Holes 3 and 6 were located equidistant from, and on opposite sides of the crown centerline and were used to evaluate flame symmetry relative to burn reversal.

Furnace operating conditions before and after rebuild are shown in Table 1. The most notable effect of the rebuild was the 17% decrease in fuel consumption. The fuel composition was obtained from the natural gas company. The percent excess air was calculated from the total fuel and air flowrates that were metered by the plant. The total fuel flowrate was the sum of individually metered flowrates for each port. The overall air flowrate was obtained using differential pressure measurements across a large orifice. The port-by-port equivalence ratios were determined by integrating measured portneck velocity data (weighted by density evaluated at the measured inlet temperature) over the portneck cross-sectional area taken from blueprints for the furnace in its new condition. Deposition of particulate matter in portnecks over the lifetime of a furnace will reduce the cross-sectional area from the design value; photographs of the aging portneck just prior to rebuild revealed that the area used in the flowrate calculation may be too high by as much as 15%. The portneck velocity field was assumed to be horizontally uniform in this air flowrate calculation. The optical temperature measurements were made through an access hole in the side of the regenerator coinciding with port 4. These measurements were made during the approximate 30-sec interval between flame reversals when no flame was present.

2.1.2 Instrumentation

The small access holes on the portnecks prevented the use of conventional, L-shaped Pitot tubes for measuring gas velocity. Therefore, a special, straight, stainless steel Pitot tube was designed. The instrument consisted of a 22.2-mm-o.d., 3-m-long, water-cooled, annular tube with two 3.2-mm-o.d. tubes running lengthwise through the probe to pressure taps at the end of the probe. The pressure taps were located 5.1 cm from the end of the probe (two probe diameters) and spaced circumferentially 70 degrees apart. The pressure taps were connected to a lightweight, differential pressure transducer. This transducer produced voltage proportional to the differential pressure; the voltage was measured by a hand-held voltmeter capable of averaging the incoming signal. The signal was sampled long enough (typically one minute) to obtain a true representation of the average.

Since the probe was not of conventional design, it was calibrated against a standard Pitot tube and manometer in a wind tunnel. The flow in the wind tunnel was varied through a pressure differential range of 0 to 75 Pa, corresponding to pressure differences anticipated in the furnace. The pressure difference and corresponding voltage output were recorded for both the standard Pitot tube and the probe. From the measured voltage and pressure differentials, a linear calibration curve was determined for the probe. Velocity measurements at the same location and conditions were repeatable to ±10%. Uncertainty in the mean velocities was estimated to be ±10% in the primary flame jet near the glass, but it may be significantly higher in the recirculation zone near the crown where reversing flow and low velocities were found. Repeated velocity profiles made at port 3 on different days were identical to within ±5%.

Table 1. Furnace operating conditions before and after rebuild.

Fuel Composition (vol %)	*Before Rebuild*	*After Rebuild*
Methane	87.49	87.49
Nitrogen	6.79	6.79
Ethane	0.77	0.77
Propane	0.58	0.58
Carbon dioxide	0.58	0.58
Oxygen	0.46	0.46
Hexane	0.10	0.10
n-Butane	0.08	0.08
i-Butane	0.05	0.05
n-Pentane	0.02	0.02
Fuel density at STP	0.819 kg/m^3	0.819 kg/m^3
Fuel molecular weight	18.34 kg/kmol	18.34 kg/kmol
Molar stoichiometric air/fuel ratio	9.42	9.42
Plant measured flowrates (kg/h)		
Fuel (sum of individual ports)	3,496	2,886
Air	87,800	55,400
Excess air based on plant-measured values	70%	30%
Species generation from melt (kg/h)		
CO_2	2,500	2,500
H_2O	600	600

Combustion gases were sampled by drawing them through a water-cooled, stainless steel collection probe using a four-head suction pump. The probe was made of a 22.2-mm-o.d., 3-m-long annular tube with a 9.5-mm suction tube on the inside. The gases were rapidly quenched upon being drawn into the tube due to the high water cooling rate in the surrounding annulus. The gases were analyzed in real-time with a NOVA 301-BD for CO_2, Land Combustion 5500/6500 units for O_2 and CO, and a North American Enviromate for duplicate O_2 and CO measurements. The NOVA instrument used an infrared absorption technique, while the Land Combustion and North American units had electrochemical cells. All analyzers were calibrated repeatedly using gas standards for O_2, CO_2, and CO. The reported accuracies were ±0.05% for O_2, ±0.3% for CO_2, and ±4% and ±100 ppm for CO measurements greater than and less than 2000 ppm, respectively. Good agreement was observed throughout the tests in the duplicate measurements. Response times for species measurements were estimated for the sample train used in the tests to be less than 2 minutes for CO_2 and 15 seconds for other species. Repeatability of species concentrations measurements was ±5%.

Gas temperature was measured using a conventional, triply shielded, water-cooled, suction pyrometer. The pyrometer consisted of a 63-mm-o.d., 4-m-long, water-cooled annular tube with a 27-mm-o.d., 18-cm-long, triple-walled, alumina radiation shield affixed to the end. Gas suction was provided with a venturi pump attached to a 2.54-cm-diameter pressure line at 550 kPa. The thermocouple voltage was measured with a Type-S, cold-junction compensator and amplifier using a hand-held voltmeter. A ninth-order polynomial was used to describe the thermocouple temperature as a function of the voltage output. The accuracy of the pyrometer was reported to be ±8 K. Temperature measurements were made approximately 2.3 m from where concentration measurements were made in the portnecks. By angling the suction pyrometer up and down, measurements were possible at several locations over a vertical distance of approximately 0.5 m across the exhaust area. All measurements were within 8 K of each other, suggesting that the flow of combustion products in the exhaust portnecks was nearly isothermal. Further information may be found elsewhere (Newbold *et al.*, 1997; Butler and Webb, 1991; Butler, 1992).

A hemispherical, ellipsoidal radiometer was used to characterize incident radiant heat flux on the crown. A schematic is shown in Figure 3. The radiometer consisted of a stainless steel, water-cooled jacket, 43 mm in diameter and 0.65 m long, encasing an inner signal wire tube with the detector head mounted in one end, and cooling water and signal lead connections at the opposite end. The radiometer was also equipped with a purge gas tube that allowed for a flow of dry nitrogen to exit the ellipsoidal cavity at the detector face to prevent fouling of the ellipsoidal reflective surface by particulate or condensation during use. The ellipsoidal detector head was designed to measure the total hemispherical radiant heat flux over the full infrared spectrum incident at the detector face. The ellipsoidal radiometer was calibrated to ±5% accuracy up to approximately 300 kW/m^2; above this range the manufacturer indicated that the linear calibration curve could be extrapolated, but that the extrapolated value might be low. The ellipsoidal radiometer required 2-3 minutes to come up to temperature after insertion into the furnace. After reaching this level, the detector had a faster response to incremental changes in heat flux, nominally 30-60 seconds. This instrument was therefore most useful for collecting time-averaged data, and only capable of measuring time-resolved trends over several minutes or more.

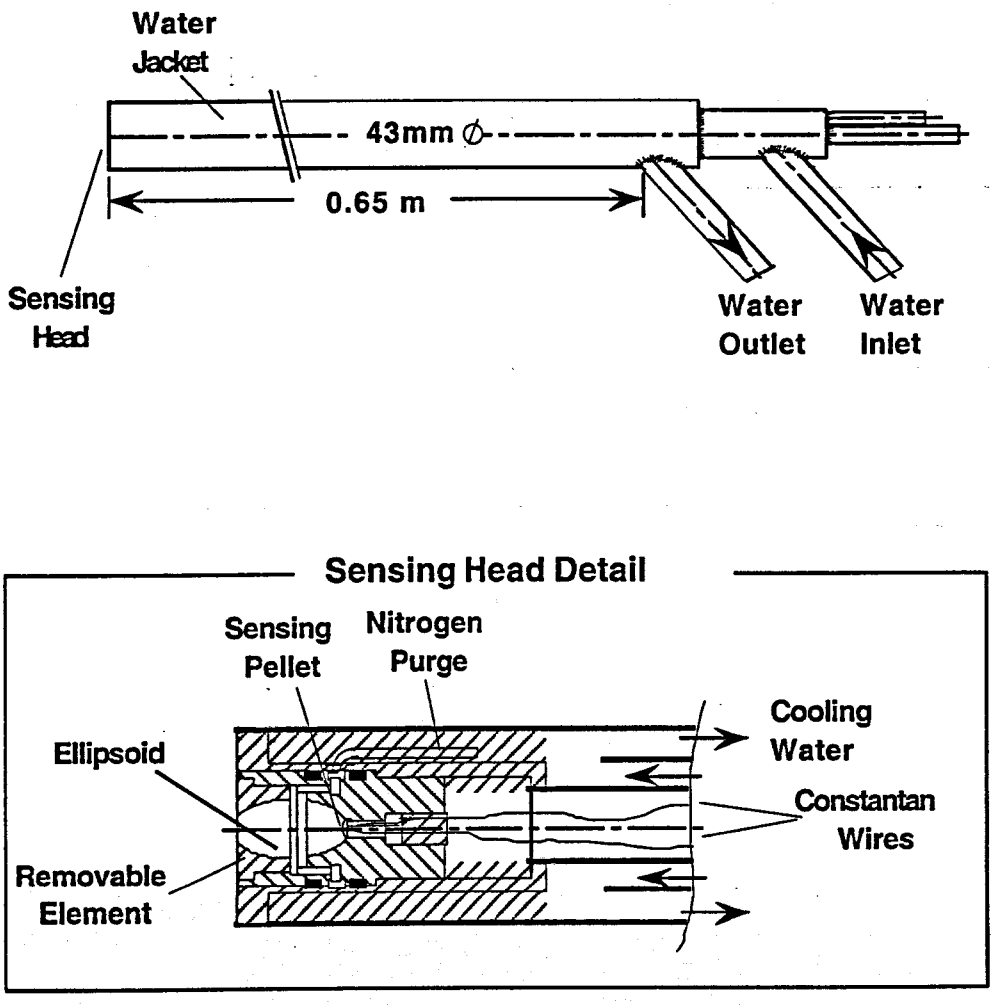

Figure 3. Schematic of the ellipsoidal hemispherical radiometer used for crown incident radiant heat flux measurements.

When performing the measurements, water-cooling and purge gas flows were established prior to positioning the instrument detector face inside the combustion space. The probe was then inserted through each of the crown access holes with the instrument normal to the glass surface, and the steady-state voltage output was recorded. The ellipsoidal cavity was inspected between measurements to ensure that the mirror was not fouled and to determine if the purge gas flow was adequate.

2.1.3 Steady-State Measurements

The horizontal component of gas velocity along the centerline of portneck 3 is shown in Figure 4. The figure shows two vector plots constructed from the Pitot tube measurements. Figure 4a shows velocities when the burners are firing in the S-N direction, and 3b shows velocities in the N-S direction. For the N-S direction, the location of the core-drilled holes permitted study of the root and central portions of the flame jet. The tail of the flame was studied in the S-N configuration. The plots show data for holes 2 through 6. After limited probing (temperature data only), the ceramic plug used to seal hole 1 fused with the crown refractory, preventing further access to the combustion space through this hole.

The highest velocities in the flame jet seen in Figure 4 are near the glass surface. Here the magnitudes of the axial velocity component exceeded 20 m/s. The portneck was vectored downward approximately 16 degrees, directing the air/fuel jet onto the glass surface. As the flame moved across the combustion space, the velocity immediately increased from the portneck exit value of approximately 11 m/s to a maximum, then decreased. This rapid increase in velocity followed by a decrease was due to ignition followed by heat loss.

A large recirculation zone is evident in the upper portion of the furnace for both firing directions. Reverse flow velocities in this region were found to reach magnitudes as high as 3.5 m/s. While it is difficult to clearly identify the zero-velocity streamline separating the flame jet and the relatively stagnant recirculation zone, the data suggest that the reverse flow occupied a region approximately within the crown arc. As will be shown later, the recirculation zone had an impact on both species concentrations and temperature.

Figure 5 shows the measured temperature profiles in holes 1 and 2 in the combustion space for both firing configurations. Temperature data were obtained only in holes 1 and 2 because *i*) high heat fluxes to the large-diameter suction pyrometer prohibited probing in the high-temperature region of the flame jet due to cooling water constraints, and *ii*) at the temperatures encountered in hole 2, the ceramic radiation shields softened and collapsed, eventually fusing together. Furthermore, the measured temperatures approached the service ceiling of Type-S thermocouples of 2050 K. Temperatures below 0.5 m from the glass line were not measured in hole 1 due to early uncertainty in positioning the suction pyrometer relative to the glass melt in this hole.

The temperature in hole 1 for the N-S firing configuration (in the region near the root of the flame) was 400 K above the inlet temperature of the combustion air (1420 K). The two burners, which were recessed approximately 80 cm inside the portneck, were angled such that the geometric intersection of their normal centerlines occurred at the edge of the portneck. However, the momentum of the inlet combustion air caused the flame to converge further out in the combustion

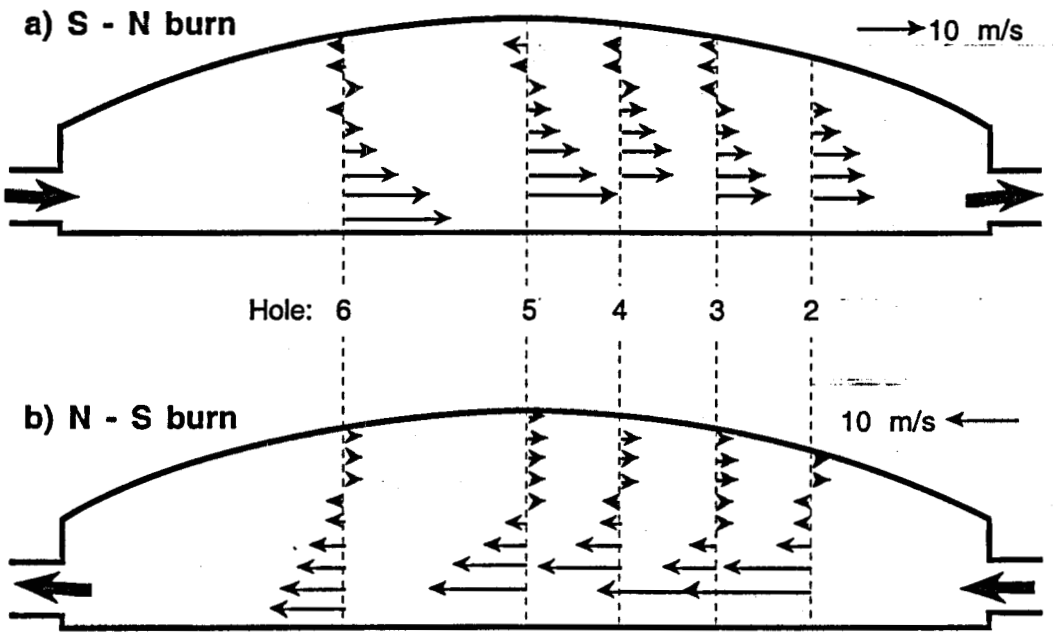

Figure 4. Contour plots of gas velocity in the combustion space of the furnace: (a) S-N firing configuration; and (b) N-S firing configuration.

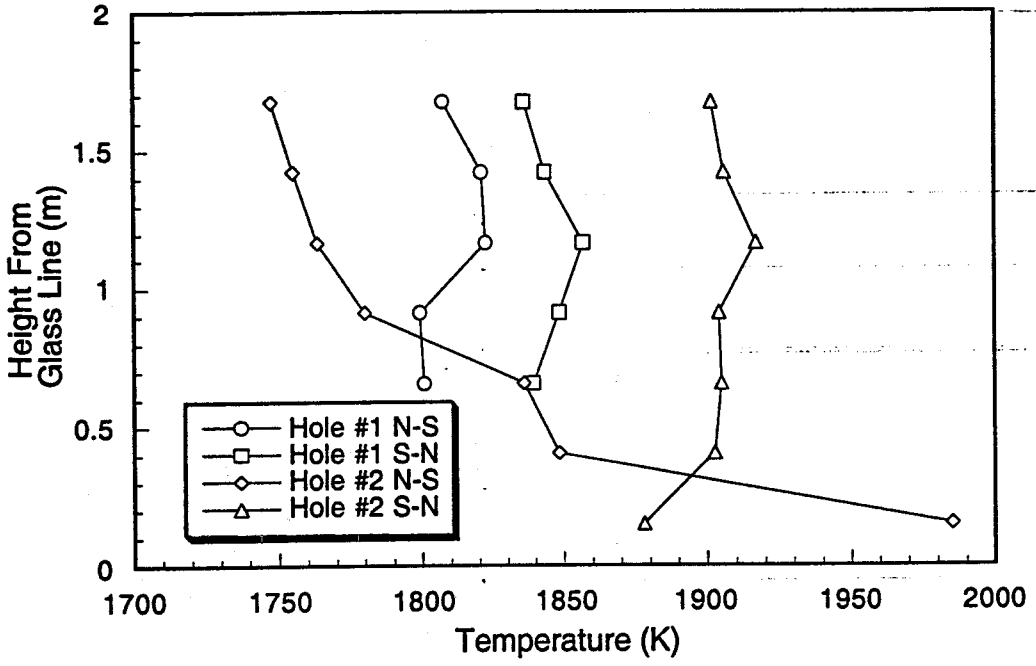

Figure 5. Gas temperature profiles for access holes 1 and 2 in the combustion space of the furnace for N-S and S-N firing configurations.

space. Despite this, ignition was observed visually to occur inside and near the sidewalls of the portneck. The rapid rise in temperature from the portneck exit to the location of hole 1 is indicative of rapid mixing and reaction.

The temperatures in the upper part of the furnace were higher in hole 1 than in hole 2 for the N-S configuration, while the reverse was true in the lower part of the furnace. The high temperatures near the crown for hole 1 were due to shear-induced entrainment of reacting (and hence, hot) combustion products from the root of the flame below. Wisps of luminous flame were observed being 'torn' off near the top edge of the flame jet and dragged back toward the portneck exit. This observation was consistent with the trend measured in hole 1. Lower temperatures observed in the upper furnace for hole 2 (approximately 60-70 K lower than for hole 1) were probably due to recirculation of cooler gases originating from near the tail of the flame, as seen in Figure 4.

The temperature profiles for holes 1 and 2 in the N-S firing mode exhibited a crossover at approximately 0.75 m from the glass line, with temperatures in hole 2 exceeding those in hole 1. Indeed, the temperature in hole 2 increased from 1850 K at a location 0.4 m above the glass line to nearly 2000 K at a location 0.2 m above the glass line. This was the region of most intense reaction in the flame jet, with strong temperature gradients.

The temperature data for the S-N firing configuration seen in Figure 5 reveal relatively flat temperature profiles for both holes 1 and 2, with some indication of a slight decrease in temperature near the glass line. In this case, holes 1 and 2 were located in the tail of the flame. Near the glass line, the oxygen was nearly depleted. The temperatures decreased with proximity to the melt due to heat transfer to the glass. Note that the temperature in hole 2 was higher (1910 K) than in hole 1 (1850 K). In the S-N configuration, hole 1 was downstream of hole 2, and both were just upstream of the portneck exit. The drop in temperature from hole 2 to hole 1 was therefore due to heat transfer by radiation and convection to the crown and glass melt. The local maximum in the vertical temperature profile near an elevation of 1.2 m in both holes 1 and 2 suggests heat transfer from the combustion products to both the crown above and the glass below.

Measured concentrations of O_2, CO, and CO_2 for the N-S firing configuration are shown in Figure 6. At any given hole, the trend of decreasing O_2 concentration from the top of the crown to the glass surface was observed, consistent with more intense reaction and oxygen consumption in the flame jet directed along the glass melt. In general, as the axial distance from the inlet portneck increased, the concentration of oxygen decreased. The highest O_2 concentrations were seen in hole 2 and the lowest in hole 6. The oxygen in the combustion air was consumed by reaction with the natural gas from the root of the flame (hole 2) to its tail (hole 6). Note the radical drop in O_2 concentration from the nominal atmospheric value of 21% to a peak of 9% in hole 2, only 2 m from the inlet port, suggesting that there was considerable reaction upstream of hole 2.

Low concentrations of O_2 can be seen near the glass surface for all of the holes in Figure 6a. Since the flame jet was directed downward by the portneck geometry, the reaction occurred most intensely near the glass surface, where the temperatures were highest. It is here that the oxygen was depleted first. The O_2 concentrations appeared to peak approximately one meter above the glass surface. This location corresponded to the boundary of the recirculation zone at the top of the flame jet.

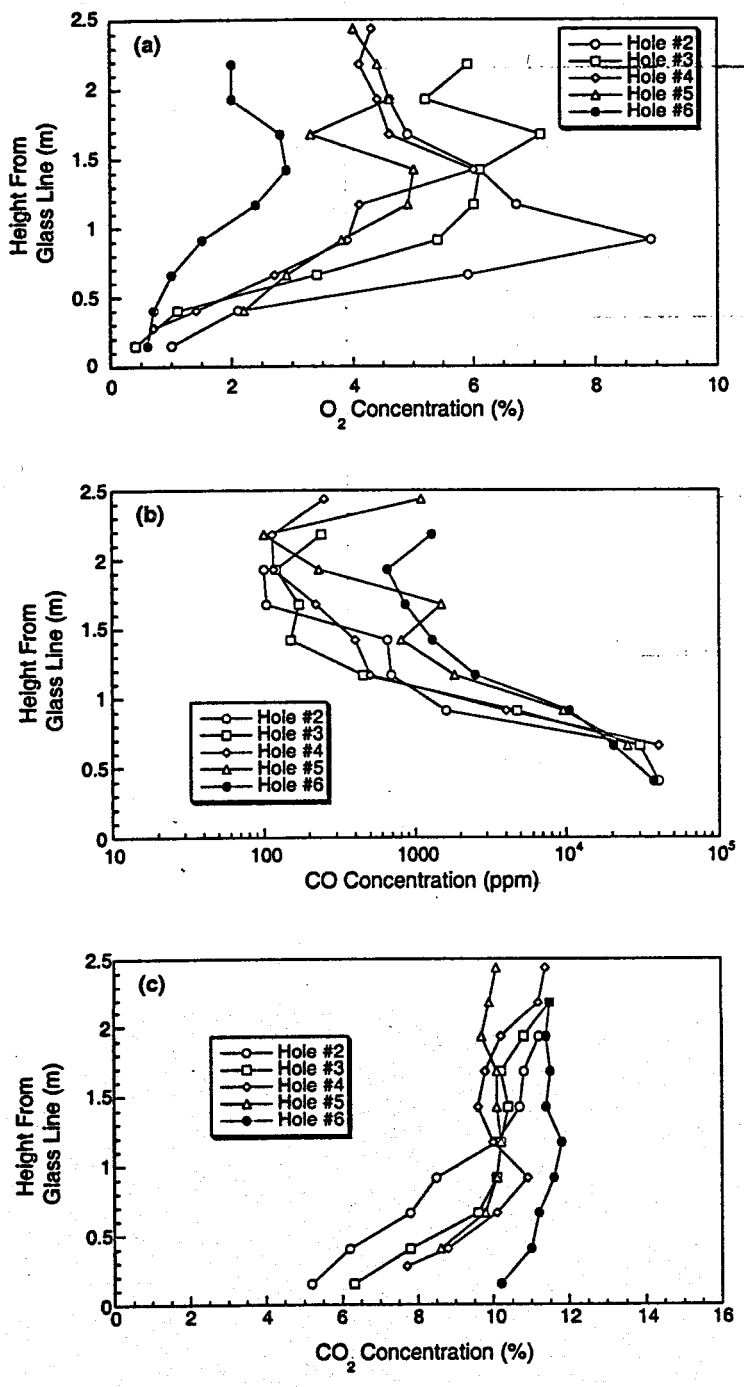

Figure 6. Concentration profiles of major species in the combustion space of the furnace for N-S firing configuration: (a) O_2; (b) CO; and (c) CO_2.

Profiles of oxygen concentration below this point (in the reacting flame jet) showed relatively large gradients, while those above (in the recirculation zone) were quite flat.

Profiles of measured CO concentration are illustrated in Figure 6b. The highest concentrations were near the glass surface inside the flame, reaching values exceeding 4% (40,000 ppm). The levels dropped quickly with increasing elevation in the furnace to the boundary of the recirculation zone (approximately 1 m) and then flattened. In general, CO concentration increased with increasing axial distance along the flame. The highest levels of CO were also seen in hole 6. The equilibrium concentration of CO at the adiabatic flame temperature corresponding to the stoichiometry of port 3 was less than 300 ppm. Hence, evidence of incomplete combustion was seen even in the tail of the flame (hole 6). This is not surprising, since the estimated air/fuel residence time in the furnace (based on measured portneck inlet and flame jet velocities in the combustion space) was less than 1 second. The fuel/air mixture had inadequate time to mix and react prior to exiting the furnace. This was further confirmed by measurements of CO at the exit portneck. Further, visual observations of the exhaust flow (downstream of the exhaust portneck) revealed luminous flame extending well into the regenerator.

The CO_2 profiles also showed a variation in concentration in Figure 6c, though not as dramatic as the CO and O_2. In general, the CO_2 concentration was lowest near the root of the flame (hole 2) and increased with axial position along the flame length, consistent with the progress of the combustion reactions. Higher CO_2 concentrations were observed in the upper region of the furnace where reaction was more nearly complete in the recirculation zone. Again, strong concentration gradients were evident in the flame jet with relatively little variation in the recirculation zone above. The maximum magnitude of CO_2 concentration was nearly 12%, which is considerably higher than expected from equilibrium calculations for the flame stoichiometry. Nearly half of the CO_2 generated in glass furnaces comes from the chemical reactions in the glass itself. This explains the higher-than-expected concentrations seen in Figure 6c.

The concentration of gases for the S-N firing configuration is shown in Figure 7. The O_2, CO, and CO_2 concentrations are shown in Figures 7a, 7b, and 7c, respectively. In the S-N burning mode the access holes lay in the tail of the flame. Thus, the oxygen concentrations were much lower than those values seen in Figure 6. Also, the vertical gradient in O_2 concentration was much less pronounced than those observed in Figure 6a. A general decrease in O_2 concentration was observed with distance along the flame jet axis, with magnitudes in hole 6 approximately 3% and those at hole 2 below 0.5%. It is interesting to note that even though port 3 was fired with $\phi = 0.66$, the oxygen along the centerline approximately 2 m upstream of the exhaust portneck was nearly depleted. It should be noted that O_2 concentrations in the portneck are considerably higher, suggesting that there was bypass of oxygen-rich flow that ultimately entered the exhaust portneck.

The high CO concentrations in Figure 7b show that combustion was incomplete. The lowest levels of CO in this figure are seen in the profiles of port 6 and the highest in port 2. Comparing these data with those of Figure 6b reveals that CO concentrations increased progressively in the furnace from the root of the flame jet to the tail. As in Figure 6b, the highest concentrations occurred near the glass surface where incomplete combustion was most prevalent. Further, the CO concentrations decreased with height.

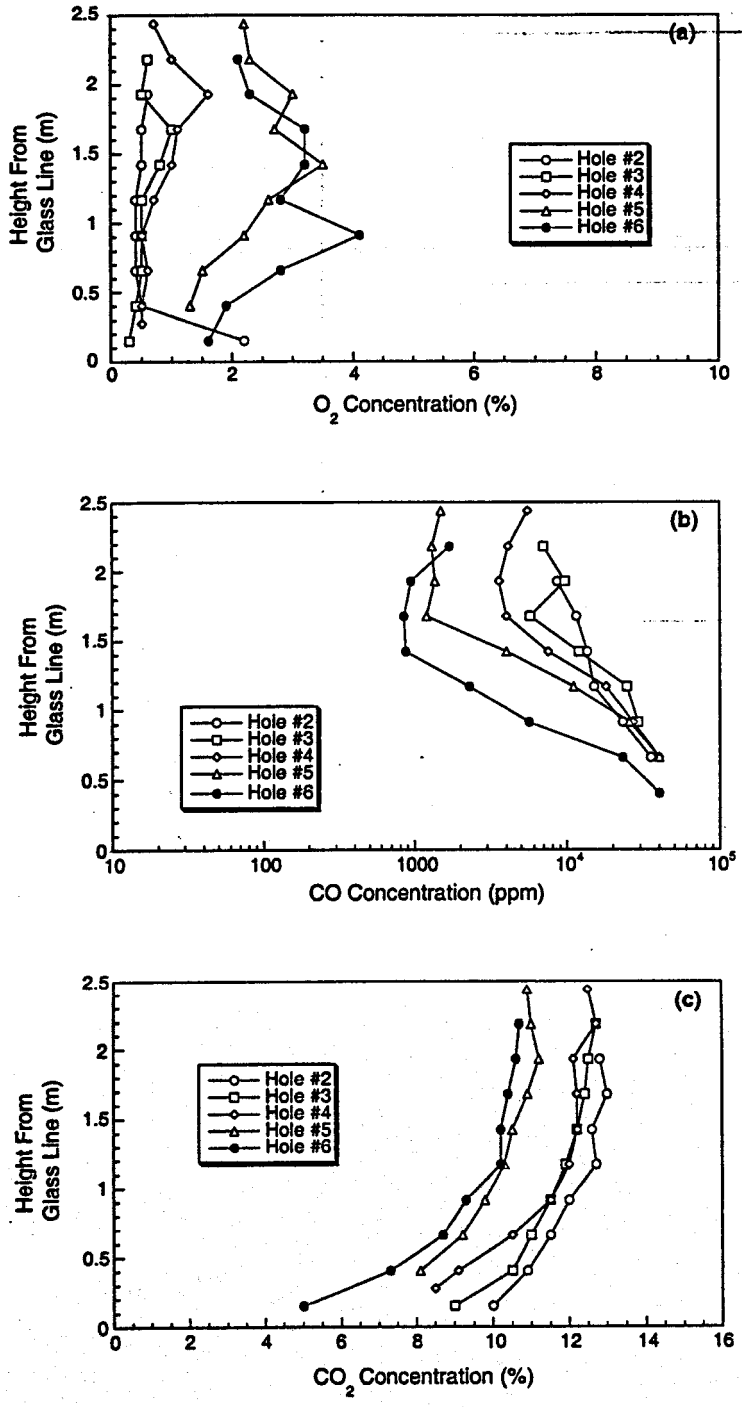

Figure 7. Concentration profiles of major species in the combustion space of the furnace for S-N firing configuration: (a) O_2; (b) CO; and (c) CO_2.

The concentrations of CO_2 shown in Figure 7c exhibit the same qualitative vertical profile variation as those shown in Figure 6c. As with the CO, the magnitude of CO_2 increased from the root of the flame jet to the tail; the effluents exiting the furnace show CO_2 concentrations exceeded 12%.

Local incident radiant heat fluxes were measured in holes 2 through 6 in the crown, and are shown graphically in Figure 8 for both firing configurations. The data show that the incident radiant heat flux was nearly invariant across the crown at a level of approximately 680 kW/m^2 and independent of firing direction. The only variation occurred near the north portneck where the incident flux is slightly higher for the S-N burning mode (exhaust), and slightly lower for the N-S firing configuration (inlet). The magnitude of incident radiative flux was extremely high, and corresponds to emission from a black surface at 1850 K. As shown in Table 1, the furnace wall temperature was measured between burn cycles to be approximately 1900 K. Thus, while the crown radiatively viewed the walls, the flame, and the cooler glass surface, the flame and walls dominated the incident heat flux. An energy balance for the probes used in this study based on cooling water flowrates, inlet and outlet cooling water temperatures, and estimated radiative properties for the exposed probe walls indicated excellent agreement (within 2%) with the measured incident radiative fluxes just presented.

2.1.4 Transient Measurements

Measurements were made in portneck 3 to assess the temporal variation of combustion parameters over the 15-minute burn cycle both for inlet and exhaust flow conditions. These were not truly instantaneous measurements due to the limiting time response of the instrumentation, probe suction, and other factors; the response time of the temperature measurement was approximately 4-5 minutes, the CO_2 required 2-3 minutes, and the O_2 and CO measurements responded in approximately 30 seconds. These measurements did, however, yield information with regard to the variation in combustion-relevant parameters over the period of a typical burn cycle. The results of the transient measurements are shown in Figure 9.

The velocity dependence in Figure 9a showed little variation with time at portneck 3 for both the N-S and S-N burn configurations. Velocity measurements inside the furnace (hole 6, 1.5 m from the glass line) revealed little temporal variation as well. The transient gas concentration in the effluent can be seen in Figure 9b. In this plot burn-cycle reversal begins at approximately 4 minutes and ends at 19 minutes. Within this time frame the O_2 and CO_2 concentrations reach a steady-state value rather quickly. The CO concentration, however, shows a dramatic rise initially, with a 30% drop to a near-stable value approximately 4-5 minutes into the burn cycle. The initial rise was perhaps due to incomplete combustion early in the cycle while a steady flow was established in the furnace.

Transient temperatures measured in the portneck were affected the most by the slow time response of the suction pyrometer. The measured temperatures at port 3 during the inlet and exhaust (N-S and S-N firing directions, respectively) phases of the cycle are shown in Figure 9c. Note that the exhaust temperature was nearly invariant over the cycle. However, the inlet combustion air decreased in temperature by perhaps as much as 150 K over the cycle. Again, these data can only be viewed qualitatively, but they illustrate the efficiency of the regenerator in recovering heat from the exhaust.

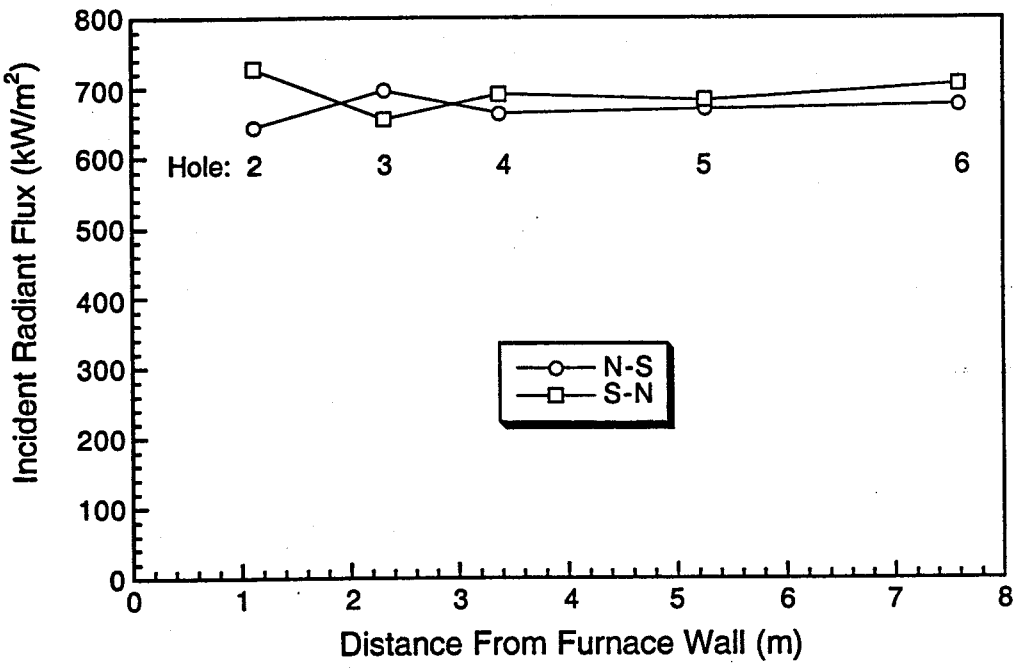

Figure 8. Radiant heat flux profile in the combustion space of the furnace for N-S and S-N firing configurations.

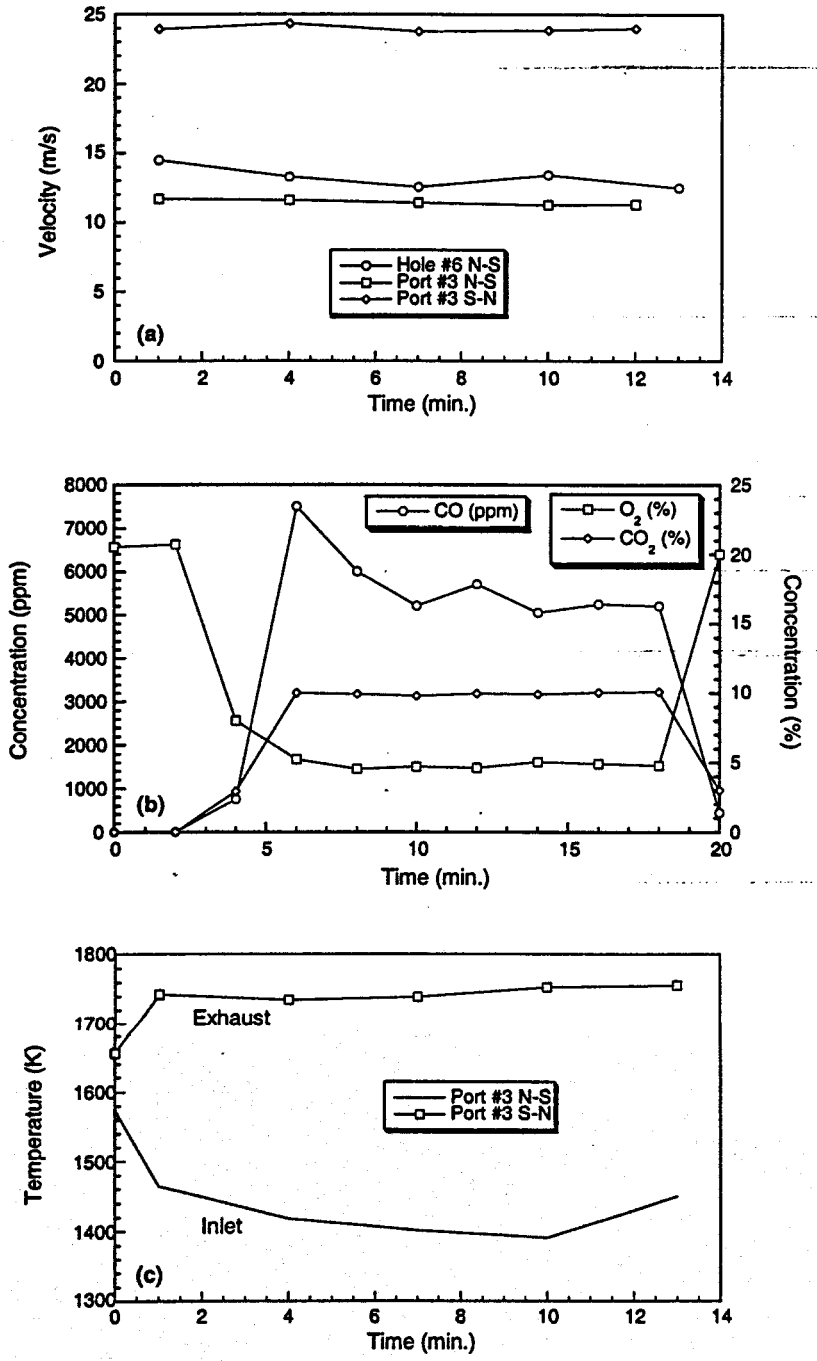

Figure 9. Time-dependent furnace and portneck measurements: (a) velocity, (b) species concentration, and (c) temperature.

2.1.5 Symmetry Evaluation

Holes 3 and 6 were located equidistant from the crown centerline on opposite sides. These two holes allowed for a limited evaluation of symmetry in the combustion process in the furnace by comparing N-S firing information at one hole (either hole 3 or 6) to the same information collected for S-N firing configuration at the other hole. These comparisons were possible both in the region near the root of the flame as well as the flame tail and were made for the data collected in these two holes for both firing configurations (the information already presented in Figures 4, 6 and 7, and 8 on gas velocity, species concentration, and wall incident radiant heat fluxes, respectively) and are discussed here qualitatively. CO, O_2, and CO_2 concentrations averaged over the measured profile are shown in Table 2 for the N-S and S-N burn configurations where holes 3 and 6 lay in the root and tail of the flame, respectively.

Radiant heat flux and gas velocity were the variables that displayed the highest degree of symmetry. As presented in Figure 8, heat flux values were nearly constant along the port centerline. Maximum variation in gas velocity at a given location both in the flame root or the flame tail were less than 5% at the region of large positive velocities in the flame jet. In the recirculation zone, the deviations were larger, but the qualitative trend indicates a high degree of symmetry. CO_2 concentrations displayed symmetry near the root of the flame for all the locations where measurements were made above the glass line. Although similar trends were observed in the flame jet region near the flame tail, deviations increased to a maximum of 12% in the recirculation zone. The average concentration shows good symmetry (Table 2). Finally, O_2 and CO measurements displayed moderate symmetry only in the flame jet region near the root of the flame. Elsewhere, deviations were quite large, particularly in the recirculation zone both in the root and tail of the flame. This is evident in the profile averages shown in Table 2.

2.2 Pre- and Post-Rebuild Comparison: Inlet and Exhaust

In this section the measurements performed after the furnace rebuild are reported and compared to those made before the furnace rebuild (Section 2.1). Whenever appropriate, additional information will be provided for the unique measurements that were performed only after the furnace was rebuilt, such as glass surface temperature, etc. In order to avoid unnecessary repetition, the reader is referred back to Section 2.1 for a description of the instrumentation common to both test campaigns.

A typical goal for the campaign life of a flat-glass furnace is ten years. Two main factors dictate the life of the tank: refractory corrosion/erosion, and plugged checkers (regenerator). The most severe erosion usually occurs at the glass line. The refractory is eroded by the movement of the molten glass and by reactions with the high temperature (1900+ K) atmosphere, which chemically attacks the refractory (mainly at the crown, where less expensive refractory materials are typically used). The checkers provide the air preheat required for energy efficiency. Over time, the exit flow of the combustion products through the checkers creates deposits. Although the checkers can be burned out and cleaned, they eventually become so plugged in regions that they severely restrict the flow

Table 2. Evaluation of combustion symmetry.

Flame region	Hole	CO (ppm)	O_2 (%)	CO_2(%)
Tail of the flame:	Hole 3 (S-N burn)	10,730	0.5	11.5
	Hole 6 (N-S burn)	9,290	1.7	11.3
Root of the flame:	Hole 3 (N-S burn)	9,480	4.5	9.7
	Hole 6 (S-N burn)	15,240	2.6	9.1

and distribution of the combustion air or they cave in, which further unbalances the pressure drop throughout the regenerator. This can result in large fluctuations of the air/fuel ratio. Thus, when a glass-melting tank has deteriorated to the point at which it is not safe or cost-efficient to operate, it must be rebuilt.

A typical furnace rebuild entails complete removal of all the refractory (walls, crown, and floor) of the melting tank and regenerators. Only the steel structural skeleton of the glass melt tank and regenerators remains. Then the glass melting tank, regenerators, and portnecks are formed using thousands of refractory bricks measuring 305-457 mm thick. Inside the regenerators, the checkers are packed to provide the required combustion air preheat with minimal pressure drop. Piping, fans, motors, wiring, sensors, and controls are all checked, repaired, replaced, or upgraded.

During a rebuild, the geometry of the portnecks and melt tank can also be altered to improve performance (fine-tune the furnace design). Usually these changes are not drastic because the tremendous cost associated with a rebuild (up to US$100 million) limits the changes (risks) companies are willing to take. Typical changes include minor variations in the size and shape of the portnecks, radius and height of the crown, etc.

The obvious effects of a rebuild are to restore the furnace to its design performance. At the end of a campaign, the flow and distribution of combustion air can vary significantly from the original because of plugged checkers and eroded and deposited portnecks. Portnecks carry the combustion air to the furnace and combustion products from the furnace. The mixing of the gas and combustion air depends on the flow field and turbulence created by the regenerator and portneck design. Therefore, from the combustion viewpoint, a rebuild restores the flow and distribution of combustion air through the checkers and portnecks to mix with the gas (at the desired stoichiometry) and provide the desired heat fluxes and energy efficiency. This paper reports measurements taken at stable operating conditions that yield acceptable glass quality both before and after a furnace rebuild. Since the rebuild restores the furnace to its design condition, the operating conditions before and after rebuild are usually different. The plant-controlled furnace operating conditions (fuel and air flowrates, *etc.*) and the measured furnace performance characteristics reported here illustrate the impact of rebuild on furnace performance.

The objective here was to compare, for the first time, the effect of furnace rebuild on the combustion performance of an industrial-scale furnace. Measurements taken in the portnecks of the side-port, 550-ton/day, gas-fired, flat-glass furnace described in the previous section are compared with the similar measurements made in the same furnace after rebuilding. The conditions at which measurements were taken coincide with "normal" furnace operation (at which quality glass was produced) both before and after the rebuild, rather than an attempt to reproduce identical operating conditions. This more clearly illustrates the impact of furnace rebuild on furnace operation. The information obtained includes profiles of velocity, species concentration (O_2, CO, and CO_2), and gas temperature in the access ports located in the six portnecks.

2.2.1 Gas Composition

The measured exhaust gas concentrations in the portnecks can be seen in Figures 10, 11, and 12 for the concentrations of O_2, CO, and CO_2, respectively. Note also that the measurements after the

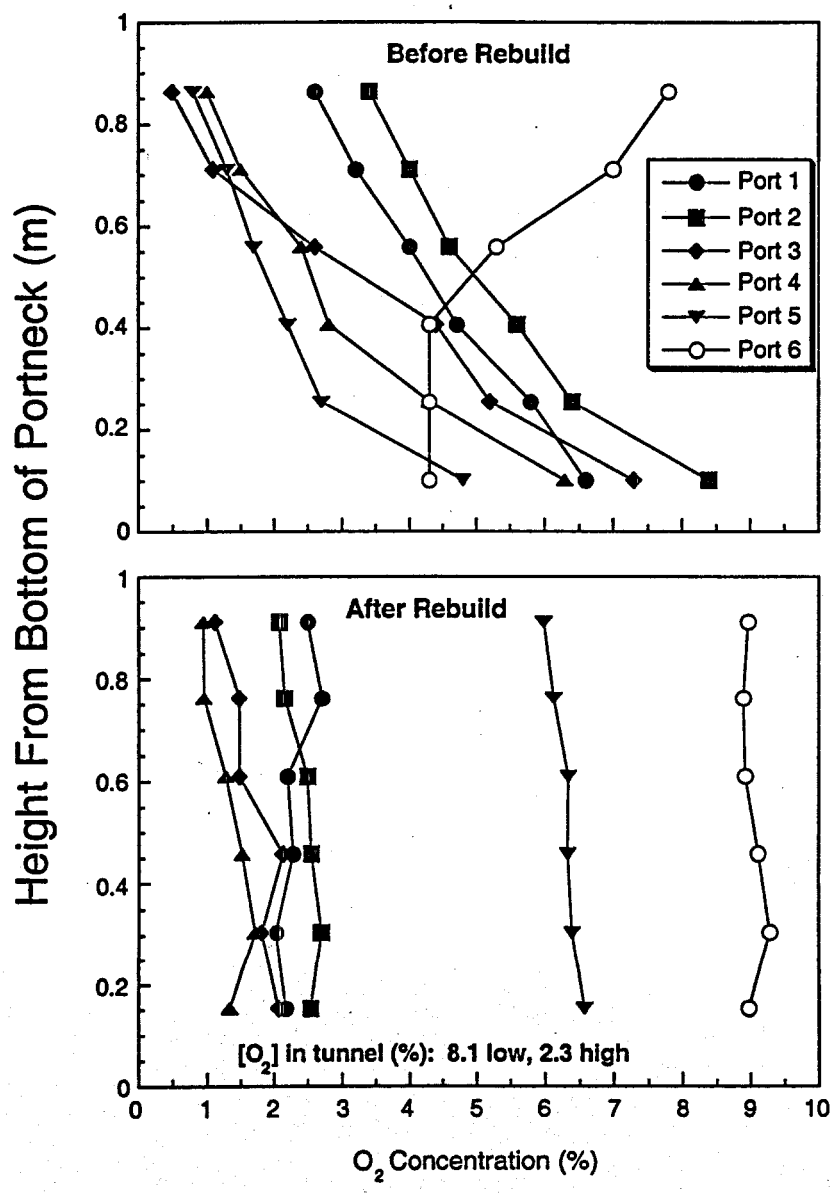

Figure 10. Comparison of portneck O_2 concentration profiles for S-N firing configuration (exhaust) before and after the furnace rebuilding.

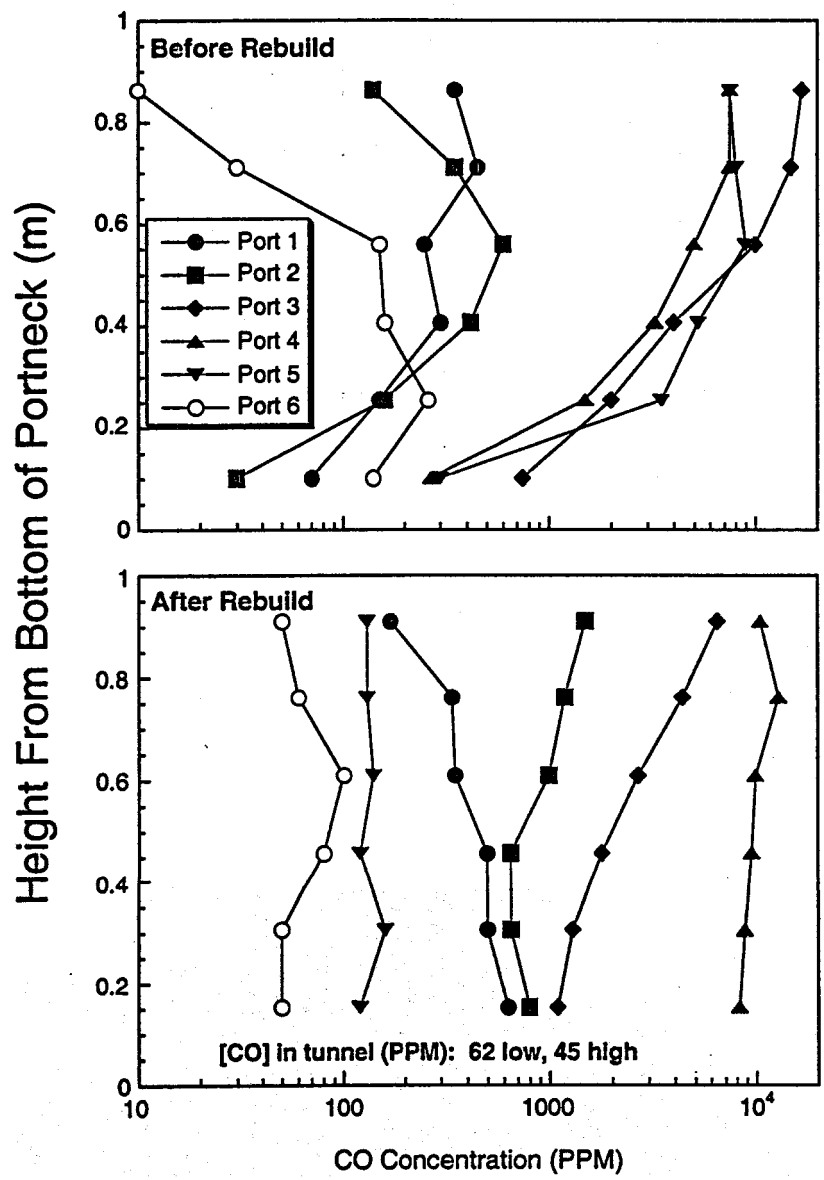

Figure 11. Comparison of portneck CO concentration profiles for S-N firing configuration (exhaust) before and after the furnace rebuilding.

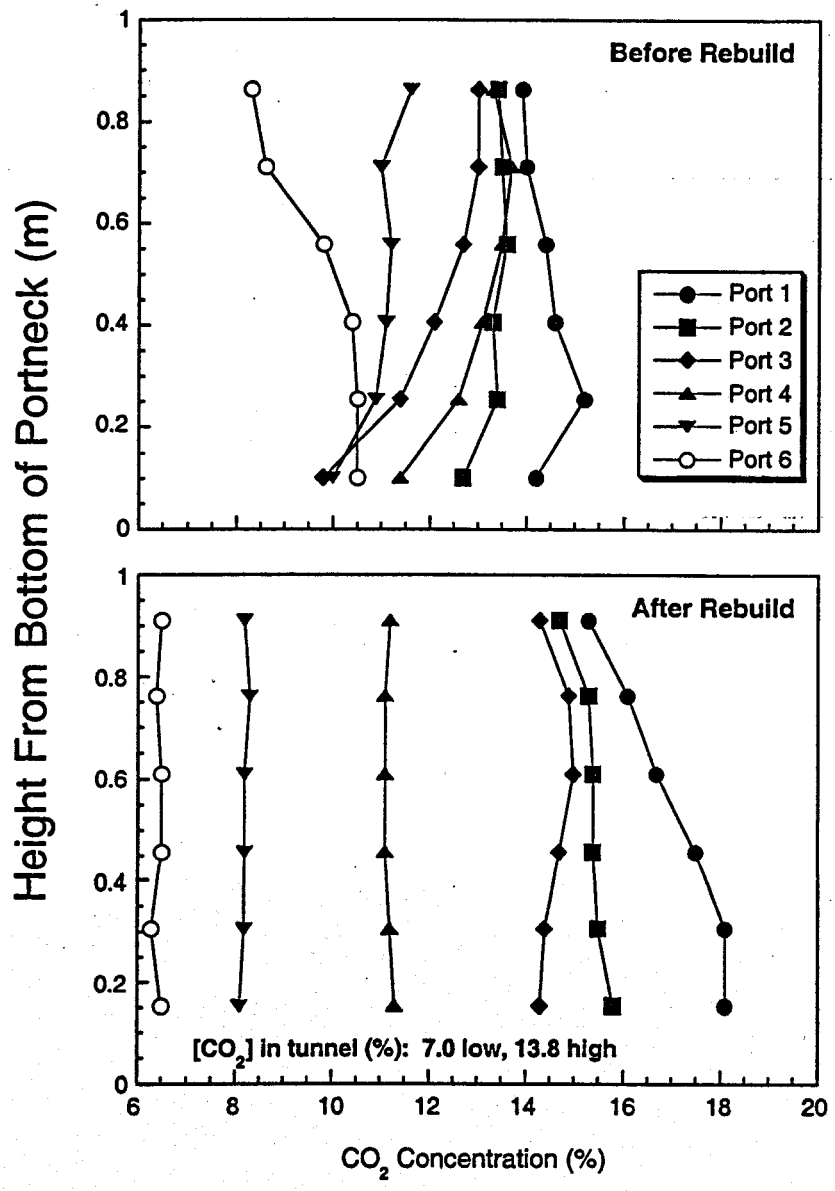

Figure 12. Comparison of portneck CO_2 concentration profiles for S-N firing configuration (exhaust) before and after the furnace rebuilding.

rebuild in two regenerator-tunnel locations are reported at the bottom of the figure with the after-rebuild measurements. Figure 10 reveals significant variation in O_2 concentration over the portneck height before the rebuild. The oxygen concentration in portneck 3, for example, varied from 0.5% at the top to 7.3% at the bottom. This is representative of all portnecks with the exception of port 6. Measurements in the combustion space along the centerline of port 3 prior to the rebuild (Newbold *et al.*, 1997) revealed oxygen concentrations near the tail of the flame were approximately 0.5%, yet the concentrations in the exhaust portneck of port 3 were much higher (0.5-7.3%). The implication is that there may have been significant bypass of oxygen-rich flow around the outside of the flame jet, which ultimately exited the furnace through the exhaust portneck. After the rebuild, the vertical variations in O_2 concentrations were smaller.

During the tests after the rebuild, a limited number of species concentration measurements were made below one of the regenerators in the tunnel leading to the furnace stack. The objective of these measurements was to explore the effect of the flow through the regenerators on these variables. The measurements in the tunnel after the rebuild indicate a stratification effect in the O_2 measurements. Low in the tunnel, the measured value of 8.1% corresponds to the high values measured in port 6. High in the tunnel, the low value of 2.3% corresponds to the average values measured in portnecks 1 through 4.

Generally speaking, low O_2 concentrations in the effluent were consistent with high CO concentrations, as seen in Figure 11 for both before and after the furnace rebuild. Relatively modest CO concentrations (<400 ppm) were found in the exhaust flow of ports 1, 2, and 6, whereas CO concentrations in ports 3, 4, and 5 reached 2% before the rebuild. The high concentrations of CO in ports 3, 4, and 5 were near the ceiling of the portneck where the corresponding O_2 concentration is low, indicating incomplete combustion. Measurements after the rebuild showed variation in CO concentrations from 10,000 ppm in port 4 where the O_2 concentration was the lowest (about 1.5%, Figure 10) and the exhaust temperature was the highest (to be seen later), to about 60 ppm in port 6 where the O_2 concentration was the highest (9%) and the exhaust temperature was the lowest. These measurements show that the flow and mixing upstream in the flame jet was a complex three-dimensional flow field, yielding such dramatic variations in both CO and O_2 in the exhaust flow. The measurements made in the regenerator tunnel also indicate that the combustion reactions continued inside the regenerators, resulting in overall complete combustion as indicated by the very low CO levels in the tunnel.

The exhaust concentrations of CO_2 before and after the rebuild are displayed in Figure 12. With the exception of port 6 before the rebuild, the profiles are nearly uniform across the portneck height, especially after the rebuild. There was a slight trend of lower CO_2 concentration near the bottom of the portnecks after the rebuild. The port-to-port variations reveal that the highest CO_2 concentrations occurred in the ports near the batch. This would suggest that the CO_2 generation in the glass reaction was more pronounced in the early part of the glass melt (nearest the doghouse).

With the measurements of O_2 and CO_2 and the plant-measured fuel flowrate at each port, it was possible to perform the mass balance for an overall reaction equation, including the CO_2 generated by the glass reaction. This analysis provided an estimate of the total air flowrate as well as the stoichiometry in each port and the CO_2 produced by the glass reaction. Such a reaction for one mole of fuel is of the form

$$fuel + \alpha CO_2 + \beta(O_2 + 3.76N_2) \rightarrow \gamma CO_2 + \delta H_2O + \varepsilon O_2 + \kappa N_2 \quad (1)$$

The six coefficients in this equation were determined by solving the mass conservation equations for oxygen, nitrogen, carbon, and hydrogen, and the two equations that represent the measured average concentrations, on a dry basis, of oxygen and carbon dioxide, as shown below:

$$[CO_2]_{dry} = \frac{\gamma}{\gamma + \varepsilon + \kappa} \quad (2)$$

$$[O_2]_{dry} = \frac{\varepsilon}{\gamma + \varepsilon + \kappa} \quad (3)$$

The results before and after rebuild are shown in Table 3.
Sensitivity of the results to the neglect of CO in Equation (1) was investigated by performing the balance for the portneck with the highest average CO concentration (port 3 prior to the rebuild, $[CO]_{dry} \approx 1\%$). The inclusion of CO made a difference of less than 1% in the predicted port-by-port air flowrate.

The predicted CO_2 formed in the glass shown in Table 3 before and after the rebuild was within 15% of the value estimated by Ford personnel (see Table 1). The largest excess air before the rebuild was 33.6%; the lowest was 10.9%, compared to 77.1% and 6.3%, respectively, after the furnace rebuild. The overall stoichiometry was not much different before and after the rebuild (22.5% excess air compared to 19.2%). This explains the fact that glass quality was not significantly changed after the rebuild, but it also indicates that the plant was under the impression (based on its own measurement of fuel and air flowrates) that it was operating in significantly different air/fuel ratios before and after, when in reality those values were quite close. The total air flowrate calculated by this analysis after the rebuild was within 9% of the plant-measured value. It is difficult to make a similar comparison before the rebuild because of the expected high amounts of air leakage. The observed trends in O_2, CO, and CO_2 concentrations for the portnecks shown in Figures 10, 11, and 12 are in qualitative agreement with the individual port stoichiometry analysis shown in Table 3. O_2 profiles after the rebuild shown in Figure 10, for example, indicate that port 6 had the largest excess air, and ports 3 and 4 the lowest. This trend is supported by the results shown in Table 3. Similar trends are observed for the CO profiles shown in Figure 11 and the results of this analysis. The CO_2 generation in the glass also presents similar trends to the CO_2 profiles measured in the ports as shown in Figure 12. The ports with the largest generation rates had the largest CO_2 concentration values.

2.2.2 Gas Temperature

Inlet (N-S firing direction) and exhaust (S-N firing direction) gas temperature measurements by port before and after the furnace rebuild are shown in Figure 13. Spatially resolved portneck temperature measurements, similar to gas velocity and species measurements being discussed here, were not possible because the diameter of the suction pyrometer probe was larger than the vertical

Table 3. Combustion analysis based on fuel flow and oxygen and carbon dioxide dry-basis concentration measurements.

Before Furnace Rebuild

	$[O_2]_{dry}$ (%)	$[CO_2]_{dry}$ (%)	Fuel Flow (kg/hr)[a]	α^b	β^b	γ^b	δ^b	ε^b	κ^b	Excess Air (%)	CO_2 Production (kg/hr)[c]	Air Flow (kg/hr)[d]
Port 1	4.48	14.38	583	0.661	2.501	1.679	1.941	0.523	9.472	26.4	924	10,910
Port 2	5.4	13.32	611	0.622	2.643	1.640	1.941	0.665	10.00	33.6	913	12,100
Port 3	3.52	12.00	619	0.246	2.349	1.264	1.941	0.371	8.900	18.7	366	10,880
Port 4	3.05	12.93	603	0.320	2.294	1.338	1.941	0.316	8.692	16.0	461	10,320
Port 5	2.25	10.97	618	0.033	2.194	1.051	1.941	0.216	8.317	10.9	49	10,160
Port 6	5.5	9.68	462	0.115	2.622	1.133	1.941	0.644	9.926	32.5	127	9,040
Total			3,496							22.5	2,840	63,410

After Furnace Rebuild

	$[O_2]_{dry}$ (%)	$[CO_2]_{dry}$ (%)	Fuel Flow (kg/hr)[a]	α^b	β^b	γ^b	δ^b	ε^b	κ^b	Excess Air (%)	CO_2 Production (kg/hr)[c]	Air Flow (kg/hr)[d]
Port 1	2.32	16.97	494	0.751	2.220	1.769	1.941	0.242	8.415	12.2	889	8,190
Port 2	2.42	15.35	557	0.557	2.227	1.575	1.941	0.248	8.440	12.6	746	9,300
Port 3	1.68	14.60	590	0.398	2.141	1.416	1.941	0.163	8.118	8.2	563	9,460
Port 4	1.3[e]	11.17	571	0.000	2.102	1.018	1.941	0.124	7.972	6.3	0	8,950
Port 5	6.3[e]	8.2	514	0.000	2.796	1.018	1.941	0.817	10.58	41.3	0	10,770
Port 6	9.0[e]	6.45	160	0.000	3.503	1.018	1.941	1.525	13.24	77.1	0	4,150
Total			2,886							19.2	2,198	50,820

[a] Fuel flow rate for each port as reported by the plant.

[b] Stoichiometric coefficients for Equation 1 as calculated based on one mole of fuel and the measured dry-basis O_2 and CO_2 concentrations.

[c] Calculated CO_2 produced by the reaction in the melt based on stoichiometric coefficients shown and fuel flow rates for each port.

[d] Calculated airflow rate based on stoichiometric coefficients shown and fuel flow rates for each port.

[e] These concentrations were not used in the solution for the stoichiometric coefficients because there was no CO_2 produced by the melt reaction in these ports.

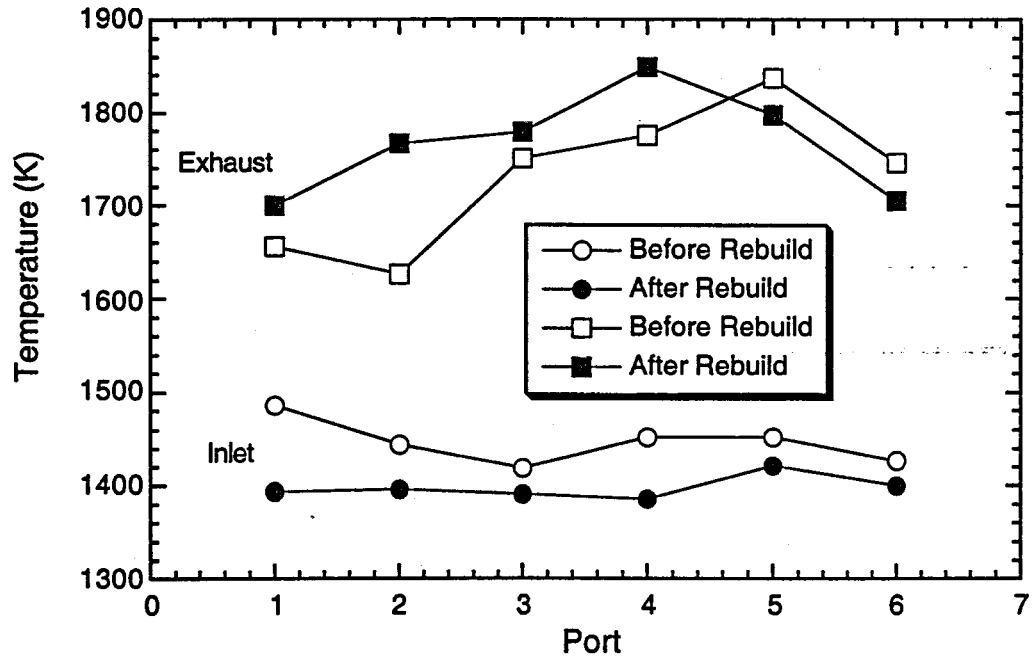

Figure 13. Comparison of inlet (N-S firing configuration) and exhaust (S-N firing configuration) gas temperature measurements by port (port 1 is near the batch) before and after the furnace rebuilding.

portneck access holes. For this reason, inlet and exhaust gas temperature data for each port were measured from inspection holes in the regenerator wall, as was explained previously.

The average furnace exhaust temperature was somewhat lower before the furnace rebuild (1735 K) than after (1758 K). This was due to the increased temperatures in the furnace associated with the reduced excess air after the rebuild. Interestingly, the temperature of the inlet preheat air was higher before rebuild than after, the profiles showing little variation from port to port. This surprising experimental result occurs because of the reduced overall air flowrate (approximately 20%) through the furnace. Despite the higher exhaust temperatures, there was actually less recoverable energy after the rebuild because of the reduced total mass flowrate.

The port-by-port furnace exhaust temperature data both before and after the rebuild reflect the stoichiometry for each port from the analysis presented in the foregoing sections and are summarized in Table 4. Lowest exhaust temperatures were found in those ports where the excess air was the highest, and high temperatures were found where the port firing was more nearly stoichiometric. Further, exhaust temperatures for the post-rebuild case in ports 1-4 were higher than their pre-rebuild counterparts because the excess air was lower. In ports 5 and 6, where the excess air following the rebuild was high, the temperatures were lower than prior to the rebuild.

2.2.3 Gas Velocity

Measured inlet air velocities at all six portnecks before and after the furnace rebuild can be seen in Figure 14. It should be emphasized that these measurements were made at a location approximately 1.7 m from the portneck entrance/exit to the furnace, as seen in Figure 2. With the area change along the length of the portneck, these velocities were higher than what was found at the portneck entrance/exit to the furnace. The portneck inlet velocities after the furnace rebuild were generally similar to those measured before the rebuild. Also, excluding points very near the top wall, inlet velocity profiles were flatter after the furnace rebuild, having average values around 10.5 m/s with variations from port to port of ±14%. Before the rebuild, the average velocity was approximately 11 m/s, with the same variation from port to port as after the rebuild. The highest and lowest average velocities measured before the rebuild were 7 m/s in port 4 and 14 m/s in port 1; similar values of these quantities were measured after the rebuild (7.5 m/s in port 2 and 13.5 m/s in port 1). Note in Figure 1 that port 1 is near the batch and port 6 is next to the working end of the furnace. These observed trends are due in part to the reduced overall flow in the furnace (see mass balance analysis summary of Table 3) and the physical condition of the portnecks before and after the rebuild. Figure 15 shows photographs of a typical port before and after the furnace rebuild, illustrating the significant buildup and geometry alteration in the portneck over several years of normal furnace operation. Previous measurements in the furnace combustion space before rebuild (Newbold *et al.*, 1997) indicated that velocities for the flame jet inside the furnace combustion space reached levels exceeding 20 m/s; there was a significant acceleration of the combustion gases through the furnace.

With the port-by-port inlet air temperature data of Figure 13 to calculate the density, mass flow in each port was estimated by integrating the velocity over the portneck area. Since portneck access allowed only one velocity profile measurement, the velocity was assumed to be horizontally constant, with the vertical variation shown in the profiles of Figure 14, total air flowrates of 80,400

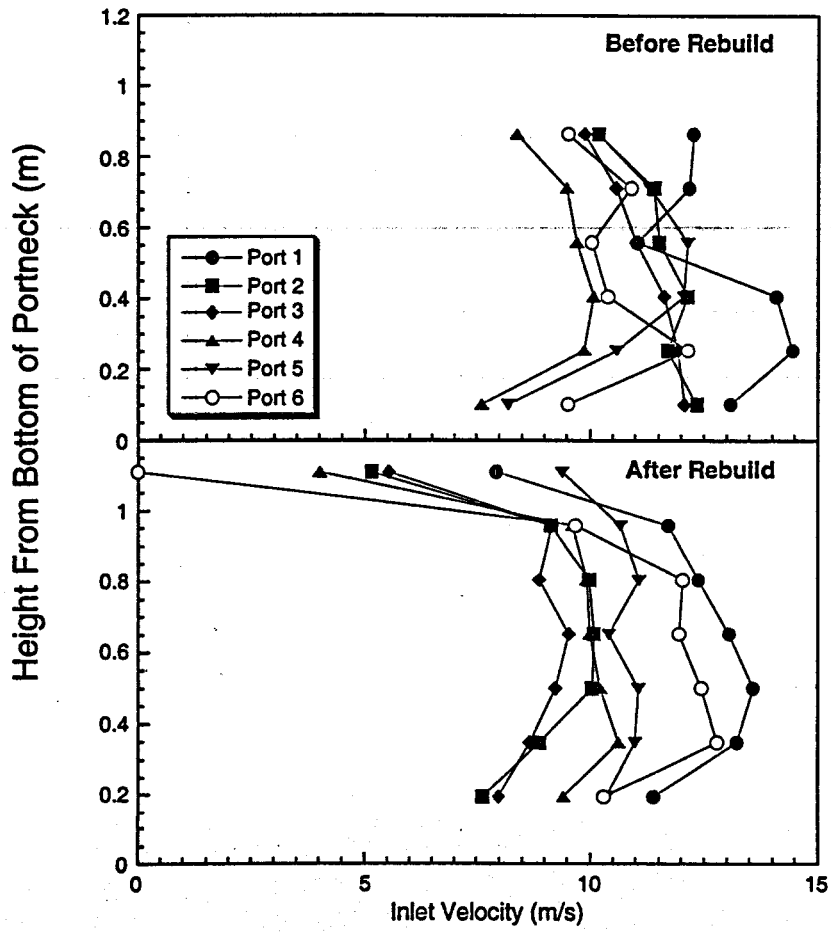

Figure 14. Comparison of portneck gas velocity profiles for N-S firing configuration (inlet) before and after the furnace rebuilding.

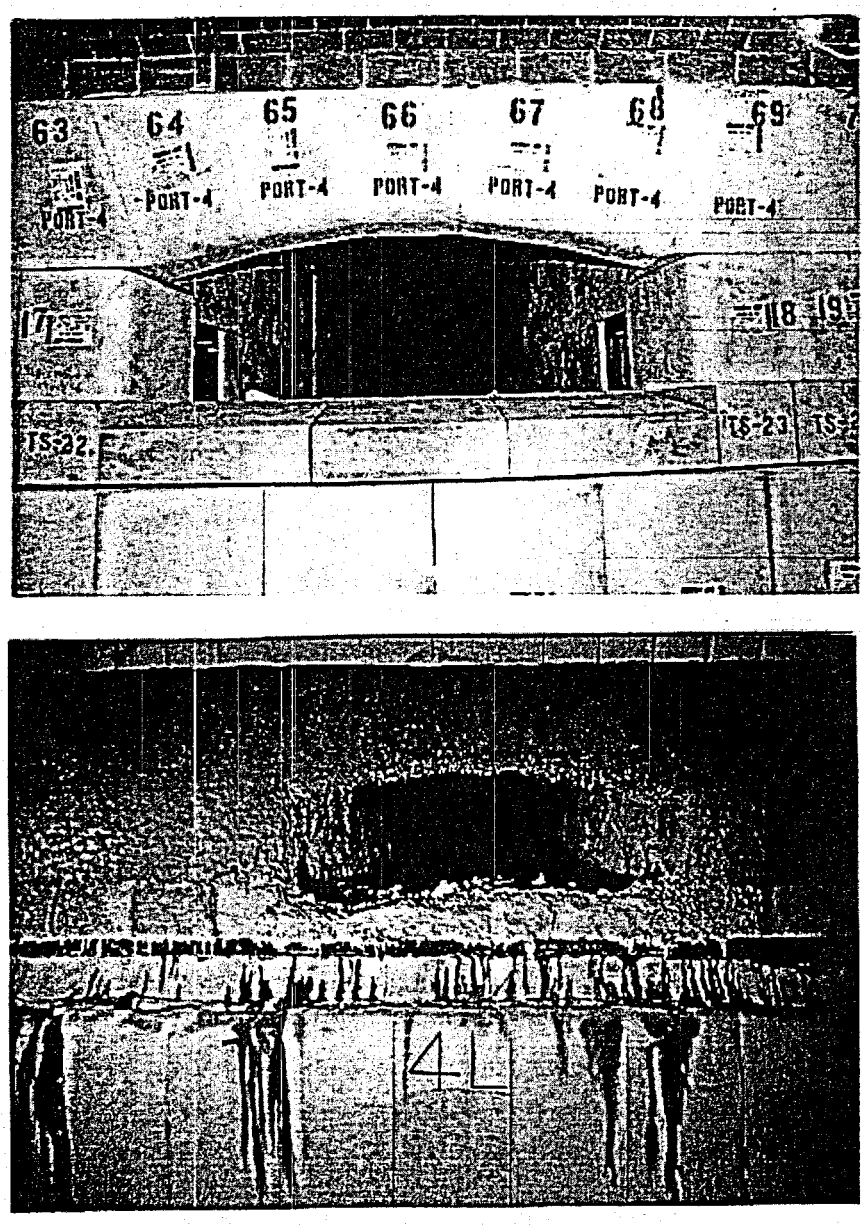

Figure 15. Photographs of a typical port (a) before and (b) after the furnace rebuilding.

kg/hr and 72,900 kg/hr were determined before and after the rebuild. Note that these values are considerably higher than the estimates made from the mass balance analysis summarized in Table 3 and are inconsistent with the temperatures observed. This underlines the complex nature of the flow in the portneck and suggests lower velocities near the lateral sides of the portnecks.

2.3 Surface Temperature

Glass surface temperature measurements in industrial glass furnaces have not previously been reported in the literature. Glass temperature is a critical parameter in furnace design and operation. In addition to affecting the rate of heat transfer to the glass, the glass temperature plays an important role in determining the quality of the glass being produced.

Glass surface temperature was measured through the six access holes in the crown of the rebuilt, 550 ton/day, gas-fired flat-glass furnace described previously. Six thermocouple plugs, when removed, provided access holes located along the center of the crown apex at axial furnace locations coinciding with the transverse centerlines of each of the six ports shown in Figure 1. Transient phenomena, which occur during the 20-second reversal period when firing does not take place, were investigated. The information obtained includes average temperature of the glass surface at each of the six port locations, as well as time-resolved information at five of the port locations, all measured during reversal of the regenerator cycle.

The input conditions for these measurements are shown in Table 4. The firing rate for the pair of burners associated with each port is noted by the two fuel flowrates. The first is for the burner on the side of the portneck nearest the batch feeder. The fuel flowrates presented in Table 4 were measured during the period when the measurements discussed here were performed. Previously, detailed effluent (O_2, CO, CO_2) concentration measurements were carried out on this furnace, and using the measured fuel flowrates and measured exhaust concentrations of O_2 and CO_2 in each port, the combustion reaction equation was balanced for each port to solve for the inlet air flowrates (McQuay *et al.*, 2000). The tests reported here were done after those previous tests (McQuay *et al.*, 2000), and therefore, there were slight differences in the port-by-port fuel flowrates. Therefore, air flowrates for each port in the combustion modeling done as part of this study were calculated assuming identical port-by-port stoichiometry (% excess air) as in the previous tests (McQuay *et al.*, 2000) but for the measured fuel flowrates of these tests. As noted in Table 4, the majority of the fuel is distributed in ports 1-5, with a smaller fraction used in the port nearest the working end of the furnace (port 6). The fuel and air inlet temperatures were assumed to be the same as before (McQuay *et al.*, 2000). Note that combustion air inlet temperatures are nearly uniform across all ports at approximately 1400 K.

2.3.1 Instrumentation

Glass surface temperatures were measured optically using a two-color pyrometer. Figures 16a and 16b are schematics of the instrument. The optical detector housing was mounted on a water-cooled sight tube. The sight tube was 4.3 cm I.D. and 1.0 m long. Inside the optical detector housing, lenses focus the infrared radiation entering the sight tube onto amplified germanium photodiodes. The radiation was transmitted through interference filters with 30 nm bandwidths centered at 1.27

Table 4. Inlet flowrates and temperatures.

	Hydraulic Dia. (m)	Fuel Flowrate[a] (kg/hr)	Air Flowrate[b] (kg/hr)	Air Temp. (K)	Excess Air (%)
Port 1	1.54	233 / 350	9,720	1395	12
Port 2	1.54	333 / 333	11,230	1397	13
Port 3	1.46	333 / 333	10,730	1395	8
Port 4	1.54	325 / 325	10,260	1392	6
Port 5	1.54	339 / 339	14,260	1420	41
Port 6	1.06	244 / 0	6,440	1400	77

[a]Fuel flowrate for each of the two burners per port as reported by the plant

[b]Air flowrates estimated using fuel flowrates measured for this study and assuming identical port-by-port stoichiometry (% excess air).

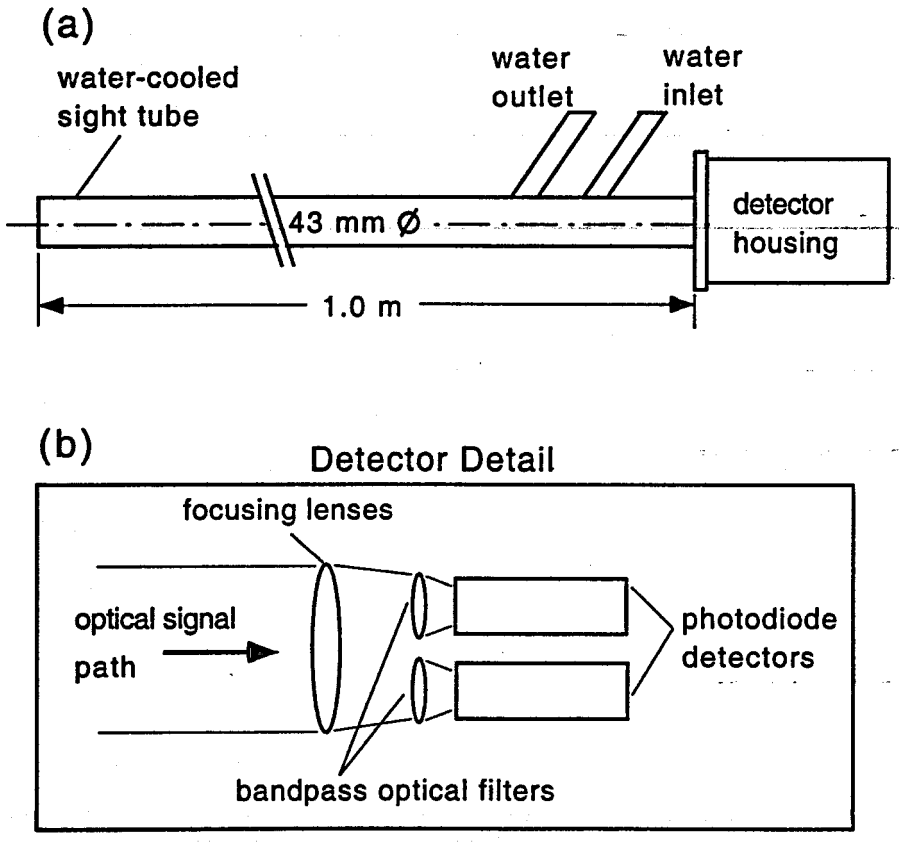

Figure 16. Schematics of the two-color pyrometer instrument used for optical glass surface temperature measurements (a), and of the detector detail (b).

and 1.60 μm. These wavelengths were chosen to avoid the absorption bands of CO_2 and water vapor. The signal amplification system for each channel was constructed with adjustable gain to permit modification for a range of high temperatures and a variety of data acquisition equipment.

For the glass temperature measurements, the amplified output from the detector was 1-12 volts. Time-averaged readings were obtained using a voltmeter, while both time-averaged and time-resolved measurements were recorded using a computer-based data-acquisition system with a 12-bit analog-to-digital converter. This system provided a sampling rate of 5000 Hz for temperature measurements, enabling a thorough time-resolved investigation of the glass surface temperature variation during the 20-second reversal period. Insulated, high-temperature, shielded cables were used to transmit the signal directly from the two-color optical assembly on the crown to the data acquisition system.

The two-color pyrometer was calibrated both with and without the water-cooled sight tube. The detector assembly (without sight tube) was factory-calibrated between 900 and 2000 K using a small reference blackbody. Later, the detector system, with water-cooled sight tube attached, was calibrated in the laboratory using a blackbody cavity designed and built for this purpose. The blackbody cavity was heated using a small electric laboratory furnace. However, due to limitations of the laboratory furnace, the sight-tube calibration permitted corroboration of the previous detector calibration only to a maximum temperature of 1400 K. To extend the calibration temperature range with the attached sight tube, a Type S (Pt-Pt10%Rh) thermocouple was inserted in a blind hole drilled into each side of a 6 mm thick aluminum oxide ceramic plate, and an acetylene torch was used to heat the rear face while the optical pyrometer imaged the front face. The ceramic plate was heated to approximately 2000 K. The front face temperature was estimated from the measured internal temperature. The sight-tube calibration using the blackbody cavity (up to 1400 K) and the ceramic plate heat source (up to 2000 K) enabled the detector assembly to be properly aligned with the sight tube, and confirmed the detector-only calibration performed previously up to 2000 K.

Exploratory measurements with the two-color pyrometer revealed the photodiode/amplifier components to be dependant on the ambient temperature. Laboratory experiments were performed to quantify this dependence. With a given blackbody source temperature, the two-color pyrometer detector assembly temperature was varied using a specially fabricated water jacket through which water of known temperature was circulated. The water temperature was varied over the anticipated range of the ambient temperature in the experiment. The temperature of the detector assembly was measured using a Type K thermocouple. The response of the photodiodes at both wavelengths (1.27 and 1.60 μm) was measured over the range of controlled detector temperatures. Interestingly, only the detector centered at 1.60 μm was found to have appreciable component temperature-dependent response. A mathematical relation, which accurately represents the temperature dependence of the amplifier sensitivity, was formulated and included in the pyrometer calibration. During testing in the glass furnace environment, the detector assembly was cooled using vortex tube coolers with adjustable flowrate in order to minimize the temperature excursions. Additionally, the temperature of the detector assembly was measured and documented for later use in data reduction. A statistical analysis of all calibration data, including the temperature dependence of the detectors, revealed an estimated uncertainty in measured surface temperatures of ±30 K.

The photodiodes in the two-color pyrometer were designed to output an amplified voltage proportional to the emissive power incident on the detector. Using Wien's approximation to Planck's blackbody function, the heated surface temperature was determined from the ratio of the two wavelengths chosen for use, and the ratio of the photodiode voltages (and hence, the emissive powers) at the two wavelengths:

$$T = \frac{C_2\left(1/\lambda_2 - 1/\lambda_1\right)}{\ln\left[\left(V_{\lambda_1}/b\right)/V_{\lambda_2}\right] + 5\ln\left(\lambda_2/\lambda_1\right) + a} \tag{4}$$

Here, l_1 and l_2 are the two wavelengths chosen, V_{λ_1} and V_{λ_2} are the measured photodiode voltages at the two wavelengths, and C_2 is Planck's second fundamental radiation constant with a value of 1.44 x 10^7 nm-K. The parameters a and b are calibration constants which account for *i)* the proportionality between photodiode voltage output and the incident emissive power (a), and *ii)* the ambient temperature sensitivity of the 1.60 μm detector (b). Both constants were determined from experiments in the laboratory prior to the glass furnace measurements. The expression for Wien's approximation included these calibration constants, determined from exhaustive calibration data taken over the full range of blackbody and ceramic heat source temperatures (900-2000 K) and detector body temperatures (286-318 K). The calibration related the measured voltage from both detectors and the detector body temperature to the imaged surface temperature.

There are two physical phenomena that may have affected the accuracy of the surface temperature measurements. First, the surface was assumed to be gray. In other words, the spectral emissivity of the glass surface was assumed to be identical at the two wavelengths. Although the spectral emissivity of the gray glass being produced during the testing was not measured, previous work has shown that the gray assumption is valid, particularly over such a narrow range of wavelength (Gardon, 1961). Second, glass is a semi-transparent medium, with emission possibly originating from a *layer* of glass instead of the surface alone. Recently, measurements of the spectral absorption coefficient for several different types of glass have been reported (Endrys, 1999; Nijnatten *et al.*, 1999a, 1999b). Based on these data it was determined that the spectral optical thickness (product of the absorption coefficient and the layer physical thickness) for the melt layer was approximately 400. Thus, emission from the glass originated from a layer less than one centimeter thick. Therefore, it was assumed that the temperature measurements reported are those of the glass surface.

Surface temperature measurements with the two-color pyrometer were taken in each of the six crown access holes, with Location 1 being nearest to the batch feed and continuing through Location 6, nearest to the working end of the furnace. Data were acquired during the reversal of the fifteen-minute regenerator cycle, when all of the burners were off for approximately 20 seconds. This enabled the unobstructed (no flame) measurement of the molten glass surface below. The estimated optical view of the two-color detector at the glass surface was a circular area approximately 9 cm in diameter. Detailed time-resolved measurements were obtained for all crown access holes, with the exception of Location 2, where only average surface temperature data were taken.

2.3.2 Physical Phenomena

Figure 17 shows a schematic (plan view) of the glass surface from the furnace batch feeder wall to the end of port 6 with respect to the general characteristics of the furnace, such as the location of the six portnecks and the batch feeder. This schematic was constructed from video observations made through the crown access holes and visual observations made through other furnace inspection ports located in the regenerators (along the centerline of the portnecks) and in the working end of the furnace looking toward the batch feeder. The video data delineated the areas of molten glass and of batch blanket, and were acquired using a high-resolution video camera with specialized filtered lenses attached to a water-cooled sight tube inserted through the crown access holes. The video probe apparatus allowed for a field of view of approximately 30 degrees, which provided clear information in the central region of the tank (2-2.5 m wide at the glass surface), but limited observations near the tank edges. Figure 17 also indicates additional information about some characteristics of the glass tank. These include (1) the location of the bubblers, which were used to enhance mixing of the molten glass, and (2) the approximate location of the "spring zone" where recirculating molten glass rose from lower regions of the tank to the surface, causing the glass surface temperature to reach maximum values in this region of the tank.

As illustrated in Figure 17, the batch blanket profile shows that the surface boundary between the batch blanket and molten glass along the furnace axial centerline was located in the vicinity of measurement Location 1, approximately 4.3 m from the end wall closest to the batch feeder. The schematic also indicates that batch material was nonexistent along the furnace centerline past Location 1 but extended along the sides of the furnace in the approximate profile shown, tapering in thickness along the furnace side walls until completely melted. This typically occurred in the vicinity of measurement Locations 3 or 4. As expected, the surface boundary between batch and molten glass is not completely steady. The location of the batch blanket varied slightly during furnace operation with several factors influencing its movement. The batch material was introduced intermittently to the furnace because of the operating characteristics of the batch feeder, causing the batch material to exit the feeder and enter the furnace in discrete clumps or "logs." In addition, the molten glass recirculation pattern and batch melting contributed to batch movement at the surface near the batch blanket/glass interface. Lateral movement of the batch blanket was also visually observed, with the unmelted batch blanket tending to shift cyclically with firing direction. This cyclic surface motion was observed to be toward the exit port side during firing, returning slightly more to the center during reversal, then shifting to the opposite port side as firing began in that direction. These factors were identified as contributors to batch blanket movement during furnace operation and to the intermittent existence of "batch islands," discrete smaller sections of batch material found near the boundary between the batch blanket and molten glass. The transient nature of the boundary between the batch blanket and molten glass was clearly established, although quantitative details of the contributing phenomena and specifics of their observed transient effects were not thoroughly studied.

Gases were liberated during melting and chemical reaction that occurred as the raw materials from the batch were processed. This was particularly true in the early regions of the furnace where melting was most intense. The generation of gases in the melt resulted in bubbles that rose and accumulated on the surface as foam. Foam was observed only near the boundary separating the batch blanket from the batch-free zone downstream in the melting section. Thus, foam was

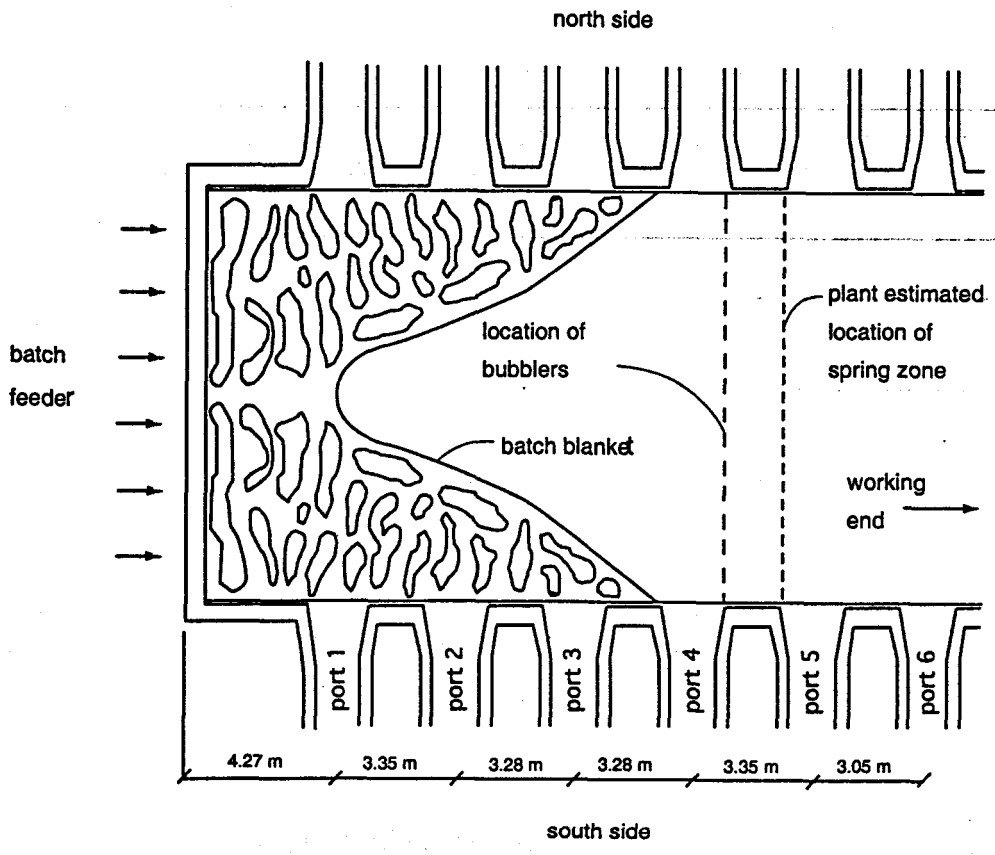

Figure 17. Schematic (plan view) of the glass surface in the furnace based on information obtained from specialized video data and visual observations through furnace inspection ports, indicating bubbler location and estimated spring zone position.

observed intermittently near measurement Location 1, but all subsequent holes (Locations 2–6) where surface temperature measurement data were collected were unobstructed by foam.

2.3.3 Time-Averaged Measurements

Glass surface temperatures measured at Locations 1-6, averaged over the 20-second reversal period, are shown in Figure 18. The lowest average surface temperature measured was at Location 1, nearest the batch feeder. The average temperature then increased sharply between Locations 1 and 2, continued to gradually rise to the peak measured temperatures at Locations 4 and 5, and then decreased at Location 6, nearest to the furnace working end.

Model predictions are also shown in Figure 18. These will be discussed in the Modeling Section but are shown here for comparison with the experimental data.

The trend in the measured average glass surface temperatures shown in Figure 18 is consistent and in good agreement with the model predictions, as well as the video and visual observations presented in Figure 17. The low average glass surface temperature measured at Location 1 was caused by the fact that this location was at the boundary of the cooler batch and the molten glass in a region where heat loss from the glass to the batch as well as to the tank walls was large. Both molten glass and batch material were viewed and measured intermittently at Location 1. Moving away from this region where batch and molten glass coexist, a sharp increase in the average measured glass surface temperature was observed along the furnace centerline between measurement Locations 1 and 2. In addition to the higher radiant heat flux received from the flame, Location 2 experienced less heat loss to the end wall and batch material. Approaching the spring zone, the measured average glass temperature continued to increase gradually between locations 2 and 3. The higher measured surface temperature at location 3 was due to (1) the recirculation flow pattern which brought hotter molten glass from the spring zone into that region, (2) the increase in firing rate and reduction of the overall excess air in the flame, and (3) lower heat loss to the furnace end wall and to the batch.

The highest average glass surface temperatures were at locations 4 and 5, the region of the spring zone. These peak temperatures were due to the recirculation pattern in the glass tank, the minimum heat loss from the glass to batch or end walls, and the highest firing rates and lowest excess air values. Repeated measurements during different reversal periods at these locations showed that the average surface temperature varied less than 76 K at location 4, which was closest to the operating bubblers, and less than 20 K at location 5.

At location 6, the average glass surface temperature was much lower than locations 4 and 5. Although there was essentially no heat loss to the batch at location 6, there was additional heat loss to the cooler working end of the furnace. Location 6 also experienced considerably less heat transfer from the combustion products than did the other locations, due to the reduced fuel flowrate in this port and significantly higher excess air (77%).

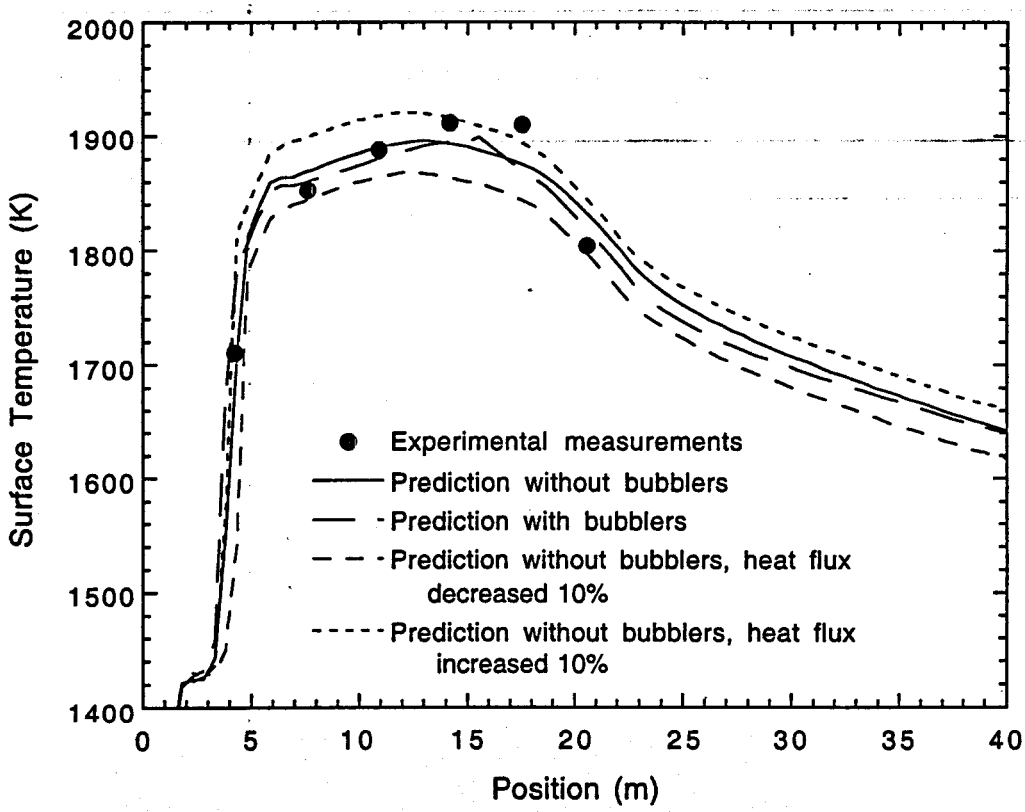

Figure 18. Comparison of measured and predicted average glass surface temperature profile along the furnace axial centerline in the glass tank.

2.3.4 *Time-Resolved Measurements*

Typical measurement traces of glass surface temperature measured during the 20-second reversal period when the flame was off are shown in Figure 19. The surface temperature at location 1 is seen to vary between 1440 and 1850 K during one 20-second reversal period. The temperature began relatively low (approximately 1600 K), and then increased slowly to a high plateau near 1820 K. It then dropped drastically over a period of about 8.5 seconds to below 1500 K before increasing slowly again to another high plateau of 1840 K for the remainder of the reversal period. This low-frequency, large-temperature variation is consistent with what might be expected if portions of the cooler batch blanket traversed the optical view area of the two-color pyrometer for a short time as they shifted position in the glass tank in the region of location 1. This batch motion arises from the phenomenon explained previously in the discussion of Figure 17, as well as the reverse velocities decelerating at the batch boundary, as shown in Figure 18. The higher temperature plateaus observed both before and after the lowest temperature interval were both relatively steady and consistent in magnitude with one another, suggesting the measurement of the molten glass surface temperature during these periods. The lower temperature intervals of the data trace were consistent with the measurement of the surface of cooler, unmelted or partially melted batch that existed as a continuous blank*et al*ong the centerline of the tank from the batch feeder to location 1. It is not known if the intermittently measured batch surface was due to optically viewing the movement of the edge of the continuous batch blanket or moving batch islands that were pulled by molten glass currents. It is known, however, that the lower measured surface temperatures at location 1 are consistent with batch surface temperatures predicted by the model and the visual observations and physical phenomena discussed previously. The time-resolved temperature signal measured in hole 1 was the only one to vary so widely during the reversal period. All other measured locations exhibit a more nearly constant surface temperature during reversal, because the surface temperature measurements at these locations were of molten glass only with batch material being nonexistent along the axial centerline of the furnace downstream of location 1.

The time-resolved surface temperature measurements obtained at access locations 3-6 indicate significantly less variation in molten glass surface temperature than at location 1. Locations 3, 4 and 5 all had similar profiles, exhibiting a steady gradual surface temperature decline over the duration of the reversal period while the flame was not present. The data at these locations, shown in Figure 19, thus illustrate the cooling of the molten glass surface during the brief non-firing period. Nominally, the surface temperature dropped 50-80 K over the no-flame reversal period. As would be expected, the slightly steeper decline in temperature took place when surface temperatures were the highest, such as near the beginning of reversal at locations 4 and 5, while the decline was more gradual when surface temperatures were lower.

The time-resolved temperature measurements of the glass surface at location 6, nearest to the glass tank exit, indicated a steady, nearly constant temperature profile that did not exhibit the same constant gradual decline as the other locations (3-5). It was noted again that location 6 was unique in the combustion cycle process, as reduced air/fuel flow occurred at this port location. The constancy of the measured surface temperature over time during reversal demonstrated that, at this location, the surface temperature of the molten glass was in a state of relative equilibrium, exhibiting

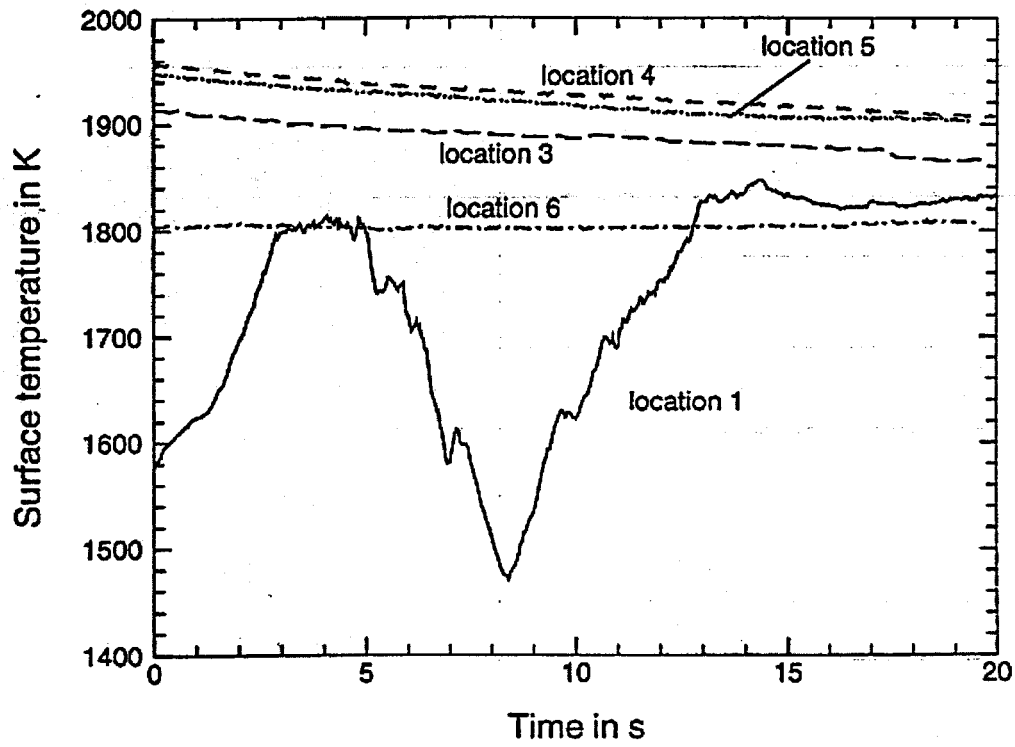

Figure 19. Typical time-resolved surface temperature plots acquired during reversal in locations nos. 1, 3, 4, 5 and 6.

no significant cooling during reversal. This was reasonable as the transient effects of firing and reversal periods were minimized at this port location, and the lower surface temperature in this region reduced net radiant heat loss.

2.4 Crown Flux

Experimental data from industrial glass furnaces found previously in the open literature were discussed earlier. Only one paper reported industrial-scale incident radiant heat flux measurements in the combustion space. The data reported in this instance consist of average wall radiant heat flux at the furnace wall (Cassiano *et al.*, 1994). Recently, limited measurements were obtained at the crown along one port location (Newbold, 1997), as discussed earlier. No spatially resolved data along the axial length of the crown were found. No time-resolved heat flux data have been reported, and no measurements have been reported during reversal when the flame is off.

Heat flux is a critical parameter in glass melting furnace design and operation. Heat flux plays an important role in determining glass quality and the refractory life. The variation of heat flux with location, as well as the transient effects due to firing and non-firing periods, must be known. Accurate measurements of heat flux are needed for model validation.

In this study, incident heat flux was measured through the six access holes in the crown of the furnace described previously. The information obtained includes both time-averaged and time-resolved data at all six locations during both reversal and firing modes of the regenerator cycle.

2.4.1 Instrumentation

The rebuilt furnace has been described previously. The input conditions for each port were the same as for the glass surface temperature measurements (see Table 4). Incident radiant heat flux measurements were performed using a hemispherical ellipsoidal radiometer with a response time of 30-60 seconds and a circular foil heat flux gage radiometer capable of higher frequency measurements up to 100 Hz. The ellipsoidal radiometer was described earlier and was used to obtain time-averaged measurements.

Both time-averaged and time-resolved incident heat flux data were obtained with the water-cooled, circular foil, heat flux gage radiometer, shown in Figure 20. This instrument consisted of a 1.7-m-long, 19-mm-diameter, brass, water-cooled jacket, encasing an inner signal wire tube with a detector head mounted at one end, and cooling water and signal lead connections at the other end. The detector head was approximately 45 mm in diameter with a 3-mm-diameter circular foil heat flux sensor located at the center of the detector face. The circular foil gage was also designed with a 180-degree view to measure total (full IR-spectrum) incident hemispherical radiant heat flux up to 850 kW/m^2. The instrument was calibrated up to 240 kW/m^2 with a voltage that was linear in relation to the total incident hemispherical heat flux to an accuracy of ±2%. The manufacturer indicated that this calibration line could be extrapolated up to 850 kW/m^2. The gage was designed for time-resolved measurements and exhibited non-attenuating response to input fluctuations up to a frequency of 100 Hz.

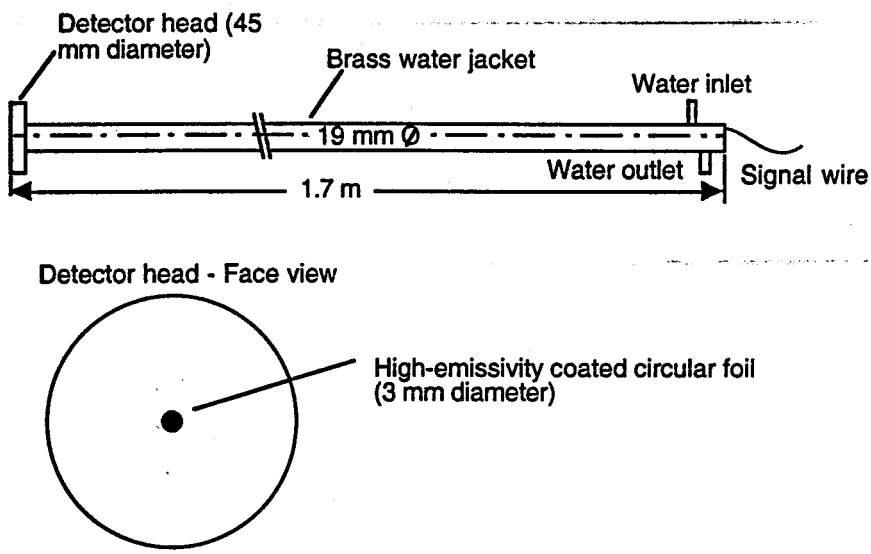

Figure 20. Schematic of the circular foil radiometer used for crown incident radiant heat flux measurements.

Measurements using the circular foil heat flux gage were performed in a manner similar to that previously described for the ellipsoidal radiometer. Adequate cooling water flow was first established, and the probe was then inserted through the crown access hole with the detector facing the glass surface below. The detector face was inspected between measurements and cleaned when necessary. The amplified output was between 0 and 2 volts. These measurements were acquired, digitized, and recorded using a computer-based data acquisition system with a 12-bit analog-to-digital converter, capable of high frequency data collection. Insulated, high-temperature, shielded cables were used to transmit the signal from the gage to the data acquisition system.

Data were obtained in each of the six crown access holes, with location 1 being nearest to the batch feeder and continuing through location 6, nearest to the working end. Time-resolved and time-averaged data were obtained during both firing and reversal cycles at each location. Heat flux measurements were acquired with the ellipsoidal probe in all of the crown access holes, except location 6. The time-averaged data acquired with the ellipsoidal radiometer were only obtained during firing periods because the radiometer response time exceeded the duration of the non-firing reversal cycles. Time-resolved data were obtained using the ellipsoidal radiometer over the entirety of several fifteen-minute firing cycles at location 4, with output recorded every 60 seconds, to examine lower frequency trends over complete firing cycles.

2.4.2 Time-Averaged Measurements

A schematic of the glass surface showing measurement locations was shown previously in Figure 17. Figure 21 shows a comparison of measured and predicted average incident radiant flux to the crown along the axial centerline of the furnace. The predictions will be discussed in the Modeling Section. They are shown here for comparison. Time-averaged data measured with both radiometers are shown.

There is good agreement between the results of the two probes, with differences of less than 12% at all locations. The largest differences were in the regions of highest heat flux. The ellipsoidal radiometer measurements were lower, consistent with the anticipated tendency of the ellipsoidal radiometer to measure somewhat low in the high heat flux range beyond its calibration range.

The lowest average heat flux values during firing periods were at location 1, where the batch blanket and end wall were cooler and had lower emissivities than the molten glass. Additionally, fuel flowrates at this location were about 12% lower than in ports 2-5 (see Table 4). Hence, radiation from the flame was lower in this region as well.

A sharp increase in the heat flux was observed between locations 1 and 2. Location 2 experienced less direct influence on incident radiant heat flux due to the previously discussed lower temperatures and emissivities of the cooler batch blanket and end wall, with a greater proportion and intensity of radiation received from the molten glass. Firing rates were also higher in port 2 than in port 1. In addition, the hemispherical nature of the measurement also included the contributions of adjacent ports.

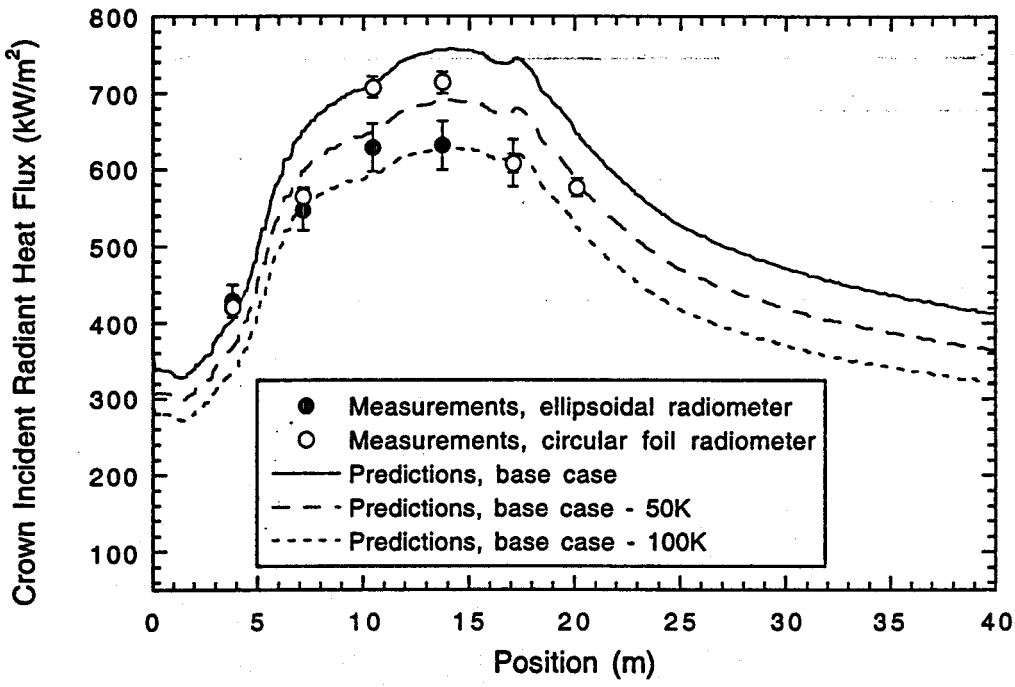

Figure 21. Comparison of measured and predicted average crown incident radiant heat flux along the axial centerline of the furnace during firing cycles.

The heat flux continued to rise to a maximum at locations 3 and 4. These ports had the lowest percentages of excess air (see Table 4), resulting in higher flame and glass surface temperatures and the highest levels of heat flux incident on the crown.

After the spring zone, the heat flux decreased. Although port 5 had a high fuel flowrate, it also had a high percentage of excess air (44%). Location 6 had a reduced fuel flowrate with significantly higher excess air (see Table 4). These effects, along with closer proximity to the end wall, resulted in lower heat flux at these locations.

2.4.3 Non-Firing Measurements

Time-averaged heat flux measured during firing cycles and the non-firing reversal periods are shown in Figure 22. During the non-firing periods, radiant energy incident on the crown comes from the molten glass, batch, furnace walls, and combustion products (principally soot, H_2O and CO_2). The molten glass surface is the principal radiation source during the reversal period.

Figure 22 shows that the shape of the profile measured during non-firing was similar to that measured during firing. The lowest heat flux was measured at location 1 due to the effects of the batch blanket and end wall. The peak crown incident heat flux measured at location 4 during non-firing was consistent with the estimated location of the spring zone where glass surface temperature was at a maximum.

As expected, the heat flux was higher during firing due to the emissive power of the flame. The highest increases due to the flame occurred at locations 3 and 4 where firing conditions were nearest to stoichiometric (see Table 4). Location 6 exhibited the lowest increase, due to the lower fuel flowrate and high excess air.

2.4.4 Time-Resolved Measurements

The high-frequency, circular foil heat flux radiometer was used to study the temporal variation in crown incident heat flux during firing cycles. Figure 23 shows the standard deviation in measured crown incident heat flux during firing. These data were calculated from time-resolved measurements acquired continuously over 30-60 seconds. The fluctuations were relatively small with a standard deviation of less than 6% of the mean flux at each location. For the most part, the variation appears to have been lowest at port locations with near-stoichiometric firing conditions. An exception is location 6, which had the highest percentage of excess air. The low variation in flux at Location 6 was probably due to the previously noted absence of significant radiation from combustion in this port.

The variation in crown incident heat flux at location 4 during typical firing cycles is shown in Figure 24. Although the ±5% uncertainty in heat flux measured with the hemispherical radiometer encompasses the full range of variation in incident heat flux over the 15-minute firing cycle, the qualitative trends in both cycles is reflective of all data taken over repeated firing periods. The profiles suggest that the crown flux increased during the first few minutes of firing due to increased radiant energy from combustion and presumably increased radiation from other surfaces (*i.e.* glass, walls) which were also being heated by the flame. Following this initial increase, the incident flux

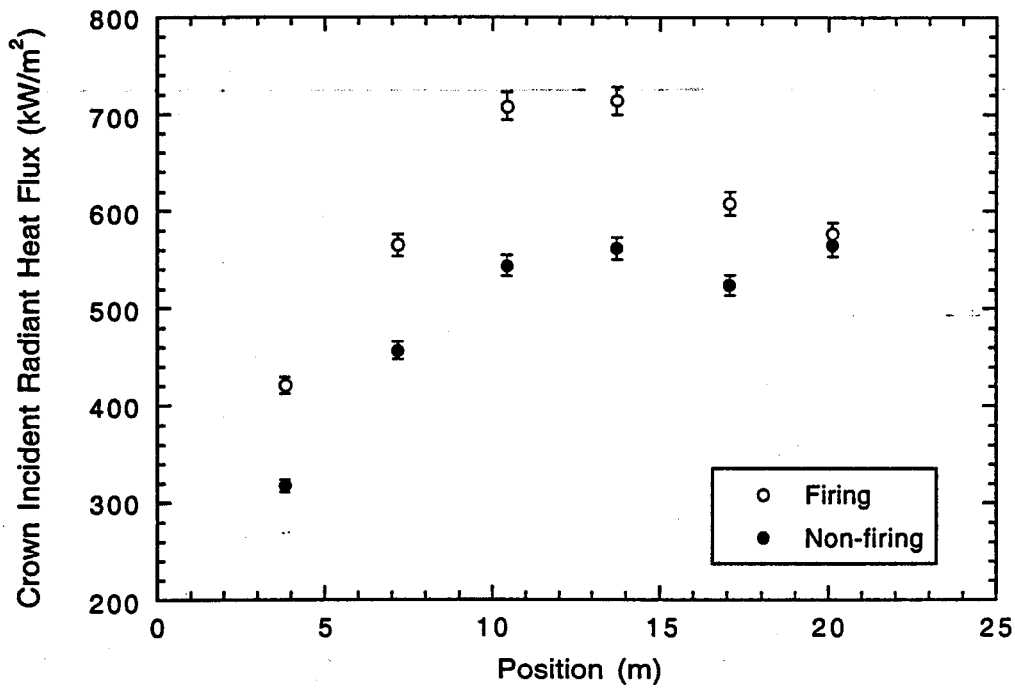

Figure 22. Comparison of time-averaged crown incident radiant heat flux measurements acquired during firing and non-firing periods using the circular foil radiometer.

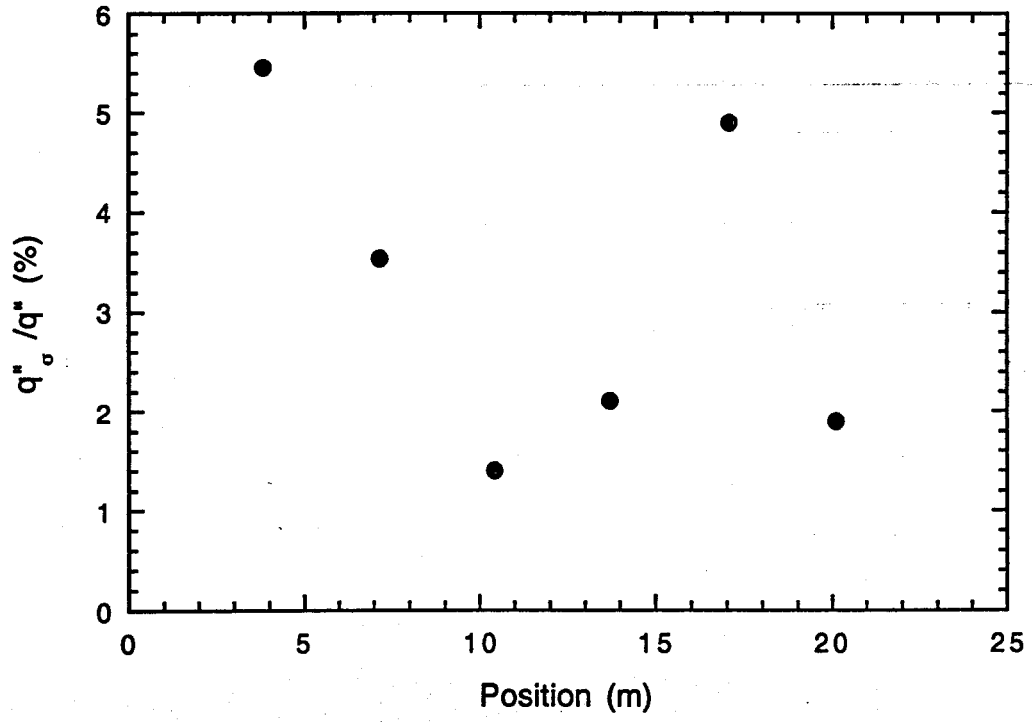

Figure 23. Average firing cycle variation (standard deviation) of measured crown incident radiant heat flux at all crown access locations.

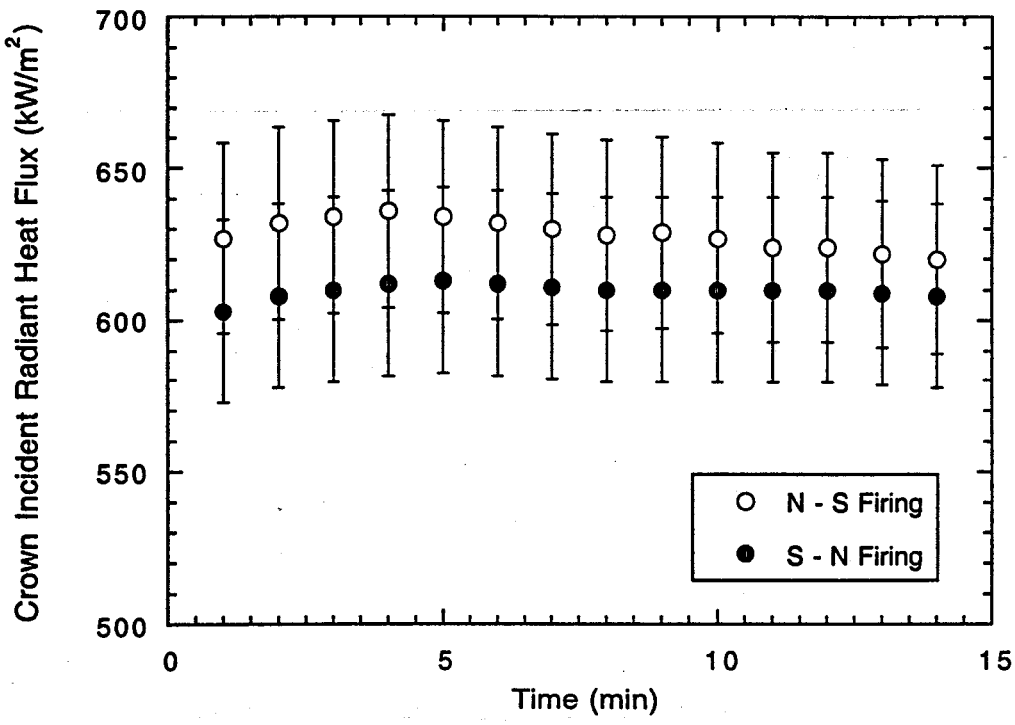

Figure 24. Cycle variation of measured crown incident radiant heat flux measured with the ellipsoidal radiometer at Location 4 for both firing directions over an entire firing cycle period.

ceased to increase and began to gradually decrease for the remainder of the firing cycle. This trend was caused by the regenerators. The regenerators were heated by the previous firing cycle exhaust and then used to preheat inlet combustion air when firing reversed direction, recuperating energy and improving the efficiency of the furnace. The observed trend suggests that the combustion air was preheated to higher temperatures during the earlier stages of the firing cycle, and as would be expected, the regenerators cooled as they transferred heat by convection to the cool inlet air. This effect was previously reported (Newbold *et al.*, 1997). Thus, during later stages of the firing cycle, less energy was available to preheat entering combustion air, resulting in lower inlet air temperatures. As a result, flame temperatures were slightly lowered, resulting in the observed decrease in heat flux radiated to the crown. The difference between the highest and lowest crown incident heat flux levels measured with the ellipsoidal probe over a single firing cycle at location 4 was approximately 10-15 kW/m^2 (3–4%). The within-firing-cycle variation shown in Figure 24 is typical of all locations. The nominal magnitude between high and low heat flux levels during a single 15-minute firing cycle at any given location was low—approximately 10-25 kW/m^2 (2-6%)—and within the experimental uncertainty.

Although the differences between the N–S and S–N firing data are within the ±5% uncertainty of the hemispherical radiometer, there is some indication in the data of Figure 24 that the local heat flux varied somewhat with firing direction. A review of all data acquired in this study indicated that the difference in measured heat flux levels due to firing direction did not follow an established pattern (*i.e.*, N–S consistently higher than S–N or visa versa), but rather, the data indicated that variation commonly occurred from cycle to cycle at a given location, independent of direction or other controlled factors. This type of variation is expected, considering the complexity of the furnace, the number of variables, and the accuracy of the instruments. The measured variation between firing cycles at a given location was modest, typically only slightly greater than the confidence level of the experimental data. The cycle-to-cycle variation did appear to be greatest in regions of highest heat flux.

Typical time-resolved data obtained using the circular foil heat flux gage during non-firing periods at several measured locations are shown in Figure 25. The measurements indicate that during the short reversal period, the crown incident heat flux at locations 2, 3, and 4 generally decreased, while the flux levels at locations 1 and 6 showed both slight increases and decreases.

The magnitude of incident heat flux variations over the reversal period shown in Figure 25 can be explained principally by the glass surface temperature behavior. A decrease in glass surface temperature of 60-70 K at a glass surface temperature of about 1900 K resulted in an approximate drop in crown incident heat flux of the magnitude seen in Figure 25. The variation in crown incident flux for location 6 observed in Figure 25 was significantly lower than for the other locations, as would be expected if the glass surface below this location exhibited more nearly constant temperature. Finally, the incident crown flux at location 1 displayed both slight increases and decreases over the reversal period, consistent with a slowly shifting melt/batch blanket/batch islands primary radiation source. Variations in incident radiant flux on the crown during the reversal period appear to have been caused primarily by corresponding changes in the glass surface temperature at each location.

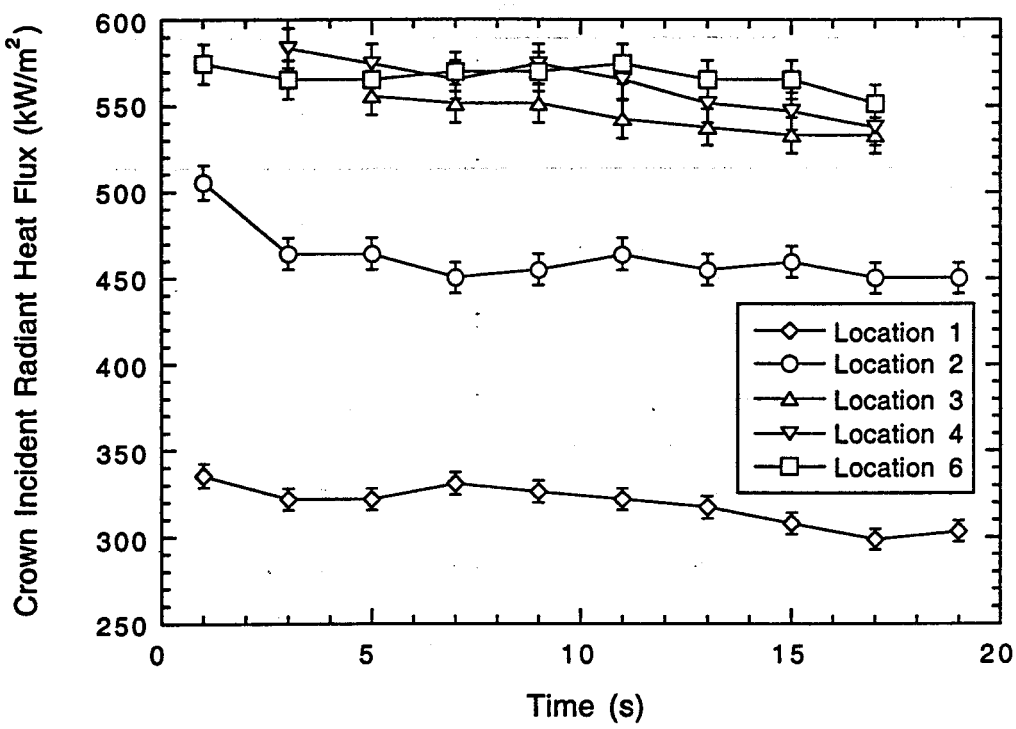

Figure 25. Typical time-resolved data of measured crown incident radiant heat flux at several locations during non-firing reversal periods.

3. MODELING

Another important objective of this study was to develop a mathematical model of the thermal phenomena in a glass furnace. This facet of our work first started with the modeling of the combustion process in a single port module, later extending to two adjacent modules and finally a full combustion space simulation. Later, in two or three major steps, this modeling work was extended to include the entire combustion space coupled with the batch feeding and melting process together with the flow in the glass tank. The experimental measurements played a vital role in validating these models, providing confidence in their application in existing furnace evaluation and new design investigations. This section of the report summarizes all of the main accomplishments in the modeling area. Because of the unique availability of the experimental data, several of the results presented in this section will be compared to the measured data where applicable.

Batch melting in glass furnaces is a complex process (Hrma, 1988). Batch is fed into the furnace from a doghouse, where it forms a continuous blanket on the surface of the molten glass. As the batch melts, the blanket dissolves into a discontinuous pattern of islands called "logs." Batch coverage on the glass surface is an important design and operation parameter because it influences the heat transfer, the melting, the velocity patterns of the molten glass, and (consequently) the product quality.

The use of mathematical modeling in glass furnace design and analysis is growing in acceptance, as shown by several recent reviews (Choudhary, 1997, 2000; Choudhary and Huff, 1997). These modeling efforts include the combustion space, melt tank circulation, and batch melting. Modeling studies of glass furnace combustion and glass flow processes include Cassiano *et al.* (1994), Boerstoel *et al.* (1994, 1995), Carvalho *et al.* (1985, 1987, 1988, 1990a, 1990b, 1992, 1995c), Ungan and Viskanta (1987), Gosman *et al.* (1980, 1995), Chen and Goodson (1980), Mase and Oda (1980), McConnell and Goodson (1979), Megahed (1978), and Novak (1980). Batch melting models include Fuhrmann (1973), Mase and Oda (1980), Hrma (1982), Carvalho (1983), Viskanta and Wu (1983), Ungan and Viskanta (1986), and Wang (1998). These studies have mainly focused on simulating the batch melting process separately, without coupling to the combustion chamber and the glass. Recently, computer models of the combustion space, melt tank circulation, and batch melting have been coupled to form an integrated model capable of predicting the thermal phenomena occurring in industrial glass-melting furnaces (Wang, 1998; Carvalho *et al.*, 1995, 1997; Wang *et al.*, 1998, 1999; Prasad *et al.*, 1999; Hoke, 1999). Unfortunately, these studies have been carried out with only limited practical data from industrial furnaces for model evaluation, and the accuracy and limits of the models are not well established.

3.1 Combustion Space

Thermochemical processes in the combustion chamber and glass tank are coupled through mass and heat transfer. Uncoupled simulations of the combustion chamber were performed for a port module, assuming symmetry between ports, and for the full furnace. In the uncoupled simulations, the temperature and emissivity of the glass tank surface were provided as boundary conditions, and the formation of gas (primarily CO_2) in the batch reactions was neglected.

3.1.1 Port Module Simulations

A one-port segment of the side-port, 550-ton-per-day, gas-fired, flat-glass furnace described previously (see Figure 1) is shown in Figure 26. In the one-port module, symmetry between the ports was assumed for simplicity. The dimensions of the furnace and locations of the access holes were shown previously in Figure 1. The access holes, numbered from 1 to 6, were located at 1.1, 2.3, 3.4, 4.4, 5.3 and 7.6 m from the breast wall.

Two state-of-the-art turbulent combustion codes, PCGC-3 (Hill and Smoot, 1993) and FLUENT 4, were used to predict the turbulent, reacting flow field in the one-port segment. PCGC-3 was developed as an academic research tool for modeling pulverized coal gasification and combustion but is generalized to include gaseous combustion and non-reacting flows. FLUENT 4 is a widely used commercial code that is applicable to a variety of reacting and non-reacting flows. Table 5 summarizes the main features of both codes. The key difference between the two codes is the grid type. The grids are both structured, but FLUENT 4 uses body-fitted coordinates and PCGC-3 uses regular, orthogonal coordinates. Hence, FLUENT 4 was able to model the curved and irregular surfaces of the crown and portnecks smoothly, while PCGC-3 required stair-step boundaries.

Grid independence was determined by performing simulations with an increasing number of cells until the solution was not affected. Grid independence in the one-port module was achieved with 62,100 cells (100 x 23 x 27 grid) in PCGC-3 and with 101,472 cells (151 x 32 x 21 grid) in FLUENT 4. The simulations required approximately 30 cpu-hours on an HP 9000/735 workstation.

Boundary and inlet conditions are listed in Table 6. Glass surface temperature and emissivity were arbitrarily assumed based on experience. The composition of the fuel was shown previously in Table 1. In the FLUENT 4 simulations, the O_2 in the fuel was replaced by CO_2. This modification increased the equivalence ratio by 0.5% and was necessary because of inherent restrictions in the FLUENT 4 code. The fuel-flowrate and burner area were used to determine the inlet velocity, which was assumed uniform. Inlet conditions were kept as similar as possible in both codes, but some minor variations occurred because of the different grids.

The temperature and flowrate of the inlet air were determined from measurements (Newbold *et al.*, 1997; McQuay *et al.*, 2000). The velocity profile (with the total air flow scaled on a port-by-port basis to agree with the plant-measured total air-flowrate) was assumed to vary stepwise vertically within the portneck with no horizontal variation. The equivalence ratio determined from the plant-supplied air and fuel flowrates (0.66 for port 3) was inconsistent (*i.e.*, too much combustion air) with measurements of O_2 in the exhaust (McQuay *et al.*, 2000). The sensitivity of the predictions to uncertainty in the equivalence ratio was investigated by reducing the air flowrate to a value consistent with the exhaust measurements, yielding an equivalence ratio of 0.81. The reduction in air flowrate was accomplished in two separate ways: (1) Reducing the velocity by 17% ("reduced air" simulation) and (2) reducing the portneck area (height) by 15% ("reduced height" simulation). Considerable buildup occurred inside the portneck over the furnace lifetime (McQuay

Table 5. Maj or characteristics of PCGC-3 and FLUENT codes.

Submodel	PCGC-3	FLUENT 4
Turbulence	Standard k-ε Nonlinear k–ε	Standard k–ε RNG
Gas Combustion	Mixture Fraction / PDF Chemical Equilibrium	Mixture Fraction / PDF Chemical Equilibrium
Radiative Heat Transfer	Discrete Ordinates	Discrete Transfer
Optical Properties	Spectral-LineWeighted-Sum-of-Gray-Gases (SLW)	Weighted-Sum-of-Gray-Gases (WSGG)
Solution Algorithm	TEACH Differencing SIMPLE Family	TEACH Differencing SIMPLE Family
Grid	Structured, Orthogonal	Structure, Non-orthogonal, Curvilinear
Equations	Newtonian, Navier-Stokes Eulerian, Finite-difference Favre-averaged	Newtonian, Navier-Stokes Eulerian, Finite-difference Favre-averaged

Table 6. Boundary and inlet conditions for the base case model.

Portneck Walls	
Emissivity	0.6
Heat Flux (W/m^2)	0.0
Crown and Furnace Walls	
Emissivity	0.6
Temperature (K)	1910
Glass Surface	
Emissivity	0.9
Temperature (K)	Piecewise linear varying from 1810 in the middle to 1760 at the furnace walls
Air Inlet	
Temperature (K)	1391
Turbulence Intensity (%)	10.0
Characteristic Length (m)	0.29
U-Velocity ($m\ s^{-1}$)	Velocity data measured in Portneck 3 for N-S burn
Fuel Inlet	
Fuel	Same as in Table 1 except assume O_2 is CO_2
Temperature (K)	283
Turbulence Intensity (%)	10.0
Characteristic Length (m)	0.022
U-Velocity (m/s)	61.42
W-Velocity (m/s)	-61.42

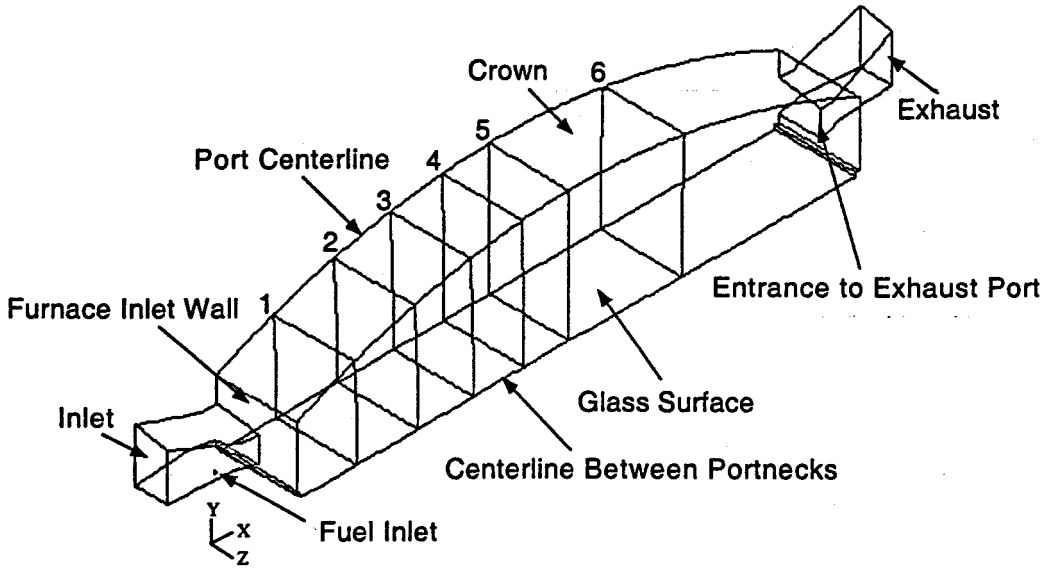

Figure 26. Schematic representation of the single portneck model.

et al., 2000), and it is certain that the portneck area was reduced. Based on photographs of a typical portneck after the furnace was shut down (just prior to its rebuild), the flow restriction was estimated to be approximately 15%. The *reduced air* and *reduced height* simulations investigated the sensitivity of the model predictions to variations in stoichiometry (due to air flow uncertainty) and portneck geometry (due to buildup).

Flow Structure

Figure 27 shows measured and predicted transverse velocity profiles in holes 2, 4, and 6. Generally, the flow was characterized as a dominant flame jet spreading over the glass surface, with a large recirculation zone near the crown. Both codes predicted velocity profiles that agree reasonably well in both magnitude and shape with the experimental data. The FLUENT 4 predictions agreed more closely with the measurements. As expected, the *reduced air* and *reduced height* parametric predictions yielded slightly lower velocities in the core of the flame jet. The uncertainty of the experimental data was estimated to be 10% in the flame region and 100% in the recirculation zone (Newbold *et al.*, 1997; Newbold, 1997).

Gas Temperature

Figure 28 shows measured and predicted gas temperatures at the two holes on the firing side of the furnace. Temperature measurements at other holes were not available due to experimental difficulties (Newbold *et al.*, 1997; Newbold, 1997). Both codes had large discrepancies with the measured values (400-600 K). Significant differences also existed between the predictions of the two codes.

There are several possible explanations for the discrepancies between the measurements and predictions. First, the inlet velocity boundary conditions may have been in error. The measurements on which the inlet velocities were based were made upstream of the actual boundary location and along only a single vertical line (see Figure 2). Second, the port-by-port stoichiometry values were scaled from overall furnace data based on the integrated flows over the portneck area, assuming no horizontal variation. Third, the portneck and crown surfaces were approximated with stair-step boundaries in PCGC-3. Fourth, chemical reactions were assumed to be limited by mixing and not by kinetics. This is a state-of-the-art assumption for turbulent combustion modeling that was implemented in both codes. Kinetic effects for some reactions, such as conversion of CO to CO_2, may have been significant. Fifth, the assumed batch coverage, glass and batch surface temperatures, and emissivities may have been in error. And sixth, soot radiation was neglected in the predictions. The FLUENT 4 results demonstrate the sensitivity of predicted flame structure to portneck geometry and combustion stoichiometry, as evidenced by comparing the *reduced air* and *reduced height* simulations with the base case.

Oxygen Concentration

Figure 29 shows measured and predicted oxygen concentrations. FLUENT 4 did better at predicting the shape of the measured profile, while PCGC-2 did better at predicting the magnitude. Exhaust oxygen was significantly lower for the *reduced air* and *reduced height* simulations, consistent with the measurements.

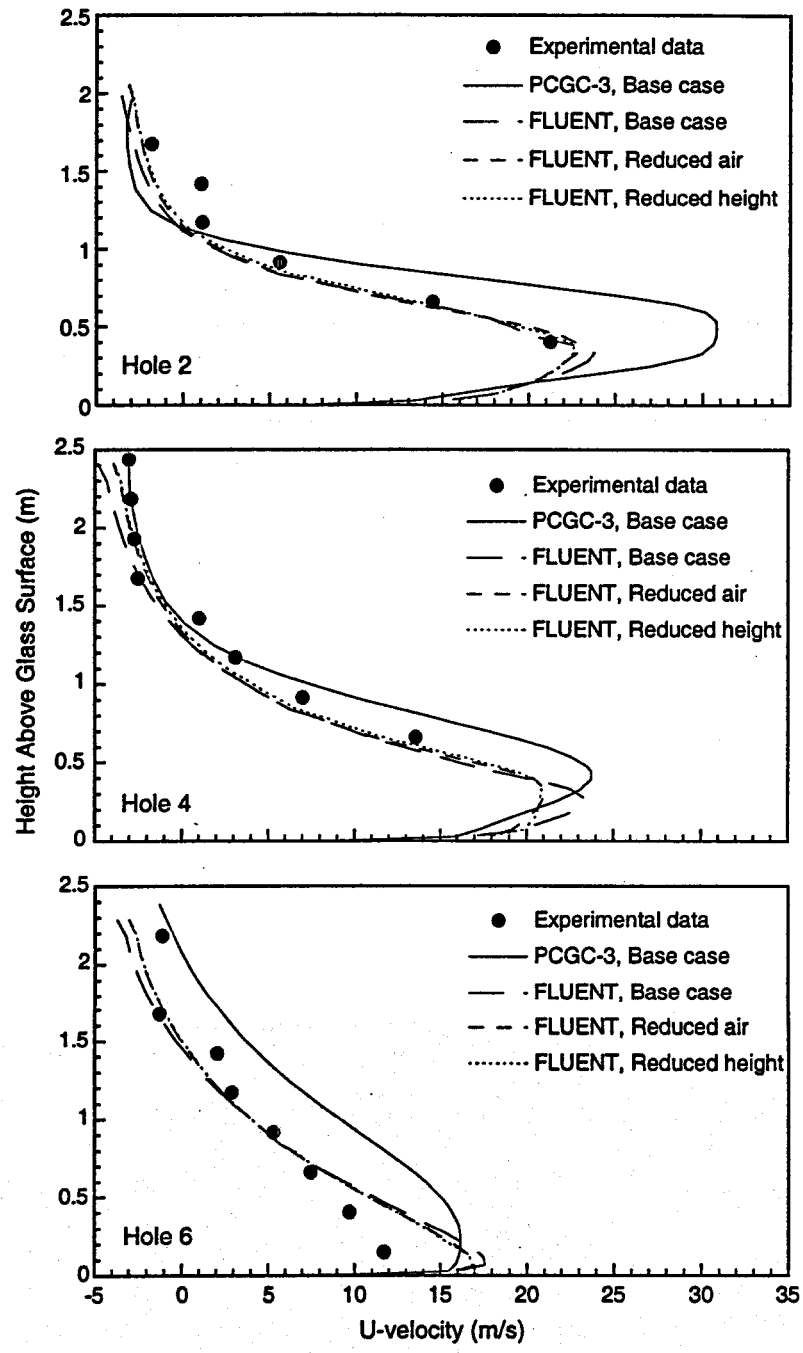

Figure 27. Comparison of measured and predicted *u*-velocities in holes 2, 4 and 6.

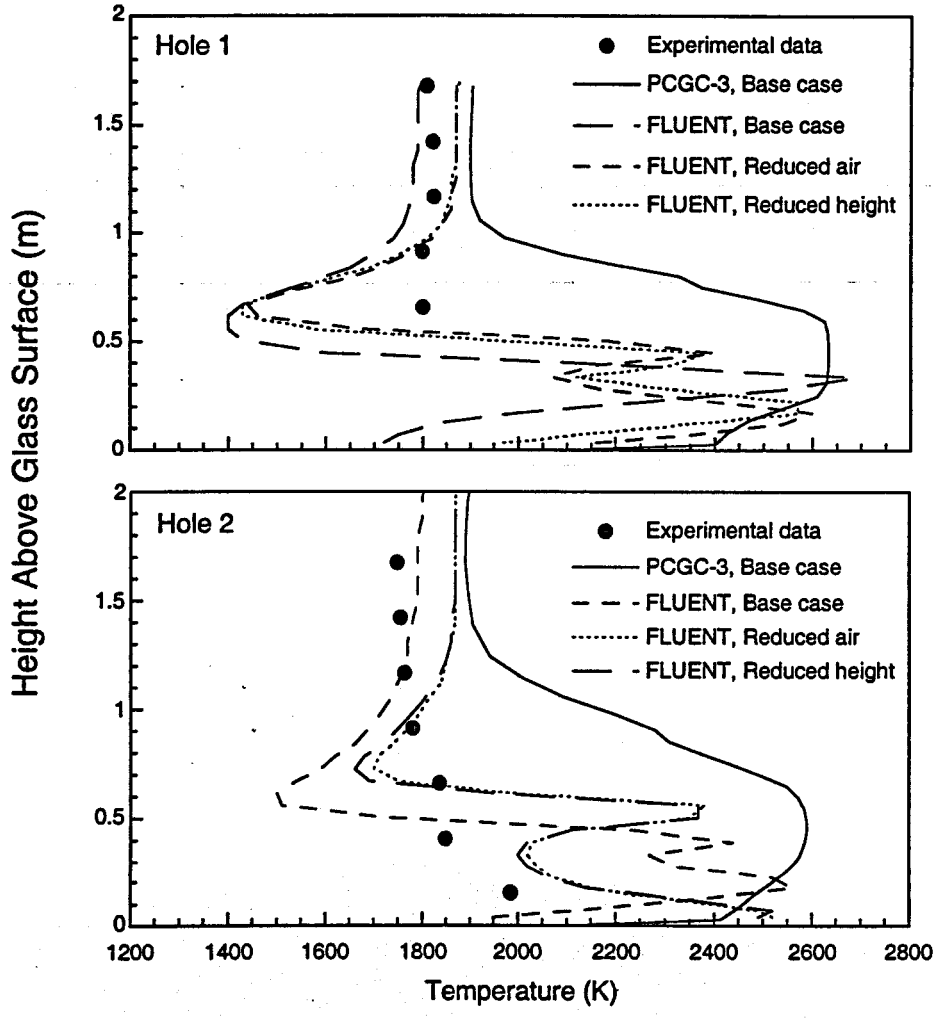

Figure 28. Comparison of measured and predicted gas temperatures in holes 1 and 2 for the north-south firing configuration.

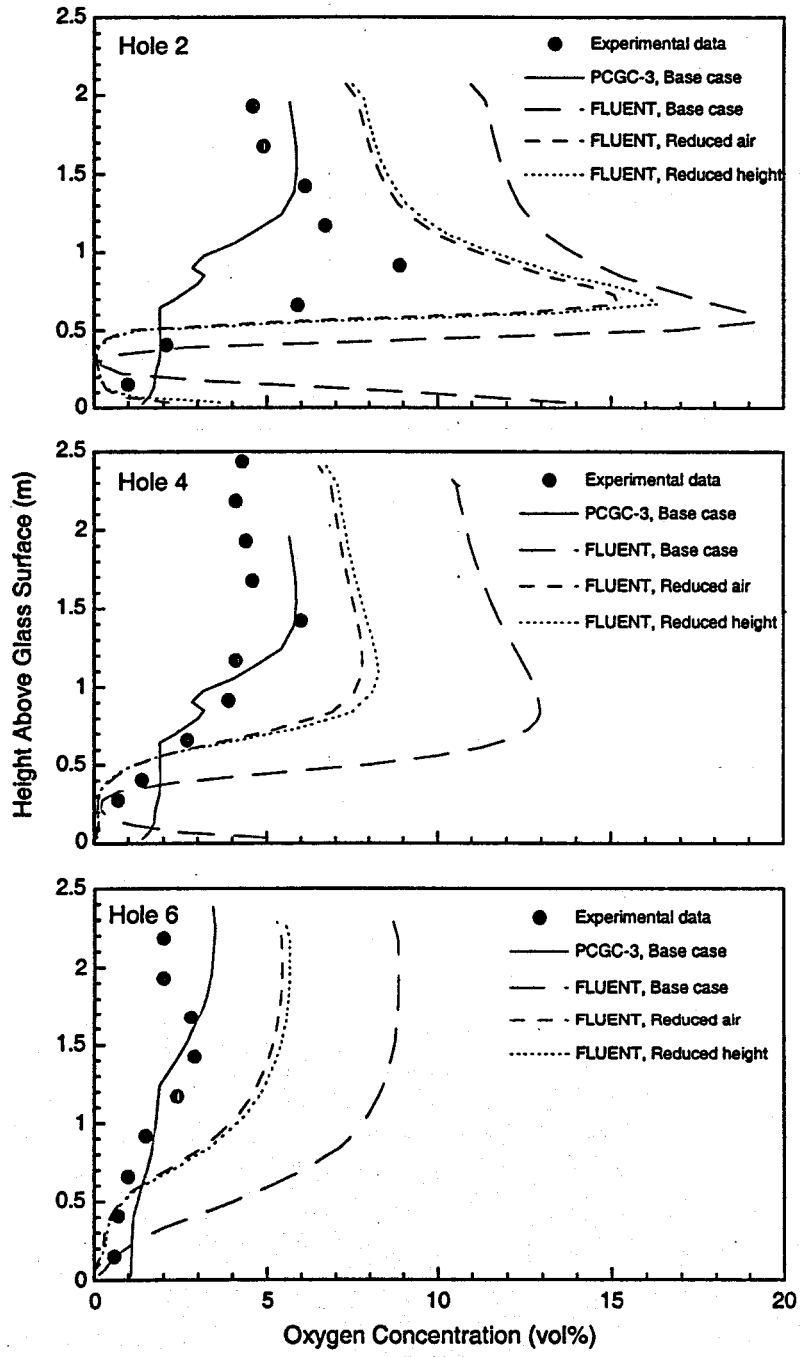

Figure 29. Comparison of measured and predicted oxygen concentrations (vol % dry) in holes 2, 4 and 6.

Carbon Monoxide Concentration

Figure 30 shows measured and predicted CO concentrations. The flame core near the glass surface is indicated by the high CO concentrations found there. The PCGC-3 predictions are substantially lower than FLUENT 4, and exhibit a thicker flame. Reducing excess air in the flame (*reduced air* and *reduced height* simulations) increased the flame thickness. The high FLUENT 4 predictions in the core region are consistent with the experimental data, since the measurements in this region exceeded the 40,000-ppm limit of the instrument (Newbold *et al.*, 1997; Newbold, 1997).

The average predicted exhaust CO concentration weighted by the mass flowrate was only 1680 ppm, while the average measured concentration was 8125 ppm. Higher exit CO concentrations could have resulted from *i)* incomplete mixing of fuel and oxidizer, *ii)* insufficient time for complete combustion, and/or *iii)* fuel-rich combustion. Higher exit CO concentrations also suggest that a longer flame occurred in the actual operation than was predicted. The discrepancies between measured and predicted CO values may be due in part to the assumption of local instantaneous equilibrium. Neglecting kinetic effects could explain why a more rapid decay of CO was predicted than measured. The higher predicted temperatures seen in Figure 28, especially downstream in the furnace, would also result in a faster predicted decay of CO.

Carbon Dioxide Concentration

A comparison of predicted and measured CO_2 concentrations for the two codes is shown in Figure 31. Again, the predicted trends seem qualitatively correct, but the magnitudes disagree. The profiles predicted with FLUENT 4 have more structure near the glass surface. The predicted values were generally lower, probably due to the fact that nearly one-half of the CO_2 produced in a glass furnace may originate from the reactions in the glass (Newbold *et al.*, 1997; McQuay *et al.*, 2000). Most of the CO_2 generated in the melt occurs near the batch feeder (*e.g.*, portnecks 1-3). This discrepancy with the experimental data could have occurred because this source of CO_2 was neglected in the predictions.

Radiative Flux

Predicted and measured profiles of incident, radiative flux at the crown are shown in Figure 33. Given the discrepancies in predicted temperature and CO_2 concentration, the good agreement may seem fortuitous. However, 60-90% of the radiant heat flux incident on the crown originates from the glass surface (Hayes *et al.*, 2001). If the glass surface temperature and emissivity are accurate, the predicted crown flux will exhibit good agreement with the measured data even when the gas temperature and CO_2 concentration are poorly predicted. The need for accurate glass surface thermal boundary conditions for the combustion space underlines the need to account for coupling between the combustion chamber and the glass tank.

Sensitivity Analysis

An analysis was performed with the combustion space model to determine the sensitivity of predictions to prescribed input conditions. This sections summarizes the results of this study.

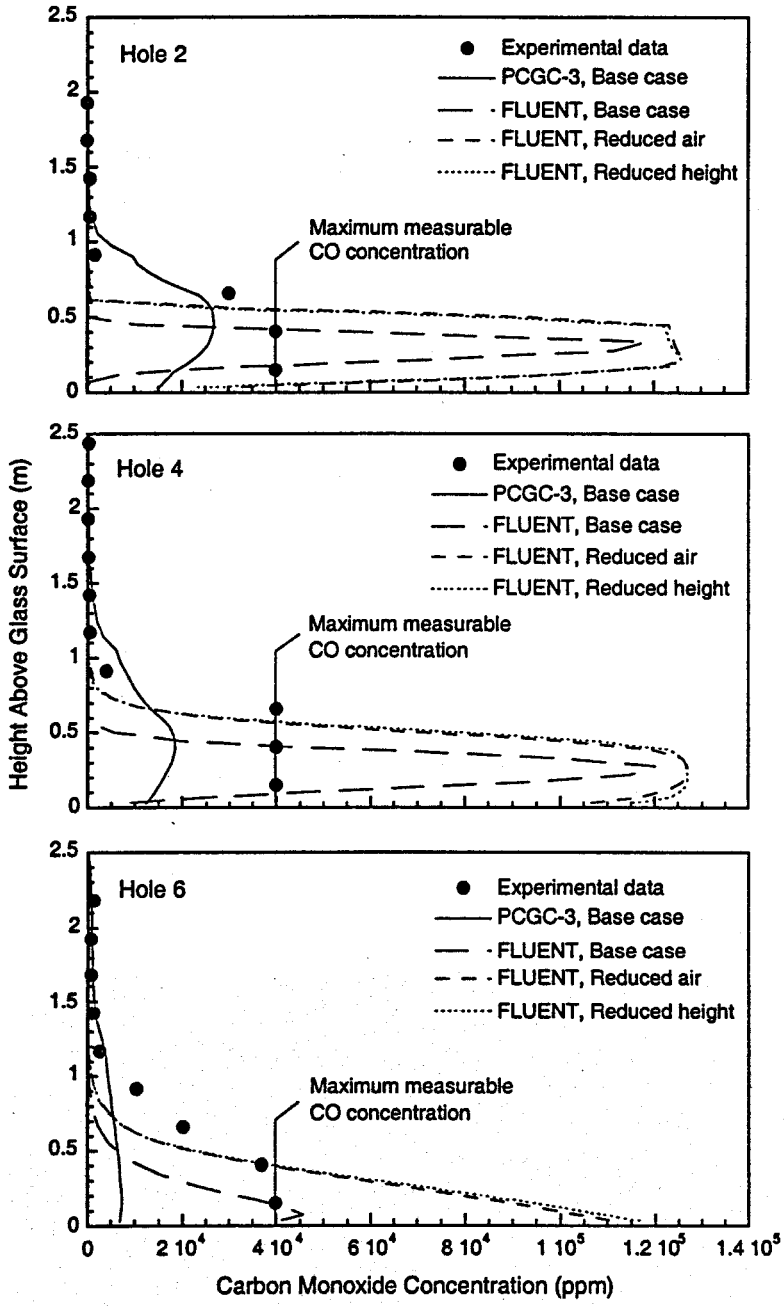

Figure 30. Comparison of measured and predicted CO concentrations (ppm dry) in holes 2, 4 and 6.

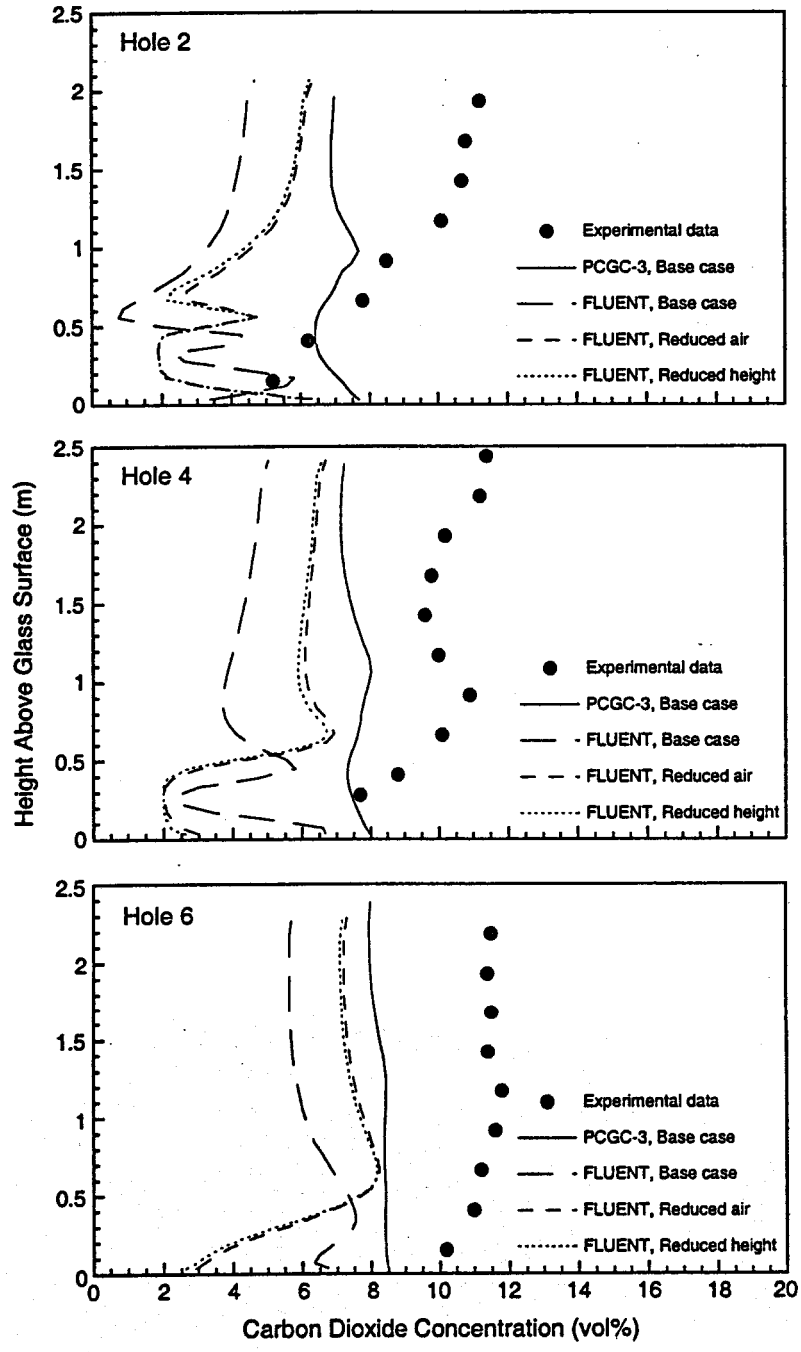

Figure 31. Comparison of measured and predicted CO_2 concentrations (vol % dry) in holes 2, 4 and 6.

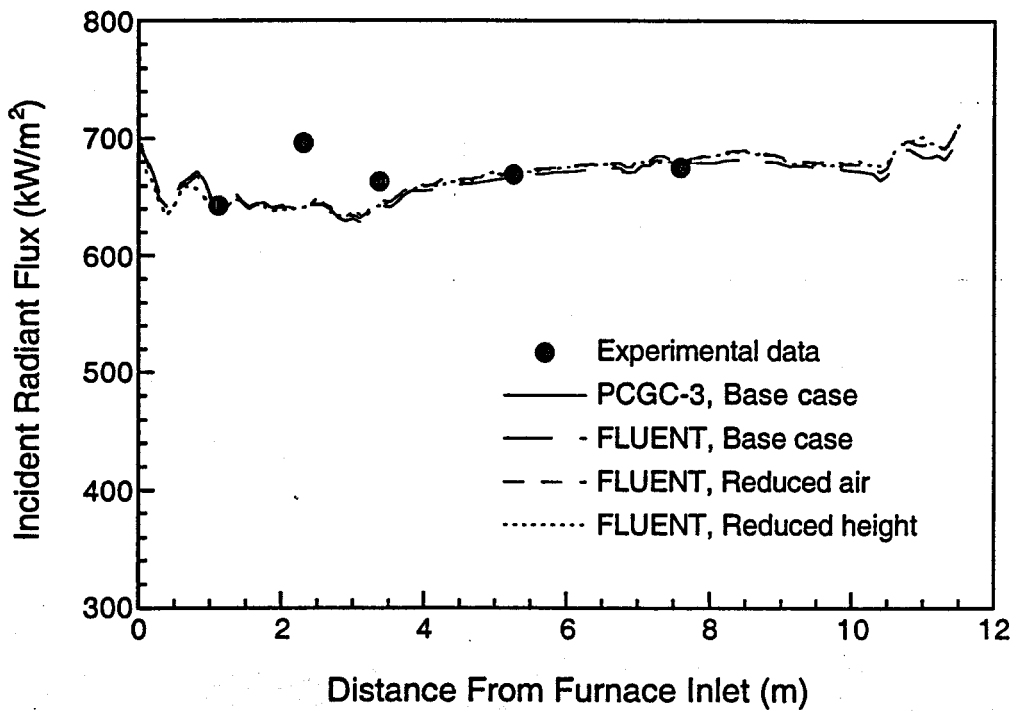

Figure 32. Comparison of the predicted and measured incident flux on the crown.

Inlet Velocities. Two cases were simulated to investigate the sensitivity of the predictions to inlet velocity distribution. In the first case, the velocity was 7.9 m/s at the portneck centerline, with a step-increase to 15.9 m/s halfway across the port. Total mass flowrate was kept constant. This inlet velocity profile caused the flame to diverge from the port centerline, opposite to the observed trend (a converging flame). The exhaust temperature was approximately 30-100 K lower than the base case, and the CO level was approximately 10,000 ppm lower. In the second case, the inlet velocity was 14.9 m/s at the portneck centerline and 6.9 m/s halfway across the portneck, again maintaining the same total mass flowrate. This condition forced the flame along the centerline further upstream than what was observed in the base case, affecting the near-glass region.

Inlet Turbulence. Turbulence intensity and characteristic length were varied to investigate the sensitivity of the predictions to the inlet turbulence levels. In the base case, the turbulence intensity of both the air and fuel streams was set at 10%. The characteristic length of each inlet stream was set at the respective hydraulic radius. The analysis of the inlet turbulence level revealed some sensitivity to the turbulence intensity and characteristic length of the streams. As expected, the most significant effects were observed when the parameters were increased above the base model values. Increasing the parameters caused the flame to diverge from the port centerline. It was further noted that the inlet portnecks converged geometrically, which would tend to suppress turbulence at the furnace inlets. Decreasing the turbulence intensity and characteristic length from their base-case values, in general, had little or no effect on the predicted flow field.

Adiabatic Crown/Walls. Changing the crown and furnace wall thermal boundary condition from 1910 K to adiabatic lowered the crown temperature approximately 70 K and resulted in a 40% reduction in crown incident radiative flux. Gas temperatures changed by 40-50 K (higher and lower) in different regions of the furnace.

Wall Emissivity. Increasing the crown emissivity from 0.6 to 0.8 had a negligible effect on the flow field and decreased the incident flux on the crown by approximately 3%. The gas temperatures in the furnace were 50 K lower at the end of the flame and approximately 100 K higher in the recirculation zone. The exit temperatures were an average of 10 K higher. The CO concentrations were 30,000 ppm lower in the flame region but similar to the base case elsewhere. The increase in wall emissivity also resulted in less uniformity of radiative flux to the crown.

Adjacent Port Interactions. The one-port module neglected interactions between adjacent ports. A two-port module was created in FLUENT 4 to investigate these effects because each port operates at a different flowrate. A grid with 185,150 control volumes (115 x 35 x 46) was used. The air and fuel flowrates in the two ports differed by 13.5 and 9.3%, respectively. The predicted interaction between the ports was confined to the tail and shared edge of the adjacent flames and was not seen to be a significant factor in predicting the combustion process. The results agreed reasonably well with the one-port module predictions.

Effect of Soot

The effect of soot radiation was investigated with FLUENT 4. Model parameters were adjusted within acceptable ranges so as to produce soot concentrations consistent with experimental values for a methane flame. When soot was included, the average exhaust gas temperature decreased and the average radiative heat flux to the glass increased. The 15% decrease in average gas temperature

had a significant impact on the predicted NO concentration at the exit, which decreased by more than 55%. Including soot also improved the heat flux uniformity, defined as

$$\text{Heat Flux Uniformity} = \frac{\sqrt{\int_A \left(q''_{rad} - \overline{q''_{rad}}\right) dA}}{\int_A q''_{rad}\, dA} \tag{5}$$

Values of uniformity greater than 0 reflect increasingly non-uniform heat flux delivered to the glass melt. Of course, a value of 0 may not be optimum for glass production. Contours of CO concentration at the burner level (not shown) clearly showed a much broader and longer flame for the simulation with soot. Results for the simulations with and without soot are summarized in Table 7.

Other information shown in Table 7 is fuel utilization efficiency and combustion efficiency. Fuel utilization efficiency is the fraction of the fuel's heating value that is transferred to the glass melt. Combustion efficiency is the percent conversion of carbon in the fuel to CO_2 and was evaluated by the concentration of CO in the exhaust stream. Higher concentrations of CO in the exhaust indicate lower combustion efficiency.

Oxygen Lance

The use of an oxygen lance to reduce NO_x formation was investigated using the geometry shown in Figure 33. Three cases were investigated: (1) 10% of the total furnace oxygen flow was introduced as pure O_2 in the lance with a global furnace stoichiometry of 119% theoretical O_2 (the remaining oxygen was introduced in the conventional portneck flow in the form of preheated air with the corresponding amount of nitrogen), (2) 10% of the furnace oxygen flow was introduced in the lance with a global furnace stoichiometry of 107% theoretical O_2, and (3) 30% of the total furnace oxygen flow was introduced in the lance with a global furnace stoichiometry of 119% theoretical O_2. The oxygen lance velocity was approximately 50 m/s in each case. This velocity was found to ensure adequate penetration into the furnace. The oxygen lance was intended to stage the combustion by delivering the oxidizer to the fuel stream over the length of the flame, resulting in lower flame temperature and reduced contact time between oxygen and nitrogen.

As shown in Table 7, the lance increased the predicted average exhaust gas temperature (soot radiation included) by 7%. Even though the nitrogen in the furnace was reduced, this increase in temperature was significant enough to increase the NO_x formation by more than 95%. With 30% O_2, however, the results suggest that a greater fraction of the oxygen delivered to the flame later in the combustion process may offer benefits in terms of reduced NO_x formation. Average radiative heat flux to the glass also decreased when increasing the overall theoretical air, indicating a decrease in the heat transfer efficiency in the furnace. The effect of the local concentration of oxygen in the NO_x formation process is also illustrated by the lance calculation at a reduced excess air setting (107% TA). In this case, although the exit temperature was about the same for both 10% lance cases, the NO_x level dropped for the richer case.

Table 7. Summary of predicted figures of merit for the NO_x reduction technologies studied.

	Base Case (w/soot) 119% TA	Base Case (no soot) 119% TA	10% O_2 Lance 119% TA	10% O_2 Lance 107% TA	30% O_2 Lance 119% TA	Oxy/Fuel pure O_2 105% TO_2	Oxy/Fuel 90% O_2/ 10% N_2 105% TO_2
Exhaust Temp. (K)	1897	2018	2046	2036	1867	1822	1822
Exhaust Species:							
CO_2 (%)	9.8	9.3	10.4	12.3	12.6	29.7	28.2
CO (ppm)	149	415	1070	2235	340	175	220
O_2 (%)	3.7	3.8	4.1	0.0	4.7	11.4	8.7
NO_x (ppm)	1823	6247	4255	3466	3835	4583	7300
NO_x (lb/ton)	10.6+	36.5+	23.8+	16.0+	16.8+	2.5	4.4
Average Radiative Flux to Glass (kW/m^2)	124	102	105	115	129	110	107
Fuel Utilization Efficiency (%)	50.6	40.6	42.8	46.9	52.6	62.0	61.2
Heat Flux Uniformity*	0.28	0.41	0.31	0.28	0.17	0.25	0.33

*Calculated from predictions of local incident radiative flux on the glass according to Equation (5)

+Calculated assuming uniform firing rate among six ports

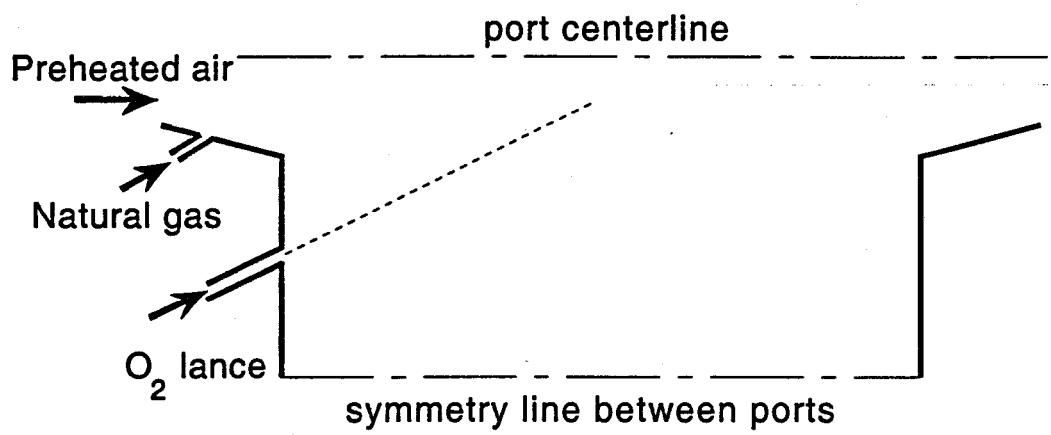

Figure 33. Schematic illustration of the oxygen lance geometry.

3.1.2 Full Furnace Simulations

Air/Fuel Combustion

Numerical simulations of the entire combustion chamber were performed with FLUENT 5. Grid-independent results were achieved with 184,474 cells with clustering in the flame jet regions along the centerline of each portneck. Turbulence intensity for all inlets was assumed to be 10 percent. Hydraulic diameter was 0.022 m for all inlet fuel streams. The hydraulic diameter for each of the six portnecks (air flow channels) is summarized in Table 4.

A convective heat-loss boundary condition was assumed for the walls and crown. Based upon the furnace drawings, the combustor walls were assumed to be 0.46 meters thick and portneck walls were assumed to be 0.38 meters thick. Combustor walls were assumed to have a thermal conductivity of 4.5 W/m-K. The ambient air temperature was assumed to be 300 K, and the external heat transfer coefficient was assumed to be 2 W/m^2-K. The crown was assumed to have the same thickness as the combustor walls, but with a thermal conductivity of 2.5 W/m-K. The molten glass was assumed to have an emissivity of 0.9 and the solid batch was assumed to have an emissivity of 0.6. An HP C360 workstation was used for the model calculation, and converged results were obtained after approximately 600 iterations.

The temperature boundary condition for the glass surface is shown in Figure 34. It was read from an external file. This boundary condition was based on results from a coupled, three-dimensional simulation of the glass tank and batch melting in the same furnace (Hayes *et al.*, 1999). These results previously showed good agreement with experimental data along the centerline of the furnace (Hayes *et al.*, 1999) and were consistent with the observed location of the batch blanket and spring zone. The sensitivity of the predictions to the assumed glass surface temperature boundary condition was investigated by performing two additional simulations wherein the boundary temperature was arbitrarily decreased by 50 and 100 K. Results for all three simulations were shown previously in Figure 21.

The shapes of the predicted centerline heat flux profiles in Figure 21 are similar to the experimental profile. However, the base case predictions are 5-15% higher than measured values except at Location 1. Differences between measurements from the two radiometers were greatest in regions of highest heat flux (Locations 3 and 4) where the circular foil probe data were closer to the base case values. Reducing the glass surface temperature by 50 K lowered the crown flux by about 10 percent. Lowering the glass temperature by 100 K decreased the crown flux by about 20 percent.

Oxy/Fuel Combustion

Oxy/fuel combustion has been applied to smaller scale (container glass, fiberglass, etc.) furnaces with dramatic reductions in NO_x levels, depending on *i)* air in-leakage, *ii)* amount of nitrogen in the fuel, and *iii)* oxygen purity. In this numerical study, two scenarios were investigated: 1) 100% pure oxygen at 105% theoretical O_2 and 2) 90%O_2/10%N_2 at 105% theoretical O_2. Air in-leakage was neglected, and the nitrogen content of the fuel was 6.8%, the same as shown in Table 1. The full-furnace geometry shown schematically in Figure 35 was simulated, assuming symmetry on the

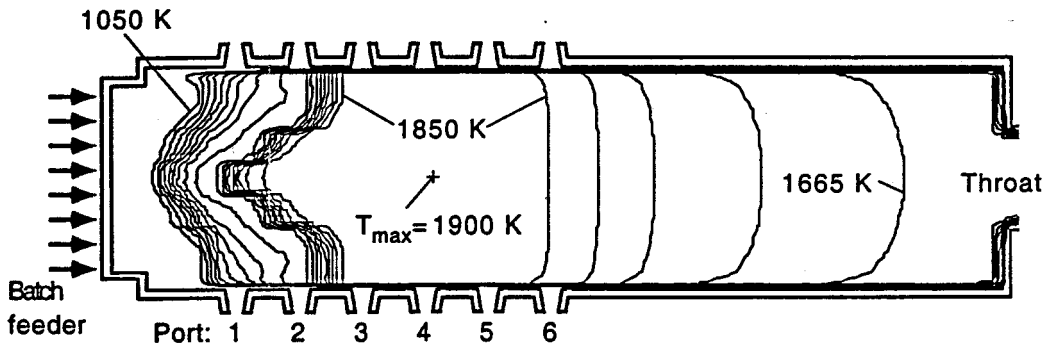

Figure 34. Contour plot of the furnace glass surface temperatures used as a boundary condition in the base case numerical simulation.

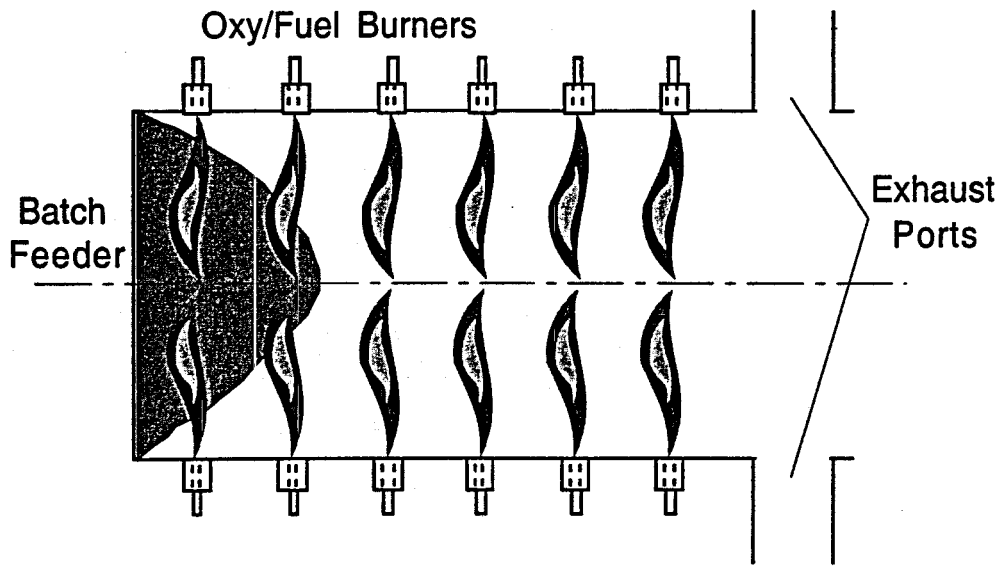

Figure 35. Schematic illustration of oxy/fuel-fired full furnace simulation.

furnace centerline. Six simple burners were configured to fire in-line with identical burners on the opposite wall. Fuel was introduced through a central port in each burner, and the oxygen entered through an annular port surrounding the fuel. Exhaust gases exited through a single exhaust port on each side of the furnace toward the working end.

A FLUENT 4 grid consisting of only 98,000 cells was used for this preliminary, conceptual study. Considerable refinement would have been required to achieve grid-independence, and this would have been impractical to attempt with the workstation that was used for these simulations and was not justified for this conceptual study.

The effect of burning with 100% oxygen firing versus that of burning with preheated air is illustrated by comparing the data shown in Table 7 for these two cases. It is important to note that the simulation for oxygen firing was that for a full furnace whereas the case for the preheated air combustion was a single port module. The NO_x generated per ton of glass for a full furnace was calculated for the port-module simulation assuming that those conditions prevailed in the entire furnace. Although that is certainly not the case and grid resolution is also a concern in the full-furnace simulations, the comparisons provide interesting, qualitative trends, which have been supported by experimental observations in furnaces burning with pure oxygen or oxygen-enriched air. Also, these calculations illustrate the effect of nitrogen, which may be present because of air in-leakage or nitrogen impurity in the oxygen-generation process.

No significant differences were observed in the average exhaust temperatures. The average temperature was only slightly lower for the pure oxygen case. The radiative heat flux to the glass was also slightly lower for that case, although heat flux uniformity did not change appreciably. NO_x concentration in the exhaust increased; however, the amount of NO_x formed was reduced by more than 70%. This is a significant reduction and explains why most glass furnace operators are considering pure-oxygen firing.

It is clear that such an approach also has challenges. First, the amount of water vapor in the exhaust is increased. In general, water accelerates corrosion. The cost of on-site oxygen generation is also significant, but this factor may be offset by the fact that regenerators are not needed. As shown by the simulations, increasing the nitrogen concentration in the oxidizer significantly increases the NO_x generation.

3.2 Coupled Modeling

The uncoupled modeling of the combustion chamber described in the previous section required specification of the thermal boundary condition (e.g., temperature and emissivity) for the batch/glass surface. Of course, batch coverage is not generally known *a priori*, and glass surface temperature distribution is a critical design parameter that one would like to predict for a given furnace design and operating conditions. In this section, individual models for the combustion chamber, glass tank, and batch melting are coupled together to predict the interface boundary condition in an iterative fashion.

3.2.1 Overall Model Methodology

Coupled modeling of the combustion chamber and glass tank in a glass furnace has been reported previously. Carvalho *et al.* (1995c) conducted the first reported study in which an assumed glass surface temperature field was used as a boundary condition for the combustion space, and the calculated heat flux was then used as a boundary condition for the glass tank. The calculated glass surface temperatures were then reintroduced into the first submodel to start the next iteration. Wang (1998), Carvalho *et al.* (1995c) and Wang *et al.* (1998b, 2000a) simulated an end-fired, float glass furnace, and studied the optimization of furnace construction and operation using a fully coupled model. In the previous studies, batch coverage was assumed. The use of a batch-melting model to predict batch coverage is described below.

Combustion Chamber Model

Combustion chamber modeling using the PCGC-3 and FLUENT 4 comprehensive combustion and fluid dynamics codes was described in the previous section. In the coupled modeling described in this section, FLUENT 5 was used. The major difference between FLUENT 4 and FLUENT 5 is the computational grid. The FLUENT 4 code uses a structured grid with body-fitted coordinates, and FLUENT 5 uses an unstructured grid. Unstructured grids are much more flexible for modeling complex geometry, and the use of an unstructured grid in FLUENT 5 facilitated modeling of the burners, portnecks, and curved surface of the crown.

The general procedure for modeling the combustion chamber with FLUENT 5 was as follows: An unstructured grid for the geometry of interest was first created using GAMBIT, a commercial grid generation package. Symmetry was used, where applicable, to reduce the size of the problem. Triangular face meshes were used for all faces except the bottom (glass surface) face, where a quadrilateral mesh was used to facilitate interfacing with the glass tank model. Thus the grid was tetrahedral except for a layer of pyramids on the bottom face. After importing the grid into FLUENT 5, smoothing and face swapping were performed until no further improvement in skewness was obtained.

The segregated, implicit solver in FLUENT 5 was used with the k-ε model and standard wall functions (Launder and Spalding, 1972; Rodi, 1984) for turbulence, second-order upwind differencing was used for discretization, and the SIMPLE algorithm was used for pressure-velocity coupling (Patankar, 1980). The assumed-shape probability density function (PDF) method (Hill and Smoot, 1993) was used for chemistry and turbulence interactions. A beta function represented the PDF of the fuel mixture fraction, and transport equations were solved for mixture fraction mean and variance. The mixture fraction is the local mass fraction of the mixture that came from the fuel stream. Hence, it represents the degree of mixing between fuel and oxidizer. The fuel composition was shown in Table 1. The mixture of fuel and oxidizer in the furnace was assumed to be at local instantaneous equilibrium (infinite-rate chemistry) with the following fifteen species: CH_4, C_2H_6, C_3H_8, C_4H_{10}, C_5H_{12}, C_6H_{14}, CO, CO_2, H_2, H_2O, O_2, N_2, H, OH, and O. Instantaneous and time-averaged compositions were pre calculated and tabulated as functions of the mixture fraction and its variance so that table lookup could be used during the actual simulations to speed up the calculations.

Radiation was calculated using the discrete ordinates method (Chui and Raithby, 1993; Raithby and Chui, 1990), with the weighted-sum-of-gray-gases (WSGGM) model for the variable absorption

coefficient. A two-step model (Tesner *et al.*, 1971; Magnussen and Hjertager, 1976) was used for soot generation and oxidation. Transport equations were solved for the nuclei and soot concentrations. Thermal and prompt NO concentrations were calculated using a transport equation with kinetic formation and destruction rates, neglecting the effect of these reactions on the velocity and temperature fields (Fluent, 1998; Webb *et al.*, 1998).

Inlet flow conditions for the fuel ports were specified with a mass flowrate and direction cosines for the firing angle. Inlet turbulence conditions were specified with hydraulic diameter and an assumed turbulence intensity of ten percent. Unless otherwise indicated, the emissivity of the furnace walls and crown was assumed to be 0.6, and heat loss through the combustor walls and crown was calculated assuming an arbitrary wall thickness and ambient heat transfer coefficient which would yield a reasonable heat loss rate (e.g., 2000 W/m^2) with an ambient temperature of 300 K. The thermal boundary condition for the bottom (glass) surface was supplied in an external (profile) file. Batch and glass emissivities were assumed to be 0.6 and 0.9, respectively.

A tutorial for the combustion chamber model illustrating the grid generation in GAMBIT, importing into FLUENT 5, and the solution, has been written and distributed to model users.

Glass Tank Model

The glass tank was modeled with FLUENT 4, using a structured grid, or with FLUENT 5, using an unstructured grid. A heat flux boundary condition was required for the top (free) surface, which receives heat from the combustion space. This boundary condition was supplied in an external (profile) file.

The main assumptions for the simulation of heat transfer and the convection flows in the glass melting model were: (1) the molten glass was assumed to be a homogeneous, incompressible, Newtonian viscous fluid; (2) bubbles and chemical reactions were neglected; (3) the flow and heat transfer of the molten glass in the tank were at steady-state; and (4) the radiation heat transfer inside the glass melt was treated by using an effective thermal conductivity in the energy equation (Wang, 1998). The partial differential equations governing mass continuity, transport of momentum, and energy were solved. Details can be found elsewhere (Wang, 1998; Carvalho *et al.*, 1995c, 1997a; Wang *et al.*, 1998b, 1999a 2000a, 2000b; Hayes *et al.*, 1999).

The thermal conductivities of the tank bottom and other tank walls were 0.7 and 2.0 W/m-K, respectively. The heat loss from the glass surface in the conditioning section was specified arbitrarily to be negligible. While heat losses exist in the conditioning section, they exercise only minor influence on the batch melting and hence, a simplified adiabatic condition was imposed.
It was initially assumed that the batch coverage area on the glass surface was fixed according to experimental observations (McQuay and Webb, 1996) and that the batch-melting rate was uniform. Later, a batch-melting model was included in the coupling procedure for predicting the batch location.

The grid was generated in Gambit and imported into FLUENT 5 which was used as the platform for solution of melt flow in the tank.

Batch Melting Model

The conversion of batch into molten glass is a complex process that includes fluid flow, heat and mass transfer, chemical reaction with gas evolution, and phase change. It was assumed in the model that the chemical reactions take place at a specified temperature, 1123 K, consuming heat and producing gas that escapes from the top surface of the batch. It was also assumed that the melting mass loss factor (fraction of raw materials evolved as gas) is constant for a given batch composition. The melting mass loss factor was assumed to be 20%. The batch was assumed to change phase over a temperature range by modeling the temperature dependency of viscosity. Above 1473 K, the melting process was assumed to be complete (Hammel, 1986). The glass reaction and melting temperatures are for Na-Ca-Si glasses of the type produced in the float glass furnace simulated here. The melted batch provides a mass input to the glass melt zone where the magnitude of the mass locally introduced from the batch zone to the melt zone depends on the local batch-melting rate. The local thickness of the batch is a function of temperature, density, and the fraction of unmelted batch.

The quasi-three-dimensional model, consisting of a series of unconnected, two-dimensional 'lanes' extending from the doghouse, is shown in Figure 36. Inlet conditions were prescribed for initial thickness, velocity, and temperature.

Batch inlet velocities were calculated from the pull rate of the furnace and the variation in batch feed along the width of the tank, based on observation.

The heat flux from the molten glass to the bottom surface of batch blanket, $Q_{gl\text{-}b}$, was calculated by

$$Q_{gl-b} = \left(k\frac{\partial T}{\partial y}\right)_{gl,interface} = \left(k\frac{\partial T}{\partial y}\right)_{b,interface} . \tag{6}$$

Here, k is the thermal conductivity, T is the temperature, y is the coordinate direction normal to the batch/melt interface, and the subscripts "gl" and "b" denote glass and batch quantities, respectively. The net heat flux from the combustion space to the top surface of the batch blanket or the free surface of glass melt, $Q_{f\text{-}gl/b}$, can be calculated by the combustion chamber model as follows:

$$Q_{f-gl/b} = \left(k\frac{\partial T}{\partial y}\right)_{gl/b,surface} = G_{gl/b} - J_{gl/b} + q''_{conv} \tag{7}$$

In this equation, $G_{gl/b}$ is the incident radiant energy (irradiation) from the combustion chamber, $J_{gl/b}$ is the local radiosity (combined emission and reflection) leaving the molten glass or batch, and q''_{conv} is the local convective heat flux from the flame to the glass/batch surface. These quantities were predicted as part of the combustion chamber simulation.

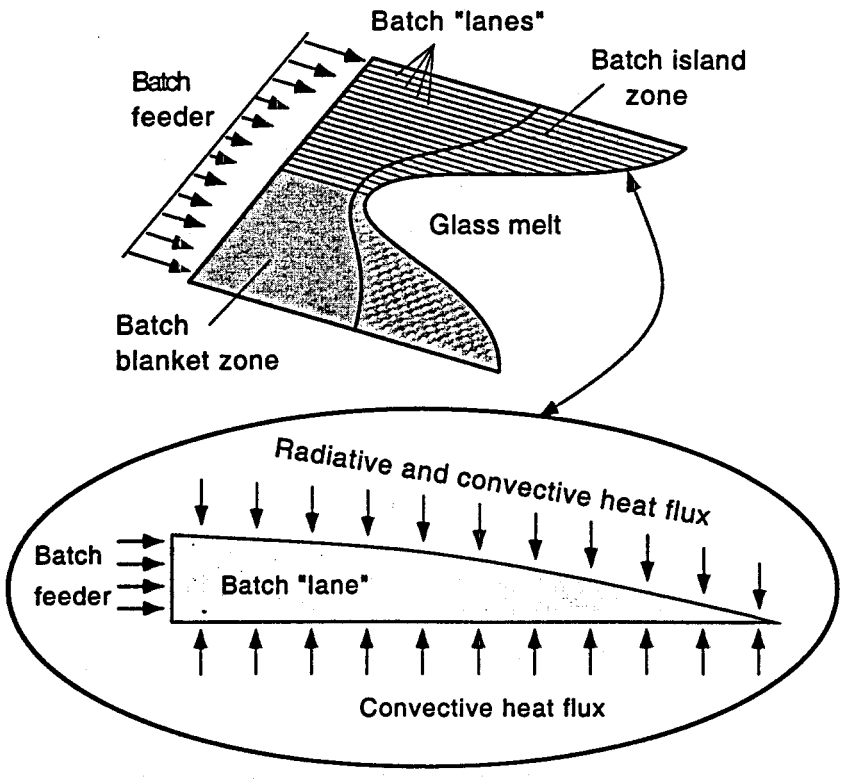

Figure 36. Schematic illustration of the batch-melting model.

The temperature field, the shape of the batch, the batch coverage area, local thickness, and the melting rate were predicted by the batch melting model (Wang, 1998). Batch melting in both cross-fired and end-fired furnaces can be predicted with the model (Wang, 1998; Carvalho *et al.*, 1995c, 1997a; Wang *et al.*, 1998b, 1999a, 2000b; Wang *et al.*, 1999b).

The set-up and use of the batch-melting model without coupling has been described in a tutorial which has been distributed to model users.

Glass Tank With Batch Melting

The batch melting and flow and heat transfer in the glass tank were simulated using the glass tank model coupled with the batch melting model. The two models communicated with each other in an iterative fashion. The tank model provided the thermal boundary condition for the bottom surface of the batch blanket, and the batch melting model provided the boundary condition for mass addition due to melting from the batch blanket to the glass. Additional details regarding the coupling procedure are given in the next section and in Wang *et al.* (1999a).

Most of the furnace operating conditions have been described previously. The batch consisted of 65% (by weight) raw materials and 35% cullet. The batch inlet temperature was 303 K and the initial thickness was 0.2 m. The thermal conductivity of the tank refractory walls and bottom were 2.0 and 0.7 W/m-K, respectively. The thermal boundary condition for heat transfer from combustion chamber is shown in Figure 37. The sensitivity of the results to the imposed heat flux was investigated by scaling the incident radiant heat flux profile in Figure 37 by ±10%. The computational grid was 195,000 cells (156 x 50 x 25) for the tank model and 264,000 cells (150 x 44 x 40) for the batch model. Converged results were obtained on an HP 735 workstation after approximately 8000 iterations. Two different cases were considered, with and without bubblers. Bubblers were used during the period when the experimental measurements were made. The bubbler submodel was based on furnace operating data and was incorporated into the simulation using a FLUENT 4 user subroutine. Details are given in Wang (1998).

Although significant differences were apparent in the model results with and without bubblers, the effect on glass surface temperature along the furnace centerline was small. The effects were much more significant in the lower regions of the glass tank near the bubblers.

The numerical results assumed steady flow and heat transfer and were compared with time-averaged experimental data. The predictions agreed well with both the trend and magnitudes of the measured average surface temperatures along the centerline of the furnace. The difference between predicted and measured values was less than 45 K in each instance, with an average difference of less than 20 K. The largest differences occurred in the regions of highest temperature: Locations 4 and 5. Increasing (or reducing) the imposed radiant heat flux profile of Figure 37 by 10% (without bubblers) increased (or reduced) the glass surface temperatures approximately 40 K. The shape of the profile was unaffected.

The model also predicted two buoyancy-driven, three-dimensional recirculation patterns in the tank. One was in the region between the spring zone and the batch feeder, while the other was between the working end and the spring zone. Figure 38 shows the predicted velocity vectors on the center plane. The magnified view of the predicted melt velocities near the spring zone, between ports 4

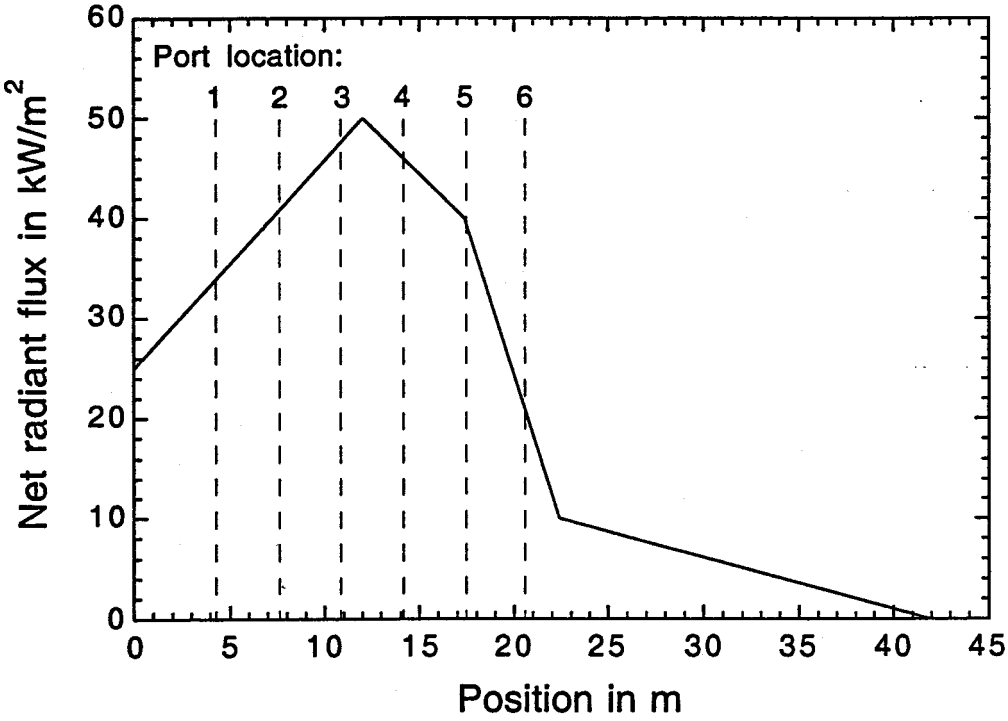

Figure 37. Axial profile of net heat flux on the batch/glass surface imposed as boundary conditions in the numerical simulations.

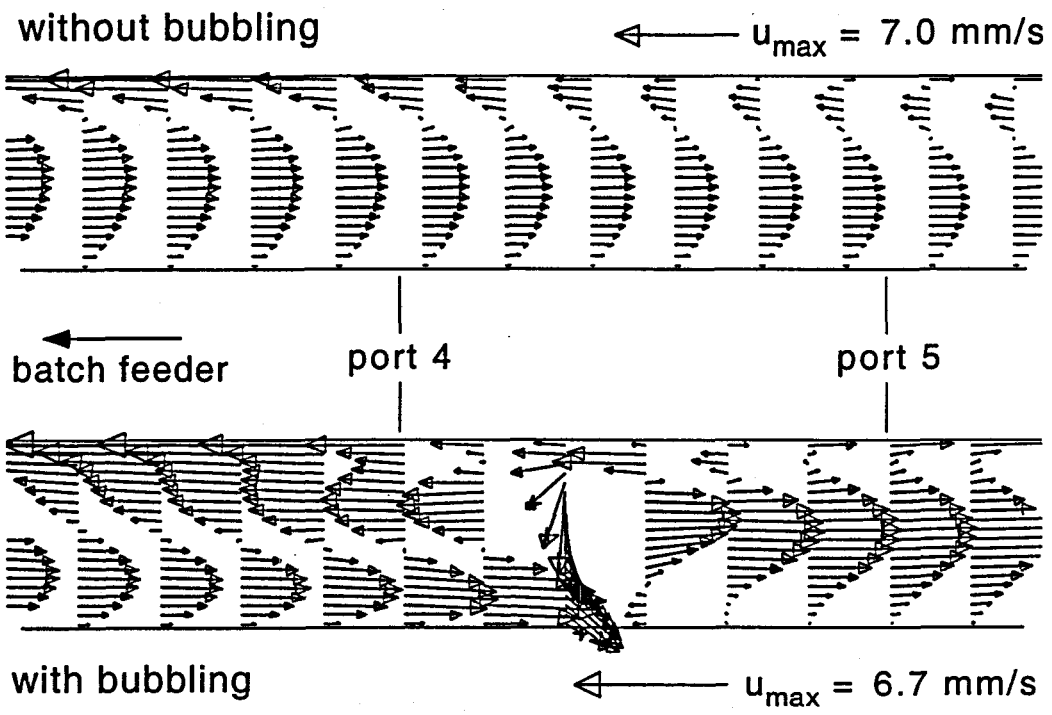

Figure 38. Velocity vector plots from the glass tank numerical model with and without bubblers in a vertical plane in the tank along the furnace axial centerline.

and 5, is shown. Although the simulations were performed for the entire glass tank, only the region near the spring zone is shown in Figure 38 because of the importance of its effect on the measured surface temperatures. The position of these plots with respect to physical characteristics of the furnace is also included in this figure for clarity.

The molten glass between the batch feeder and Location 1 was shielded from radiant combustion heat by the blanket of unmelted batch. This, combined with heat loss due to the proximity of the cooler batch and furnace walls, contributed to the lowering of the molten glass temperature in the region. The cooler molten glass was denser and fell toward the bottom of the tank nearest the batch-side tank wall, creating this three-dimensional, recirculation zone. As shown in Figure 38, the flow pattern of the molten glass indicates that the higher-density glass near the bottom of the tank traveled toward the center of the glass tank, rising to the surface at the location of the spring zone. The spring-zone region is characterized by high combustion firing rates, with minimal heat absorption by batch material. It was in this general area that the highest glass surface temperatures were measured. At the glass surface upstream of the spring zone, glass flowed back toward the batch feed area. Downstream of the spring zone, glass flowed toward the furnace working end. The recirculation and glass flow patterns are important in understanding the analysis of the glass surface temperature data as well as the overall melting process in the furnace. Figure 38 also illustrates the effect of the bubblers on the flow in the glass tank, clearly showing the enhancement of the mixing process resulting from the presence of the bubblers.

The complex three-dimensional recirculation pattern in the melt between the batch feeder and the spring zone region can also be seen from the glass surface velocity vectors shown in Figure 39. The locations of ports 1-5 are also shown for reference. The surface velocity vectors shown for the two operating conditions reveal both the predicted spring zone location where the surface flow velocities divided in opposite directions, and the predicted surface location of the batch blanket where the velocity magnitudes are significantly smaller than those on the molten glass surface. The region of large changes in surface velocity magnitudes outlines the predicted boundary between the molten glass and batch, where the high reverse surface velocities are rapidly decelerated. The location of the spring zone is shown in the figure to be approximately two-thirds of the way down the melting section, where the rising melt separates at the surface in the region between Locations 4 and 5. The differences in surface velocities between the two cases appear to be relatively minor, with the simulation without bubblers exhibiting less variation in surface velocity laterally across the furnace for a given axial location. The bubblers result in a more curved surface velocity profile near the spring zone, with higher velocities near the furnace axial centerline and lower velocities angled away from the centerline in regions closest to the tank sides.

Glass Tank and Combustion Chamber With Batch Melting

In a previous section, the combustion space of the furnace was simulated with a full-furnace model. This model required, as input, the thermal condition (*e.g.* temperature and emissivity) of the batch/glass surface. In this section, the combustion space and glass tank are simulated in integrated fashion. A model for the glass tank is presented and used to predict the thermal boundary condition required by the combustion chamber model. The glass tank model requires, as input, the heat flux from the combustion chamber. Hence, the two models are coupled, and a coupling procedure is described for solving them simultaneously, thus avoiding the need to fix the

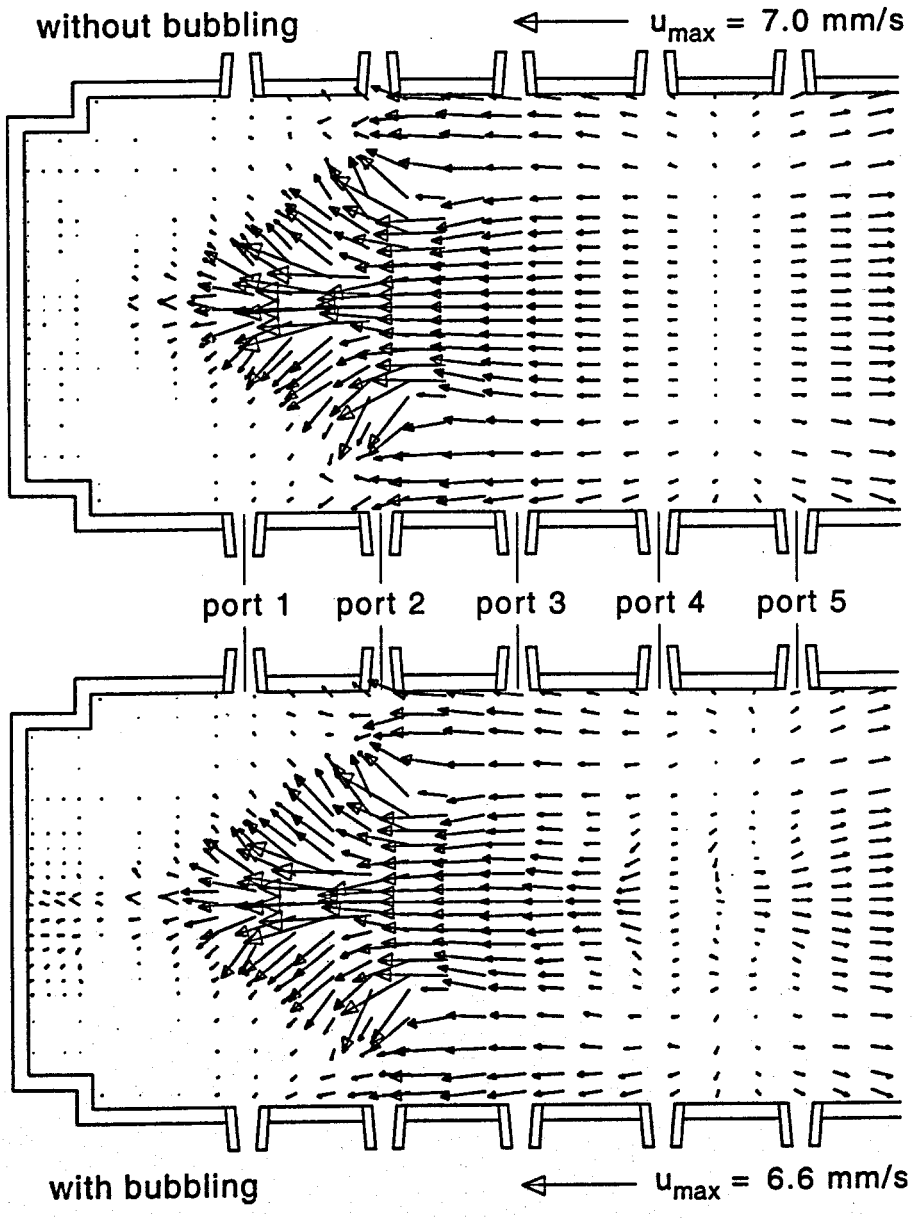

Figure 39. Surface velocity vector plots from the glass tank numerical model with and without bubblers.

glass/batch surface heat flux and temperature as boundary conditions. These interface conditions are calculated iteratively by the coupling procedure. Results are first presented for an oxy/fuel-fired furnace, where batch coverage and melting rate were assumed. Results are then presented for an air-fired furnace, in which a batch-melting model, also described in this section, is coupled with the combustion chamber and glass tank models and used to predict the batch coverage and melting rate. The information flow for the coupled modeling procedure is diagrammed in Figure 40. Information was transferred in both directions between each pair of models as shown. The combustion chamber model provided the heat flux to the batch and glass surfaces. The glass tank model provided the glass surface temperature seen by the combustion chamber and the heat transfer rate from the molten glass to the underside of the batch. The batch-melting model provided the batch coverage (location) and batch surface temperatures.

The three models were run simultaneously. The FLUENT 5 processes (combustion chamber and glass tank simulations) were run on separate, dedicated workstations. The batch-melting model is not as computationally expensive as the other two models, and it was typically run on the same workstation as the glass tank model.

Before coupling the models, they were typically run as stand-alone models for a specified number of iterations to establish reasonable solutions with assumed boundary conditions. Details of this procedure are given in the model coupling tutorial, written for potential model users.

FLUENT 5 profile files were used to transfer information between the three models. Very strong under-relaxation was used to promote stability. Typical under-relaxation factors were of the order of 0.05.

After coupling the combustion space, batch, and tank submodels, the three models were allowed to run simultaneously until convergence was achieved. For the FLUENT processes, convergence was monitored by watching the residuals, the energy balance, and key parameters such as exhaust temperature and heat flux to the tank (for the combustion chamber), and average glass surface temperature and throat (outlet) temperature (for the glass tank). Convergence was achieved when a stochastic steady state was reached.

Air/Fuel Fired

In this section, a coupled simulation of the combustion chamber, glass tank and batch melting process for the air/fuel-fired furnace shown previously in Figure 1 is described. The operating conditions of this furnace as well as detailed measurements made through access ports drilled in the crown prior to furnace rebuild were described previously (McQuay *et al.*, 1996, 2000; Newbold *et al.*, 1997). Glass surface temperature and incident heat flux on the crown were also reported (Hayes, 1999).

Because of computer memory limitations, only the melting section was simulated in the combustion chamber model. The heat transfer to the glass surface in the conditioning section of the combustion chamber from neck to outlet was assumed to be negligible. The heat losses through the crown and walls were assumed to be 2.6 and 7 kW/m^2, respectively. The thermal conductivities of the tank

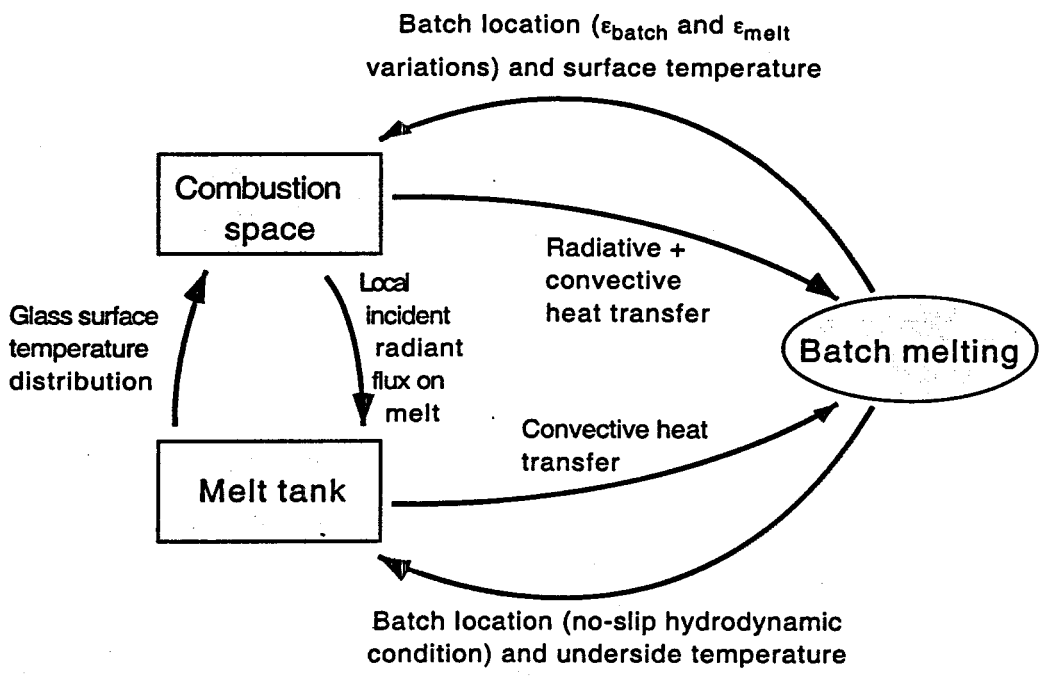

Figure 40. Information flow for the coupled solution.

bottom and other tank refractory walls were assumed to be 0.7 and 2.0 W/m-K, respectively. The model also included the thermal effects of a water cooler located at the tank neck used for melt cooling.

An unstructured grid consisting of 120,000 cells was used in FLUENT 5.0 for the combustion chamber model, and a structured grid consisting of 195,000 cells was used in FLUENT 4.4 for the tank model. The batch model used a grid comprised of 194,000 nodes. Converged results were obtained after approximately 1000 iterations.

Predicted glass surface temperature is shown in Figure 41. The solid line shown in the figure crossing the melt surface is the initial guess for the batch boundary location.

Glass surface temperature is an essential property in determining glass flow pattern, batch melting, glass homogenization, and fining, all of which determine the glass quality. Batch coverage on the melt surface can be clearly seen from Figure 41 by the relatively low temperature. Furthermore, a slight asymmetry in the glass surface temperature due to firing from one side of the furnace to the other is also evident. The maximum temperature occurred approximately two-thirds of the way from the batch feeder to the throat, consistent with the estimated location of the spring zone.

The predicted and measured incident radiant flux profile along the furnace centerline is shown in Figure 42. The predicted incident heat flux distribution is a critical furnace design variable. Although the shape of the profile is predicted well, including the point of maximum flux, the magnitude is over predicted. However, these simulations did not include the effects of batch islands or foam, both of which would lower the heat flux.

Two complex, buoyancy-driven, three-dimensional recirculation patterns were predicted in the glass tank. One was in the region between the batch feeder and the spring zone; the other was between the spring zone and working end. Figure 43 shows the predicted velocity vectors on the glass surface. The figure clearly illustrates the location of the spring zone where melt rising from the bottom of the tank reaches the free surface and splits, flowing in opposite directions back toward the batch blanket and toward the working end. This spring zone is located between ports 4 and 5. Predicted maximum surface velocities occur near the batch. At this point, the flow falls to the floor of the tank due to the cooling which occurs as energy is supplied from the melt to the underside of the batch blanket. Note that the extent of the batch blanket is a minimum near the center of the tank, with longer extension along the sides of the furnace.

Figure 44 shows the predicted profiles of crown and glass surface temperature along the furnace centerline. The figure also includes measured data. The predicted glass/batch surface temperature agrees well with the measurements, with maximum deviations of 30-35 K downstream of the batch (ports 2-6). Predictions for the crown temperature are consistently low by approximately 100 K. The thermocouple holes on the crown were blind holes, and the refractory blocks used a thermocouple well that featured a 3-cm refractory tip separating the thermocouple bead from the combustion space. Crown surface temperature is estimated to be 50-80 K higher than reported here.

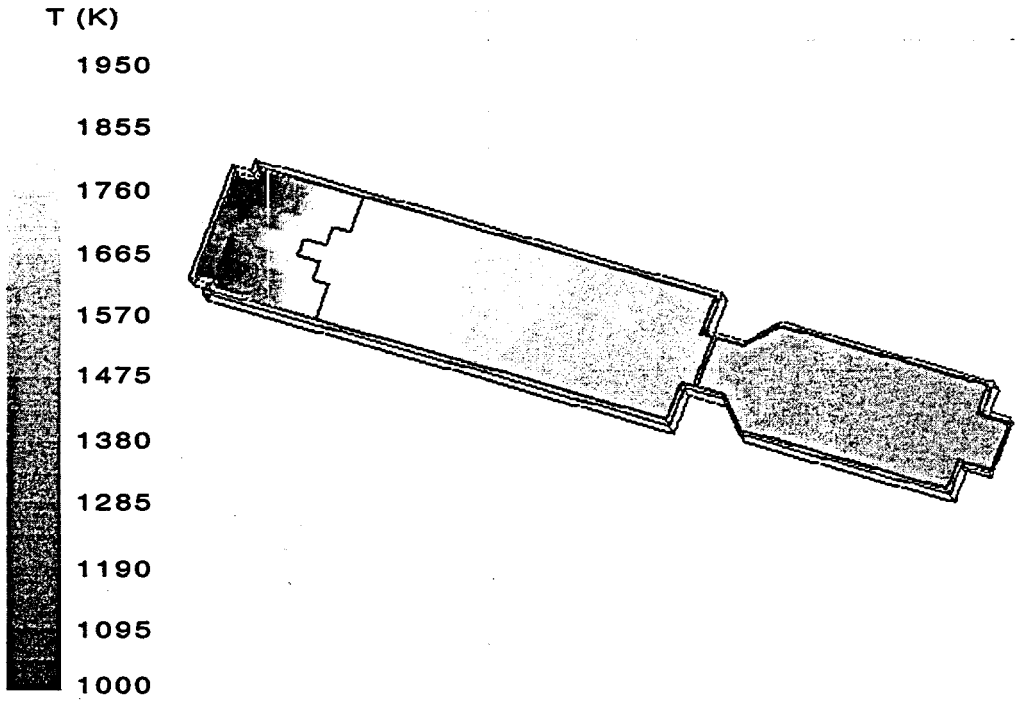

Figure 41. Predicted glass surface temperature distribution.

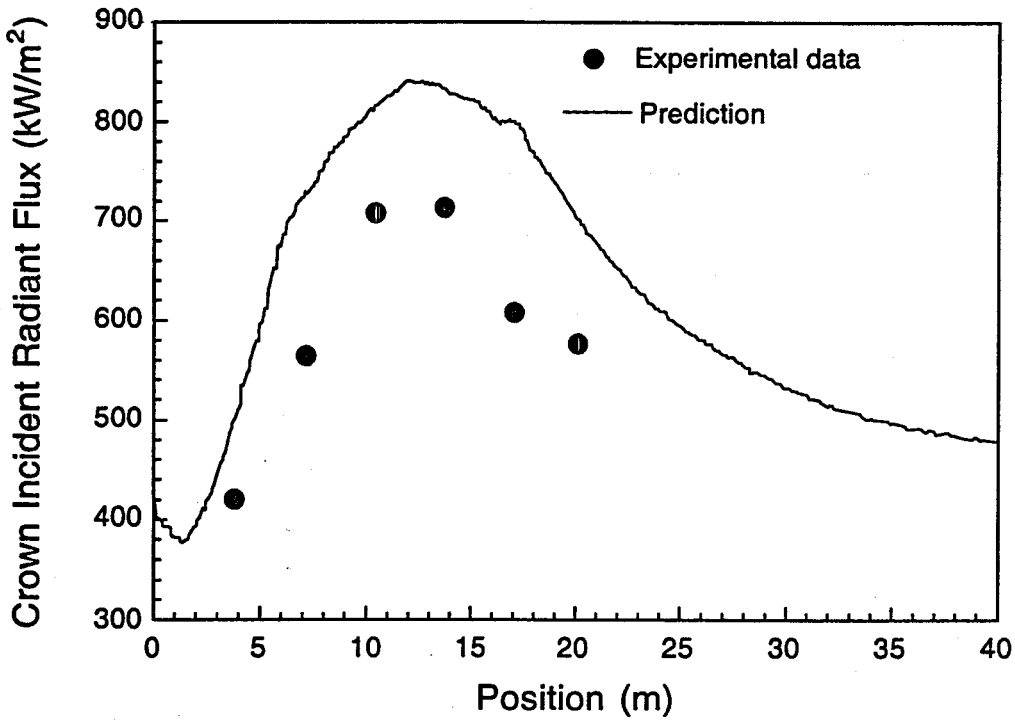

Figure 42. Predicted and measured incident radiative heat flux on the crown.

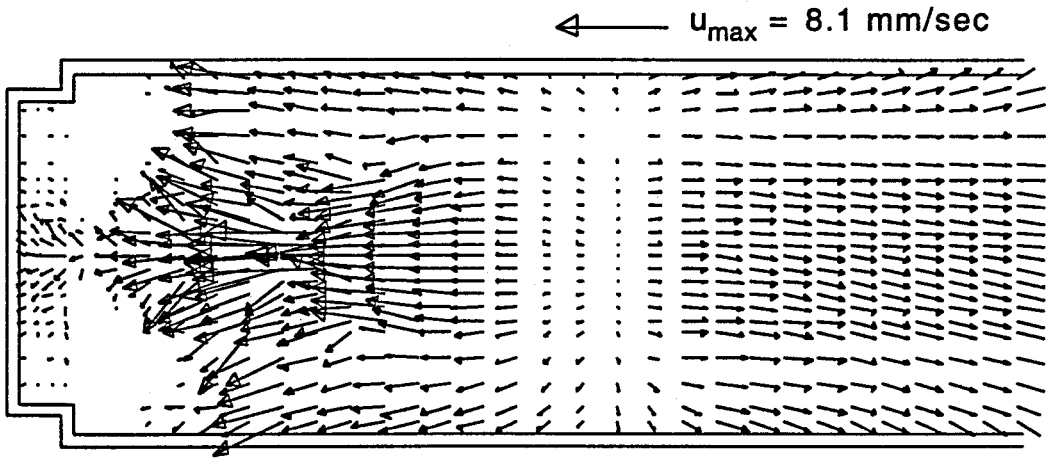

Figure 43. Predicted glass surface velocity distribution.

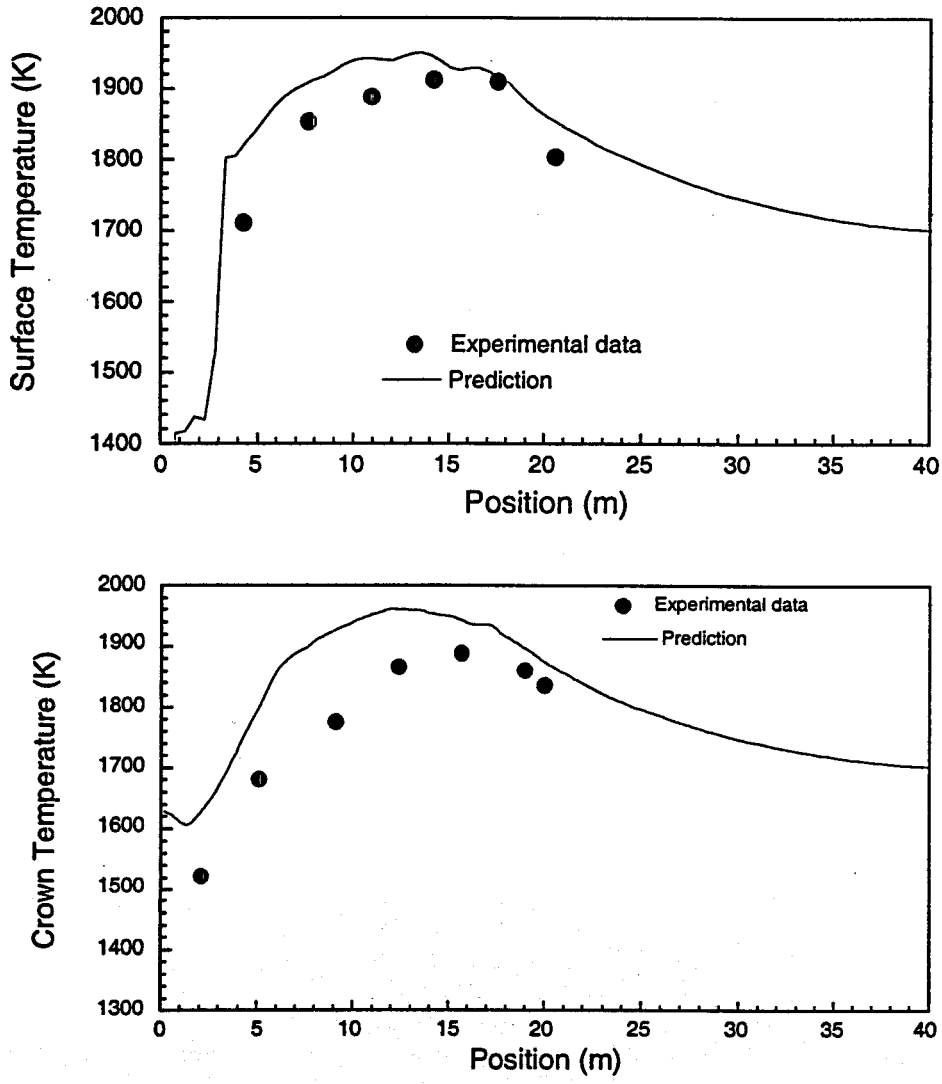

Figure 44. Predicted and measured profiles of glass/batch surface temperature and crown temperature along the furnace centerline.

The predicted and measured exhaust gas compositions are given in Table 8. The data and predictions are in good agreement, with the exception of the CO_2. Significant CO_2 is generated in the batch melting and fining process, particularly at early ports where more significant melting occurs. It is estimated that over 2000 kg/hr of CO_2 is generated in the melting process in this furnace (McQuay *et al.*, 2000).

Oxy/Fuel Fired

Oxy/fuel combustion in a hypothetical float glass furnace is simulated. Oxy/fuel combustion saves energy and reduces combustion-generated pollutants. Oxy/fuel combustion has been successfully used for small and medium-sized industrial glass-melting furnaces.

The hypothetical geometry was based on the previously described air-fired, float glass furnace. The six portnecks located on each side of the combustion chamber were replaced by six oxy/fuel burners and arranged symmetrically along the furnace length. The burners were 0.415 m above the glass surface and spaced at 3.3-m intervals starting at 3.7 m from the doghouse. A 0.68 m^2 outlet opening for exhaust gas was located on each side on the breast wall near the doghouse. The model also included the thermal effects of a water cooler located at the tank neck for melt cooling.

The pull rate of the furnace was the same as the air/fuel furnace. Because oxy/fuel combustion does not require regenerators, there was no oxygen preheating, and both oxygen and natural gas inlet temperatures were 300 K. Inlet flowrates for four parametric cases are shown in Table 9. The firing distribution among the burners was 17.3, 20.4, 20.8, 15.1, 14.4 and 12.0% of the total on each side, starting from the doghouse end. Because there were no regenerators, there were no reversals in firing direction, and burners on both sides of the furnace operated continuously. Because of computer memory limitations, only the first half of the melting section was simulated in the combustion chamber model, and the results were used to provide the thermal boundary condition to the first half of the tank model. In the second half of the tank model, the heat flux to the top surface was assumed to be uniform at 10 kW/m^2. Beginning at the neck and continuing to the end of furnace, the heat flux was assumed to be negligible.

External heat loss was assumed to be 2.5 and 3.5 kW/m^2 through the crown and walls, respectively. The batch coverage was specified, based on video observations in the air/fuel-fired furnace (Hayes *et al.*, 1999). The batch-melting rate was assumed to be uniform. The top and bottom batch surface temperatures were assumed to be piecewise linear varying from 1373 K at the doghouse to 1573 K or higher at the edge of the blanket. The thermal conductivities of the tank bottom and other tank walls were 0.7 and 2.0 W/m-K, respectively. Conjugate heat transfer in the melt tank walls was included in the analysis (Wang, 1998).

Only half of the combustion chamber was simulated because of symmetry about the centerline. The full glass tank was simulated, however, even though it was symmetrical, because the savings did not justify the work that would have been required to modify the coupling procedure to account for symmetry. The computational grids were 98,301 cells (151 x 21 x 31) for the combustion chamber and 195,000 cells (156 x 50 x 25) for the glass tank. Converged results were obtained on two HP C360 workstations after 6000-8000 iterations.

Table 8. Predicted and measured exhaust compositions.

		Port 1	Port 2	Port 3	Port 4	Port 5	Port 6
O_2 (vol%)	Calculated:	1.8	3.0	2.6	2.2	5.8	8.2
	Measured:	2.3	2.4	1.7	1.3	6.3	9.0
CO_2 (vol%)	Calculated:	10.2	10.2	10.4	10.5	8.6	7.2
	Measured:	17.0	15.4	14.6	11.2	8.2	6.5

Table 9. Inlet natural gas and oxygen flowrates.

Firing, $F_i/F_{100\%}$	Natural Gas	Oxygen	Total Mass F_i
100% firing	**1771**	**6520**	**8291**
116% firing	2052	7591	9643
133% firing	2363	8731	11094
84% firing	1478	5445	6923

The predicted gas temperature and turbulent flow profiles for the 100% firing case are shown in Figures 45 to 49. Because of the effective mixing of the natural gas and oxygen around the burner orifice, the oxy/fuel flame temperature was 473 K higher than the air/fuel flame temperature reported previously (Wang *et al.*, 1998). The near-burner gas velocity was also higher. The flame flows over the batch/glass melt surface, which enhances the heat transfer from the flame to the batch and melt. In the regenerative, crossfire, air/fuel furnace, high temperature exhaust gas flows out of the combustion chamber through the outlet portnecks that are located directly across from the inlet portnecks. Therefore, the flame path is shorter in the air-fired furnace, and the energy lost in the exhaust gas is higher. In the oxy/fuel furnace, there was one exhaust outlet located at the end of each breast wall near the doghouse. Before flowing out of the combustion space through the outlet, the exhaust gas traversed a longer distance inside the combustion chamber. The increased residence time for combustion gases in the oxy/fuel configuration resulted in increased heat transfer to the glass tank, decreased exhaust temperature, and increased thermal efficiency, as compared with the air-fired furnace. The experimentally measured average exhaust gas temperature at outlet openings in the air/fuel furnace was 1758 K (Newbold *et al.*, 1997). The predicted average exhaust temperature in the oxy/fuel furnace was 1618 K. The composition of the exhaust gas was also very different in the two furnaces. The H_2O and CO_2 concentrations were considerably higher in the oxy/fuel furnace, as shown below in Table 10.

In the superstructure of the air/fuel-fired furnace, there are high gas velocities. High flow velocities in close contact with batch give rise to dust in the area between the doghouse and the locations where the first major batch melting reactions take place. Alkali dust can volatilize partly or completely at the high temperature in the combustion space. Reactions between the alkali gases and the superstructure refractory are detrimental and may lead to refractory erosion and the formation of slag that flows into the bath of molten glass, causing defects. As the total fuel and oxygen mass flowrates in oxy/fuel combustion than in air/fuel combustion, the gas velocities in the combustion space are lower. Figure 46 shows velocity magnitudes through most of the furnace were in the 10 m/s range, whereas they were 20-25 m/s in the air/fuel furnace (Newbold *et al.*, 1997). It is expected that lower velocities in the combustion space may contribute to lower refractory corrosion, although the corrosion mechanism also depends on NaOH concentration, alkali volatile deposition rates, etc.

The predicted heat flux to the glass and batch surfaces is shown in Figure 47. Total radiation heat transfer from the combustion space to the batch blanket and to the glass surface is summarized in Tables 11 and 12.

Figure 48 shows the NO_x distribution at one horizontal plane through the burner centerline in the combustion chamber. Oxy/fuel combustion may reduce furnace pollutant emissions significantly. In the four cases simulated here, the furnace NO_x emissions are in the range of 1.311 to 2.585 kg NO_x/ton glass and the furnace NO_x emission for 100% firing is only 1.933 kg NO_x/ton glass (see Table 13), which is much lower than the air/fuel case (5.5 kg NO_x /ton glass) (Webb *et al.*, 1998).

Predicted glass surface temperature is shown in Figure 49. The split batch boundary is indicated with a solid line. The glass temperature is an essential property in determining the glass flow pattern, batch melting, glass homogenization, and fining, all of which determine the glass quality. Since there is no flame reversal, the oxy/fuel furnace is more stable than the air/fuel furnace.

Table 10. Predicted mass percentages of exhaust gas at outlet openings.

Firing, $F_i/F_{100\%}$	O_2 (%)	N_2 (%)	CO_2 (%)	H_2O (%)	Total
100% firing	**4.0**	**2.3**	**52.6**	**41.1**	**100.0**
116% firing	4.4	2.3	52.4	40.9	100.0
133% firing	4.2	2.3	52.5	41.0	100.0
84% firing	4.0	2.3	52.6	41.1	100.0

Table 11. Predicted average heat flux and total heat transfer from combustion space to batch blanket.

Firing, $F_i/F_{100\%}$	Flux q_i (kW/m^2)	Total Q_i (kW)	$Q_i/Q_{100\%}$
100% firing	**99**	**9555**	**100%**
116% firing	117	11261	118%
133% firing	136	13082	137%
84% firing	79	7663	80%

Table 12. Predicted average heat flux and total heat transfer from combustion space to glass melt surface.

Firing, $F_i/F_{100\%}$	Flux q_i (kW/m^2)	Total Q_i (kW)	$Q_i/Q_{100\%}$
100% firing	**25**	**3521**	**100%**
116% firing	31	4273	121%
133% firing	37	5193	148%
84% firing	20	2777	79%

Table 13. Predicted exhaust gas variables.

Firing, $F_i/F_{100\%}$	T_{out} (°C)	V_{out} (m/s)	NO_x (ppm)	Total NO_x (kg/ton glass)
100% firing	**1345**	**5.88**	**3990**	**1.933**
116% firing	1368	6.95	4066	2.281
133% firing	1388	8.10	4002	2.585
84% firing	1323	4.83	3307	1.311

T_{out} : Average exhaust temperature

V_{out} : Average exhaust gas velocity

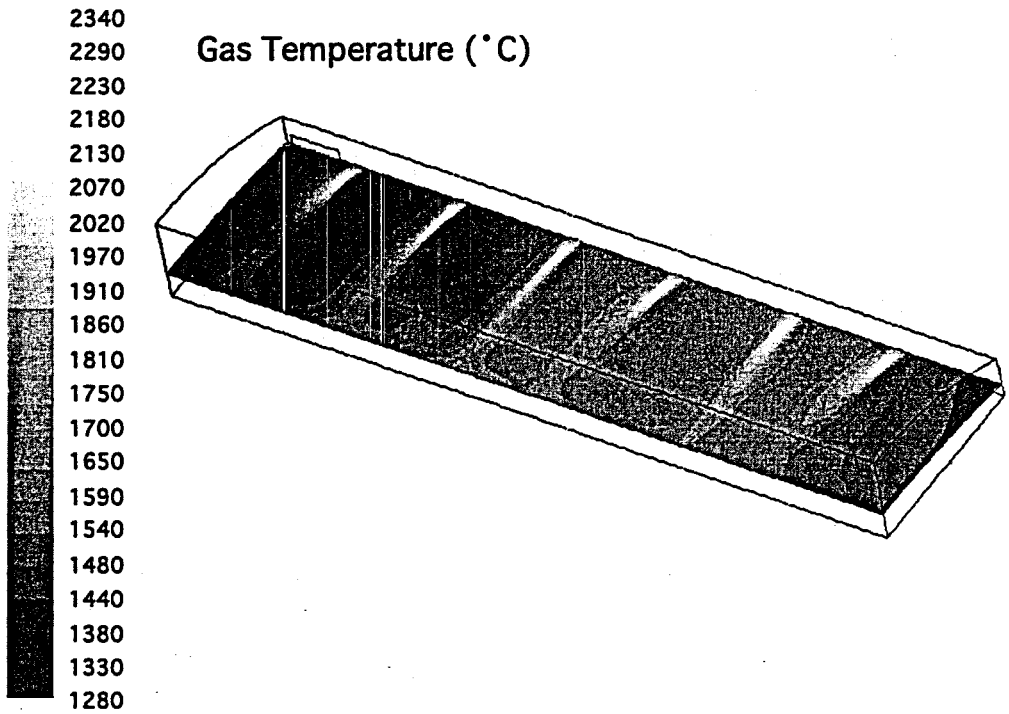

Figure 45. Predicted gas temperature profile in the combustion chamber (100% firing).

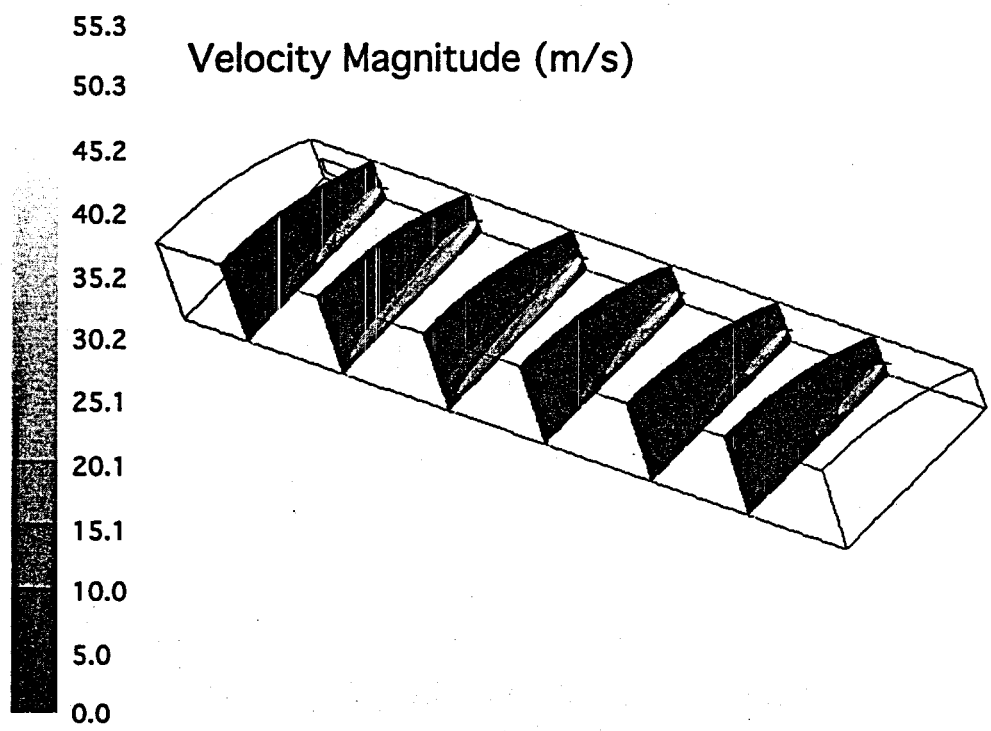

Figure 46. Predicted gas velocity profiles in the combustion chamber (100% firing).

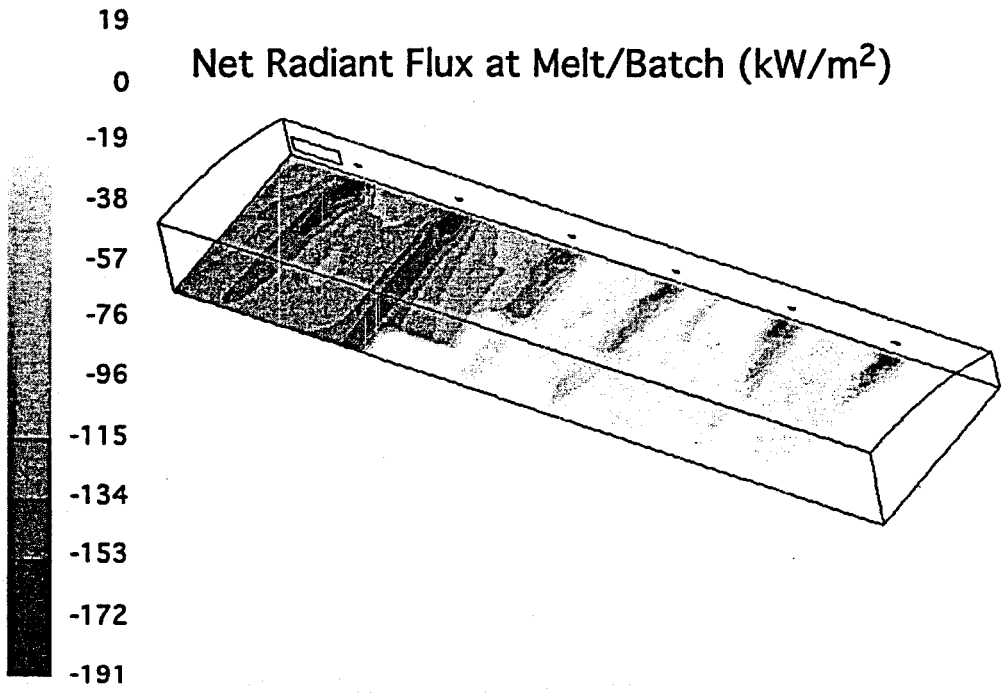

Figure 47. Predicted heat flux distribution from the combustion space to the surface of batch and glass melt (100% firing).

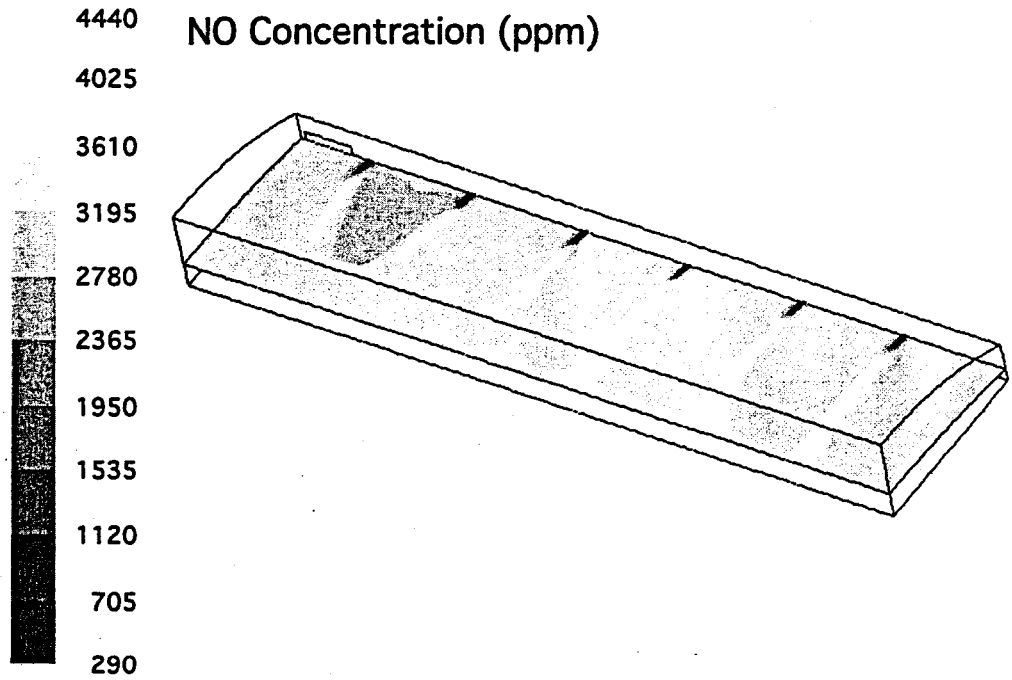

Figure 48. Predicted NO_x distribution in the combustion chamber (100% firing).

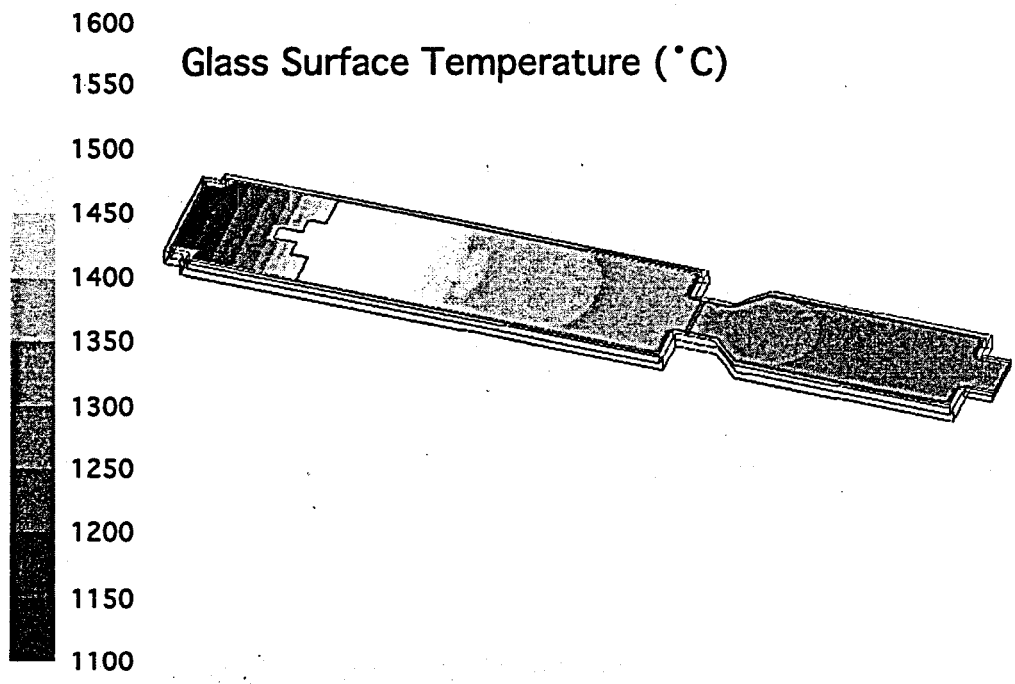

Figure 49. Predicted temperature profile on the glass surface (100% firing).

Oxy/fuel burners can be rearranged according to the heat flux requirements, resulting in improved glass temperature profiles and more uniform radiation heat flux. Therefore, the quality of the glass melt can be improved.

Higher flame temperature, increased residence time, and more flexible burner arrangement all help increase the thermal efficiency and reduce pollutant emissions. As shown in Figures 50 to 52 and Tables 9 to 12, the theoretical energy savings for the oxy/fuel furnace may be greater than 30% (Newbold *et al.*, 1997). Of course practical limitations, such as incomplete mixing, foam resistance, and heat loss, may reduce the savings to 20-25%.

Figure 50 shows predicted crown temperature profiles along the centerline of the combustion chamber. Figures 51 and 52 show the predicted melt surface and bottom temperatures along the tank centerline. The crown and melt surface temperatures were lower at the doghouse end because the batch is an effective heat sink for both the combustion space and the glass melt. The crown and melt surface temperatures were highest in the flame zone, where the combustion energy supplied to the glass melt is high, and the emissivity of the molten glass is high (0.9 compared with 0.6 for the batch).

The sharp dip in melt temperature at the 60-percent-length location in Figure 51 is due to the removal of heat to simulate the water cooler located in the neck zone. The melt temperature changed smoothly in the conditioning zone because there were no burners in this part of the furnace

Figures 50-52 indicate that the crown, glass surface, and tank bottom temperatures increased with increasing firing rate. Increasing the firing rate did not alter the shape of the predicted profiles. However, the extremes in firing rate (from 84% to 133% firing) resulted in increases in crown and glass surface temperatures of 100 K or more. The glass bottom temperature exhibited less sensitivity to the firing rate than the crown and glass surface temperatures.

3.2.2 Model Enhancements

Batch Islands

The boundary between batch and molten glass is not steady and well defined. The batch is introduced intermittently to the furnace because of the operating characteristics of the batch feeder, entering in discrete clumps or "logs." In addition, the molten glass recirculation pattern and batch melting contribute to batch movement at the surface near the batch blanket/glass interface. Lateral movement of the batch blanket was also observed, with the blanket shifting cyclically with the firing direction. This cyclic surface motion was observed to be toward the exit port side during firing, returning slightly more to the center during reversal, then shifting to the opposite port side as firing began in that direction. This movement contributes to the formation of "batch islands," discrete clumps of batch material found near the boundary between the batch blanket and molten glass. The transient nature of the boundary between the batch blanket and molten glass has been clearly established, although quantitative details of the contributing phenomena and specifics of their observed transient effects have not been thoroughly studied.

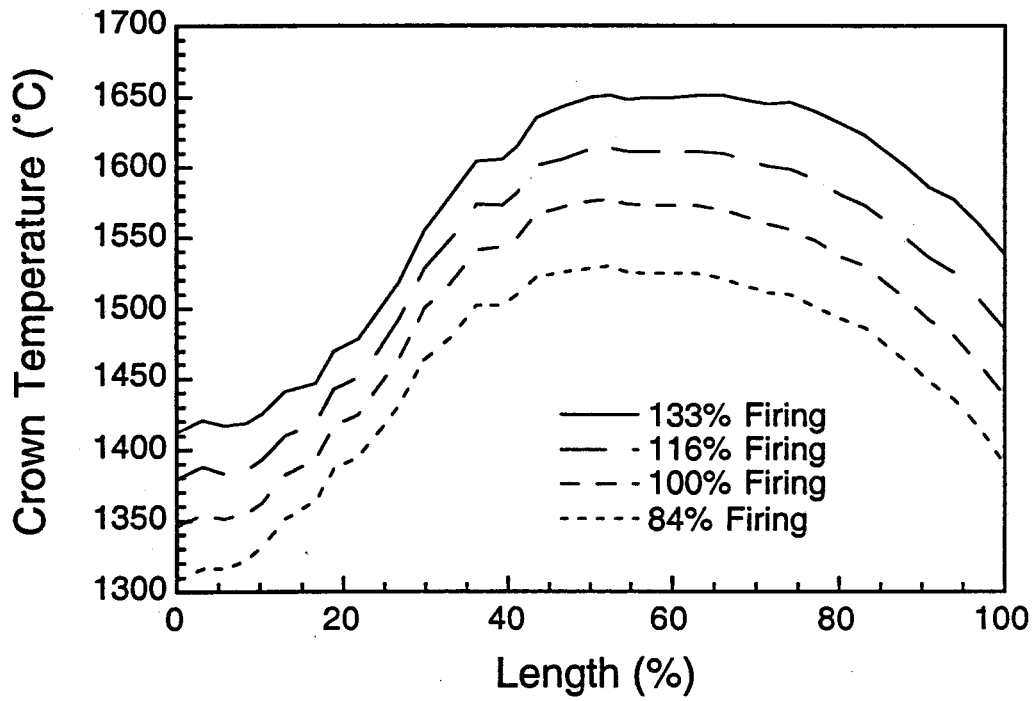

Figure 50. Predicted crown temperatures at the center of the furnace.

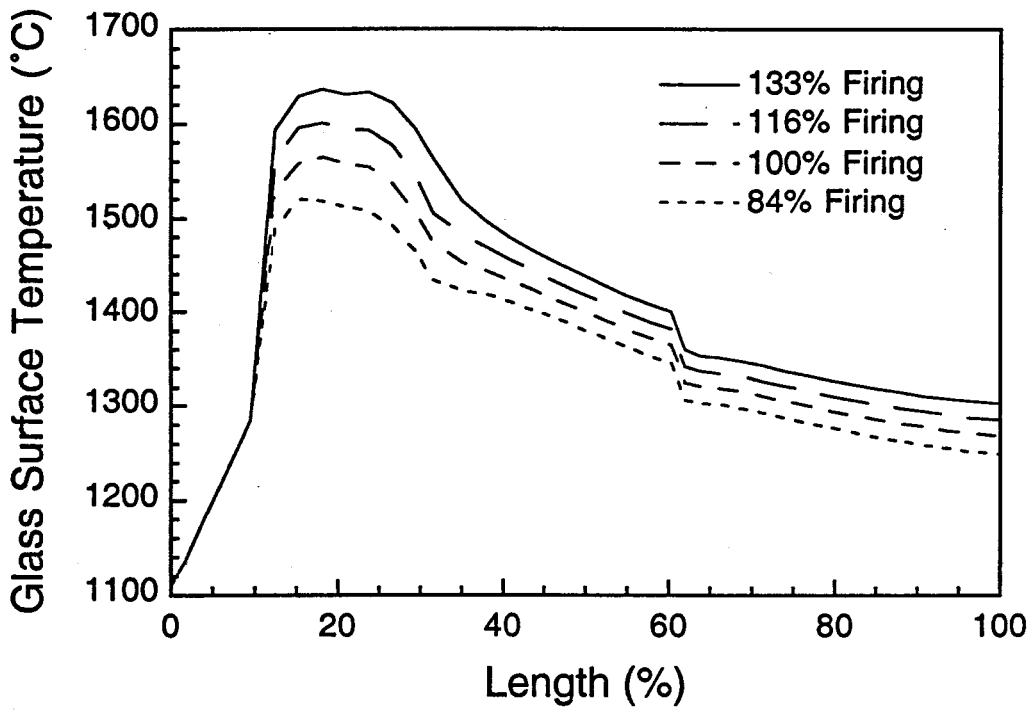

Figure 51. Predicted glass surface temperatures at the center of the tank.

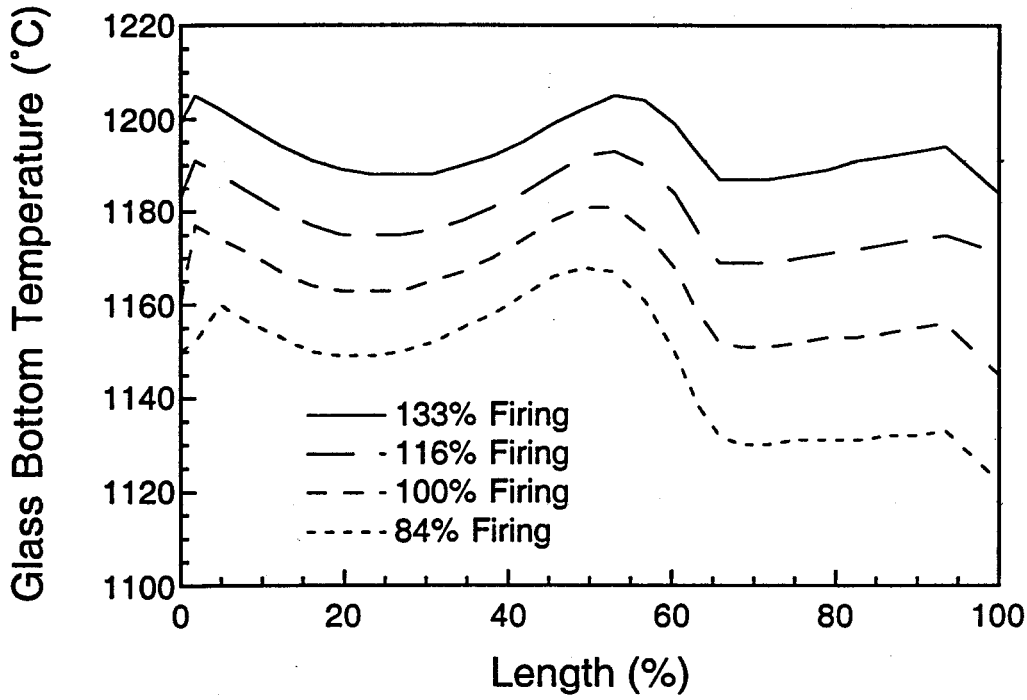

Figure 52. Predicted glass bottom temperature at the center of the tank.

In order to account for the effects of batch islands, the batch area was divided into two zones as shown in Figure 36. In the batch blanket zone, the batch was assumed to completely cover the melt surface. In the batch island zone, the batch was assumed to cover only a portion of the melt surface. The local temperature "seen" as a thermal boundary condition by the crown/combustion space in the batch island zone was approximated as an area-weighted average of the temperature of the batch island and its neighboring melt surface in a given computational cell:

$$T_{surf} = f\,T_{batch} + (1 - f)\,T_{glass} \tag{8}$$

Here, f is the batch island fraction, and T_{batch} and T_{glass} are the local batch and glass surface temperatures, respectively. Likewise, the batch/melt surface emissivity was approximated as an area-weighted average of that used for the batch and melt surface. The resulting heat flux predicted by the combustion chamber model was then proportionately distributed to batch island and melt surfaces based on their respective areas. The temperature dependent physical properties of the batch and the batch behavior model are described by the same equations in both zones.

Effect of Soot

Parametric simulations were performed to investigate the effect of including soot radiation. The solution was carried out on two HP C360 workstations. The combustion chamber model ran on one workstation and the glass tank and batch melting models ran on the other workstation. A heat flux boundary condition was used for the glass surface in the melting section, and an adiabatic condition was assumed for the glass surface in the conditioning section from the neck to the outlet. In the batch island zone, it was assumed that the batch occupies 85% of the melt surface area (Wang *et al.*, 2000b).

The boundary conditions (glass/batch surface temperature, emissivity, and heat flux) were updated every fifteen iterations. An information flow diagram was shown previously in Figure 40. Converged results were obtained after approximately 8,000 iterations for the combustion chamber model and 10,000 iterations for the tank model.

The crown and combustion chamber walls were assumed to have a heat loss of approximately 2 and 5 kW/m^2, respectively. The tank model also included a specified heat loss at the tank neck to simulate the effects of a water cooler.

Predicted gas temperature at the fuel inlet plane is shown in Figure 53. The flame region is clearly evident. There are recirculation zones at both ends of the combustor, which distort the flames from Ports 1, and 6 so that they do not flow directly across the combustion chamber to their respective exhaust ports. The penetration of the flames into the combustion chamber is quite good, providing for excellent heat transfer to the melt tank. The predicted average exhaust gas temperatures compare well to the measurements. The average of the predicted exhaust temperatures for the outlet ports was 1764 K as compared with 1758 K for the average of the measured values (McQuay *et al.*, 2000).

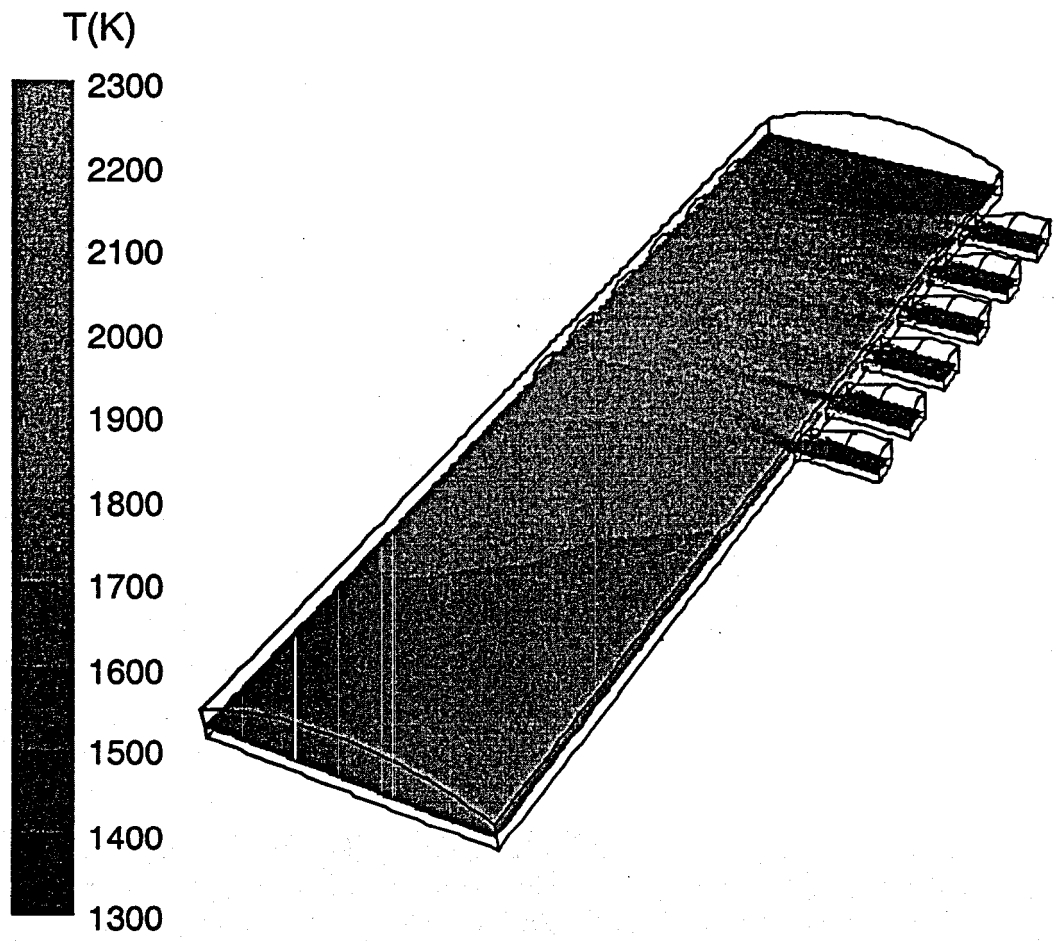

Figure 53. Predicted gas temperature at the fuel inlet plane with soot radiation included.

Predicted and measured concentrations of O_2 and CO_2 in the exhaust gas are given in Tables 14 and 15, respectively. Predicted oxygen concentrations are within one percent of the measured values with the exception of Port 6 where the fuel distribution was unique (see Table 3) and the possibility of oxygen bypassing the weak flame in that port was high. Measured carbon dioxide concentration exceeded the predicted values at all ports, but especially at Ports 1 and 2, where the batch was melting. It is estimated that over 2000 kg/hr of carbon dioxide was generated by batch melting reactions (McQuay *et al.*, 2000). This source of CO_2 was neglected in the combustion chamber model.

The predicted net heat flux from the combustion space to the glass/batch surface is shown in Figure 54. It is highest in the batch zone, where the surface temperature was lowest. The batch boundary is clearly evident.

Predicted glass surface temperature with and without soot is shown in Figure 55. As expected, soot enhanced the radiative heat flux and accelerated the batch melting. The total radiation heat flux with soot included was almost identical to that without soot (20,700 kW), but the maximum flame temperature with soot was 285 K lower than without soot. Less nitrogen oxide was produced when soot was included (13.7 compared with 15.3 kg NO/ton of glass) because of the lower flame temperature. Oxygen and carbon dioxide mole fractions were unaffected.

Predicted and measured incident radiant flux at the crown centerline is shown in Figure 56. The predictions agree with the experimental data in terms of both magnitude and shape of the profile. Including soot enhanced the radiation heat transfer and improved the agreement with the data, especially in the early flame region.

Figure 57 shows the predicted and measured profiles of crown temperature. Again, there is good agreement. Including soot radiation increased the maximum crown temperature by about 40 K.
Predicted and measured glass surface temperatures are shown in Figure 58. The rapid heating of the batch is evident. Again, the profile shape and magnitude were predicted very well, especially when soot radiation was included. Predicted batch coverage is shown in Figure 59. The batch melted more quickly when soot radiation was included. Since the value of radiation heat flux was higher on the flame inlet side for the simulation with soot included, the batch melted more quickly on this side (see Figure 59).

Effect of Batch Island Coverage

The sensitivity of the model predictions to the assumed batch coverage in the batch island zone was investigated by performing four parametric calculations with the following coverage: 100%, 90%, 85%, and 80%. The effect of air bubblers was also included. The bubblers were located in a transverse line on the tank bottom near port 4. Operation parameters (number of bubblers, flowrate, position relative to the tank bottom, orifice diameters, etc) were taken from plant data. The bubbler submodel was incorporated into FLUENT 4 using a user subroutine. Details are given by Wang (1998).

Table 14. Predicted and measured oxygen concentration.

	Average O_2 % (Mole Fraction)	
Outlet Ports	Measured	Calculated
1	2.3	1.5
2	2.4	2.4
3	1.7	2.0
4	1.3	2.0
5	6.3	5.4
6	9.0	6.8

Table 15. Predicted and measured carbon dioxide concentration.

	Average CO_2 % (Mole Fraction)	
Outlet Ports	Measured	Calculated
1	17.0	8.7
2	15.4	8.7
3	10.4	8.8
4	10.5	8.7
5	8.6	7.2
6	7.2	6.6

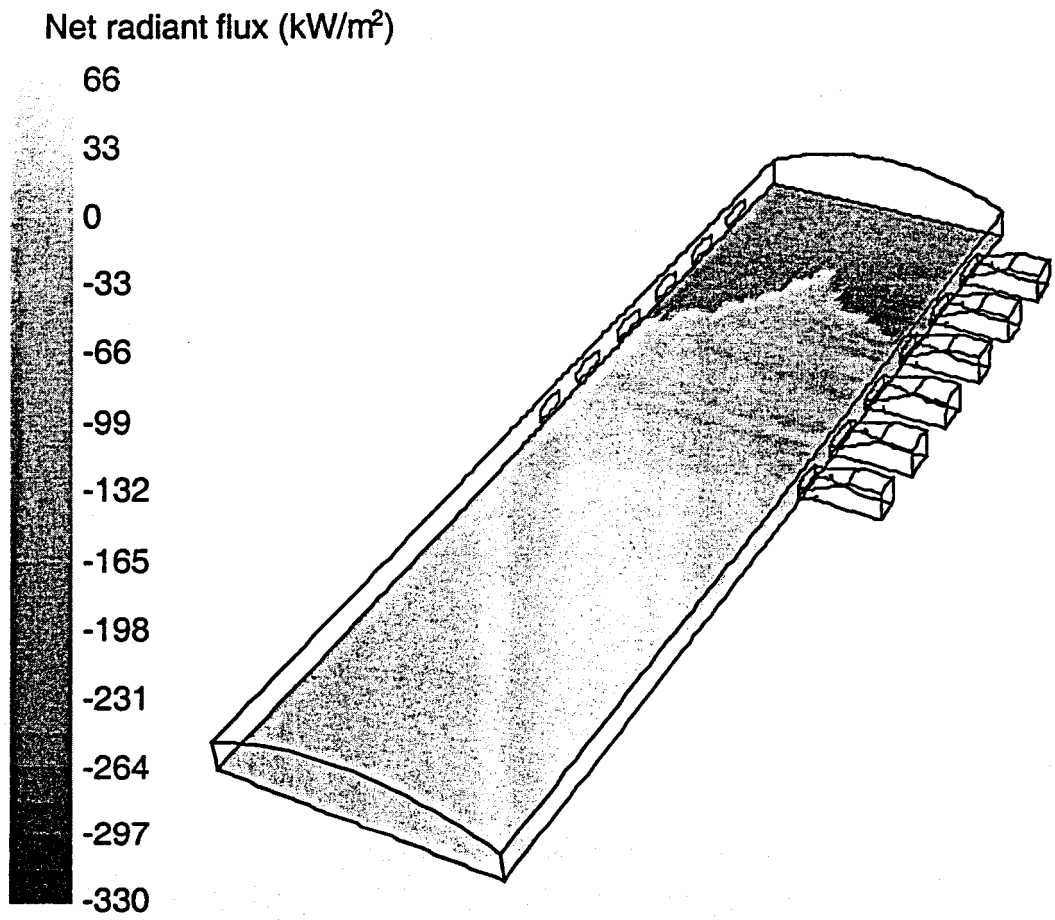

Figure 54. Predicted net flux to the glass/batch surface with soot radiation included.

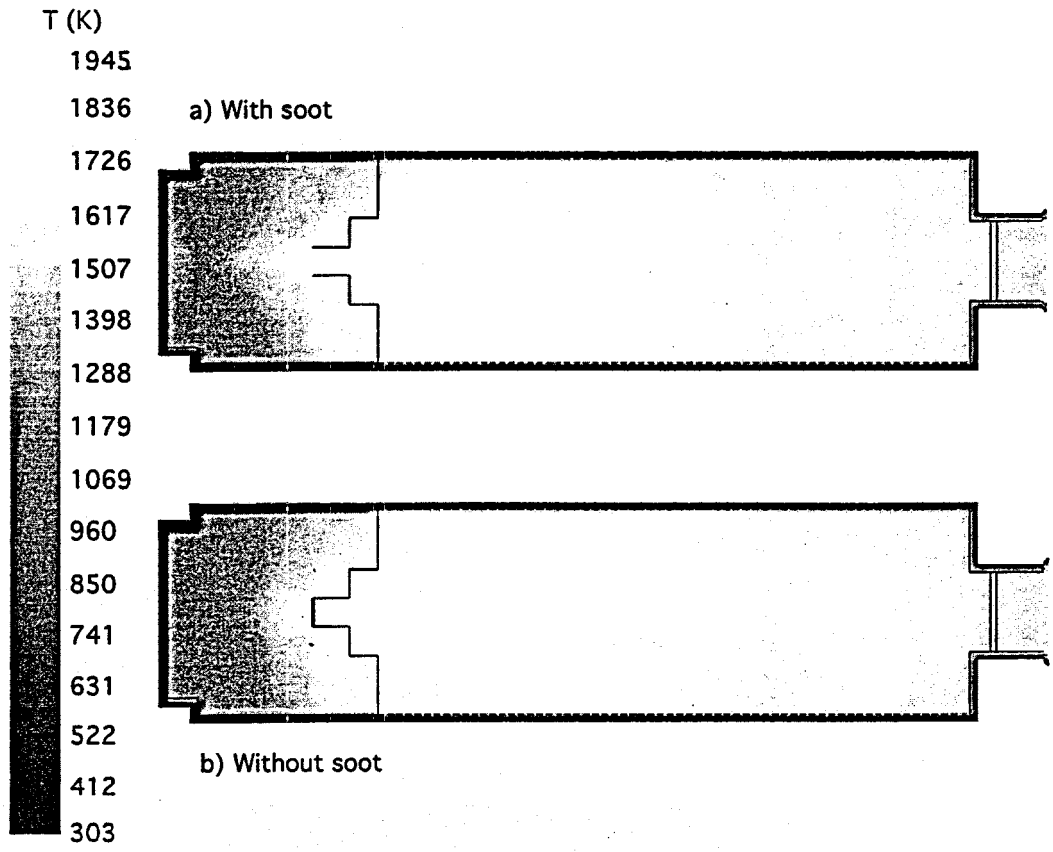

Figure 55. Predicted glass surface temperatures: (a) without soot (b) with soot.

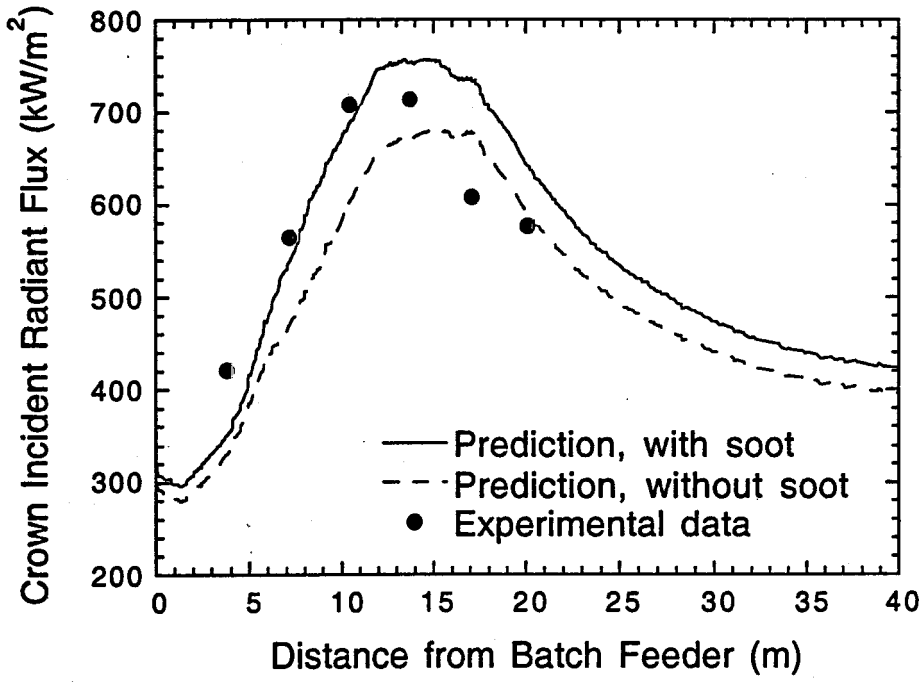

Figure 56. Predicted and measured crown incident radiation flux along the furnace centerline.

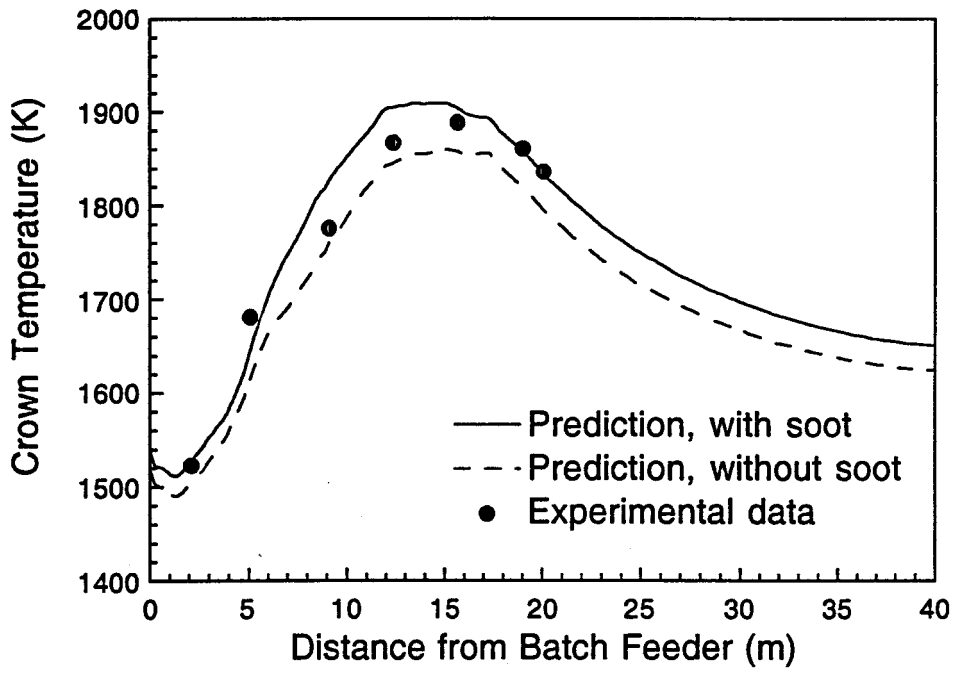

Figure 57. Predicted and measured crown temperature.

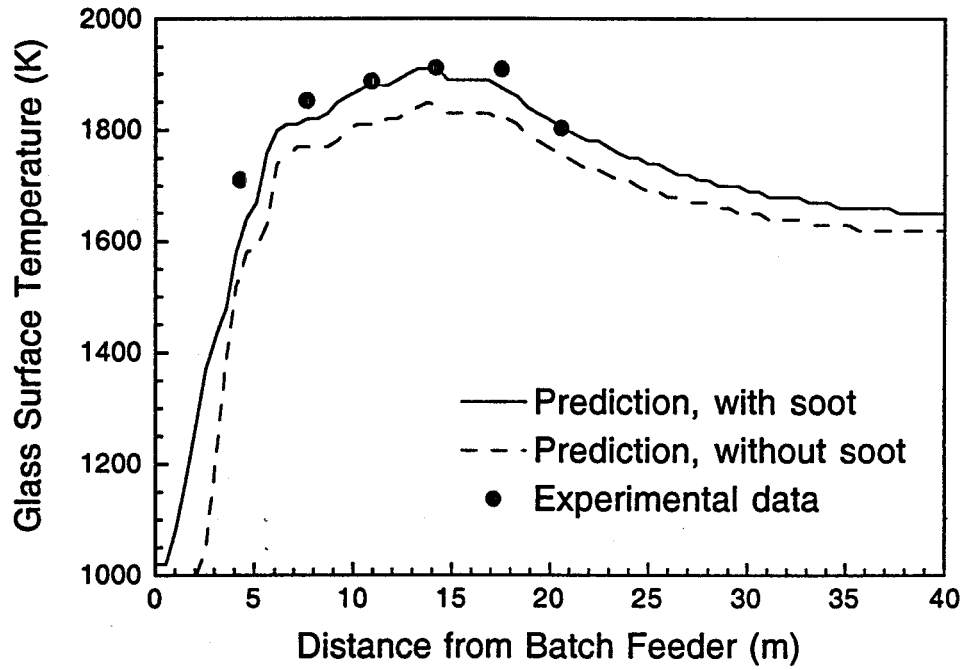

Figure 58. Predicted and measured glass and batch surface temperature along the furnace centerline.

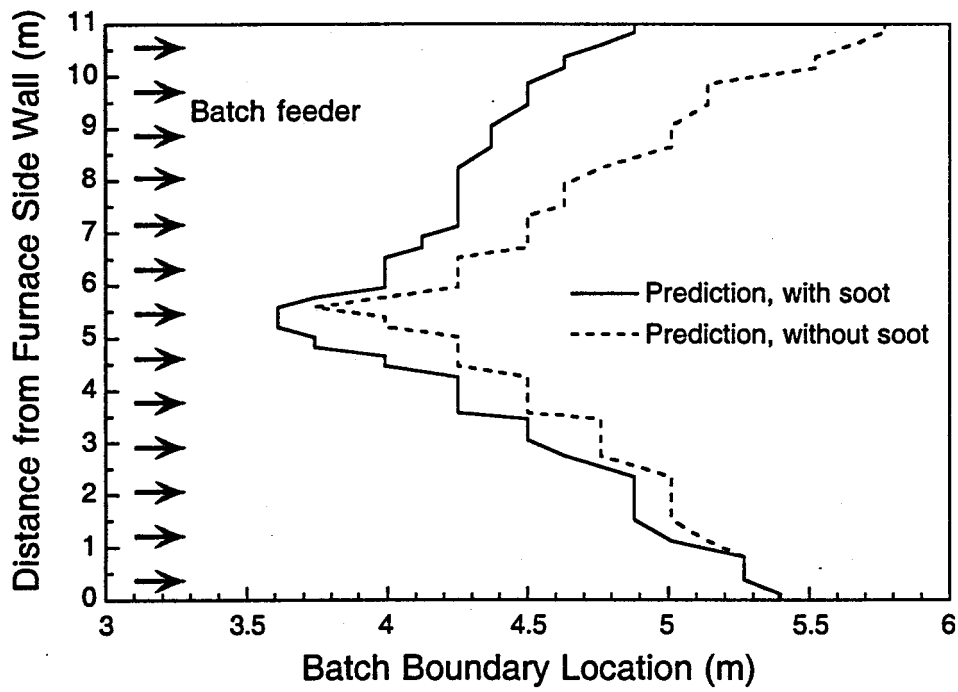

Figure 59. Predicted batch coverage.

Figure 60 illustrates the predicted total batch coverage. As the batch fraction decreased, the total batch blanket coverage increased. Melting on the firing side (top of figure) was accelerated due to exposure to the highest flame temperatures, producing asymmetry in the batch boundary about the furnace centerline. The asymmetry increased with decreasing batch fraction in the island zone. The difference in batch length at the furnace sides was approximately 1 m for 80 percent coverage in the island zone. It is also noted that the predicted total batch coverage varied by as much as 80% for the two imposed batch fraction extremes studied. The increased batch coverage (with associated relatively cooler temperatures seen by the flame) at low batch fractions resulted in considerably higher total heat transfer from the flame to the batch/melt.

The predicted gas temperature distribution at the fuel inlet plane for 85% coverage in the island zone is shown in Figure 61. Penetration of the flames into the combustion chamber provides effective heat transfer from the flame to the batch and melt. Ports 1 and 6 exhibited reduced flame temperatures because of the proximity to the batch feeder and significantly reduced firing rate, respectively. The peak gas temperature was observed to be near port 4 at approximately 2300 K.

The calculated net heat flux from the combustion space to the glass melt or batch surfaces for 85% coverage in the batch island zone is shown in Figure 62. Negative values of the net heat flux indicate net heat transfer *to* the glass melt and batch. Figure 63 shows the corresponding predicted glass melt and batch surface temperature distributions. The predicted heat transfer to the batch/melt was highest in the batch zone where the surface temperature is the lowest. As expected, the predicted surface temperature was lowest in the batch melting area and highest at the free surface of the melt, downstream of the batch area. Maintaining the glass temperature high in the melting zone of the tank is important for efficient batch melting, proper melt flow pattern (*e.g.*, a distinct spring zone), glass homogenization, and fining (degassing of the melt). As there is no heating source in the conditioning zone, the melt temperature decreases slightly as the glass flows out of the melter due to heat losses through the tank bottom and sidewalls.

A comparison of predicted and measured glass surface temperatures along the furnace centerline is shown in Figure 64. The heating of the batch is clearly evident by the rapid rise in batch surface temperature early in the furnace (0-5 meters from the doghouse). The batch melted more quickly for high batch fraction. As suggested by the temperature profiles of Figure 64 and confirmed by the melt surface velocity predictions (not shown), the melt hot spot (spring zone) moved slightly toward the working end as the batch fraction decreased. While the predicted glass surface temperature profiles for 85, 90, and 100% batch fraction are quite close in magnitude, the 80% batch fraction simulation exhibited considerably lower surface temperatures for the same fuel input. This sensitivity to the imposed batch coverage fraction in the batch island zone will be observed subsequently for other predicted quantities discussed hereafter. Neglecting the measurement in the region of rapid heating near the batch feeder, the predicted glass surface temperature for 85% coverage in the batch island zone agrees with the measured values to within 40 K.

Average furnace exhaust temperature predictions are shown in the inset panel of Figure 64. The average exhaust temperature is the mass flow-weighted average of the furnace gas outlet temperatures over all exhaust ports. Higher heat transfer from the flame to the expanded batch coverage, which resulted when the batch coverage in the island zone was decreased, yielded reduced

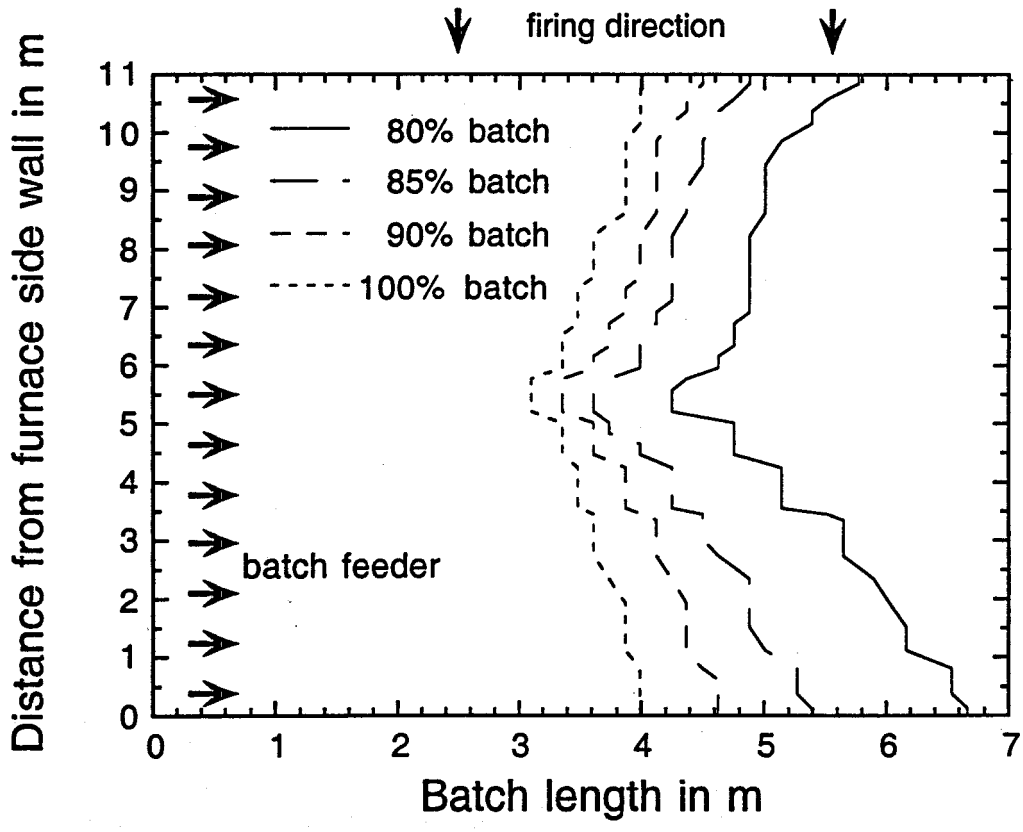

Figure 60. Predicted batch boundary location for different batch coverage fractions in the batch island zone.

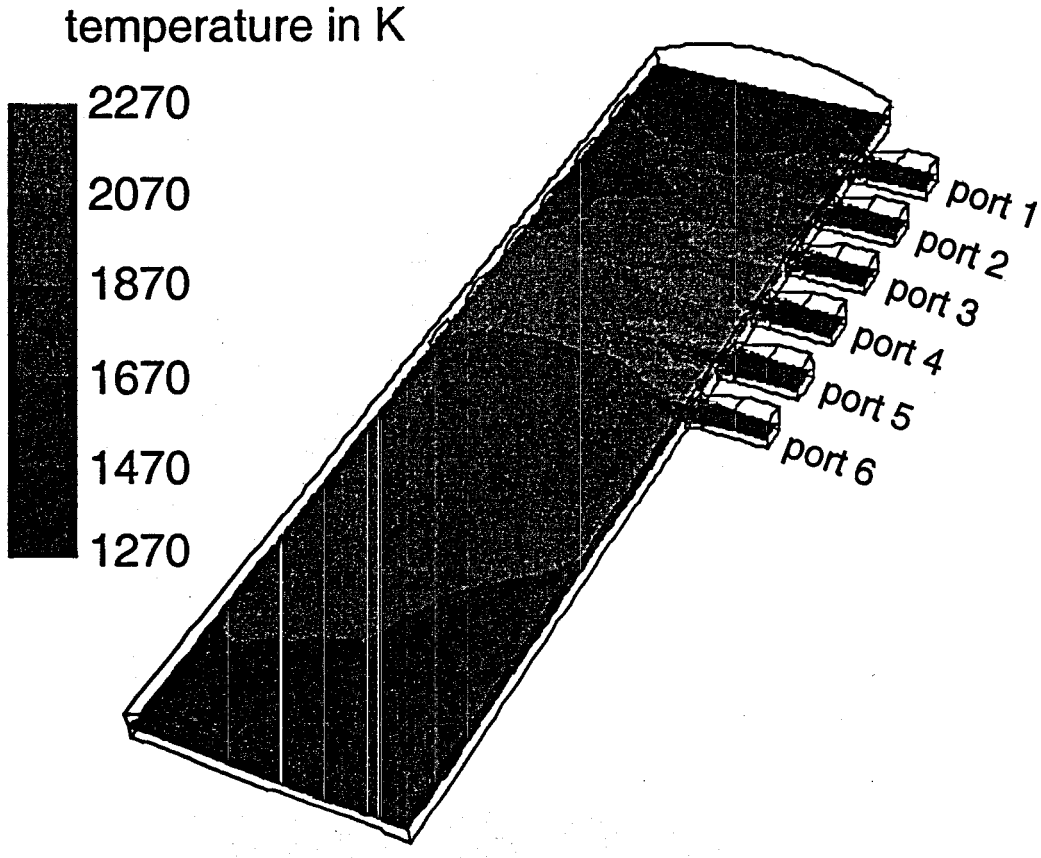

Figure 61. Predicted gas temperature distribution in the combustion space at the fuel inlet horizontal plane (85% batch coverage in the batch island zone).

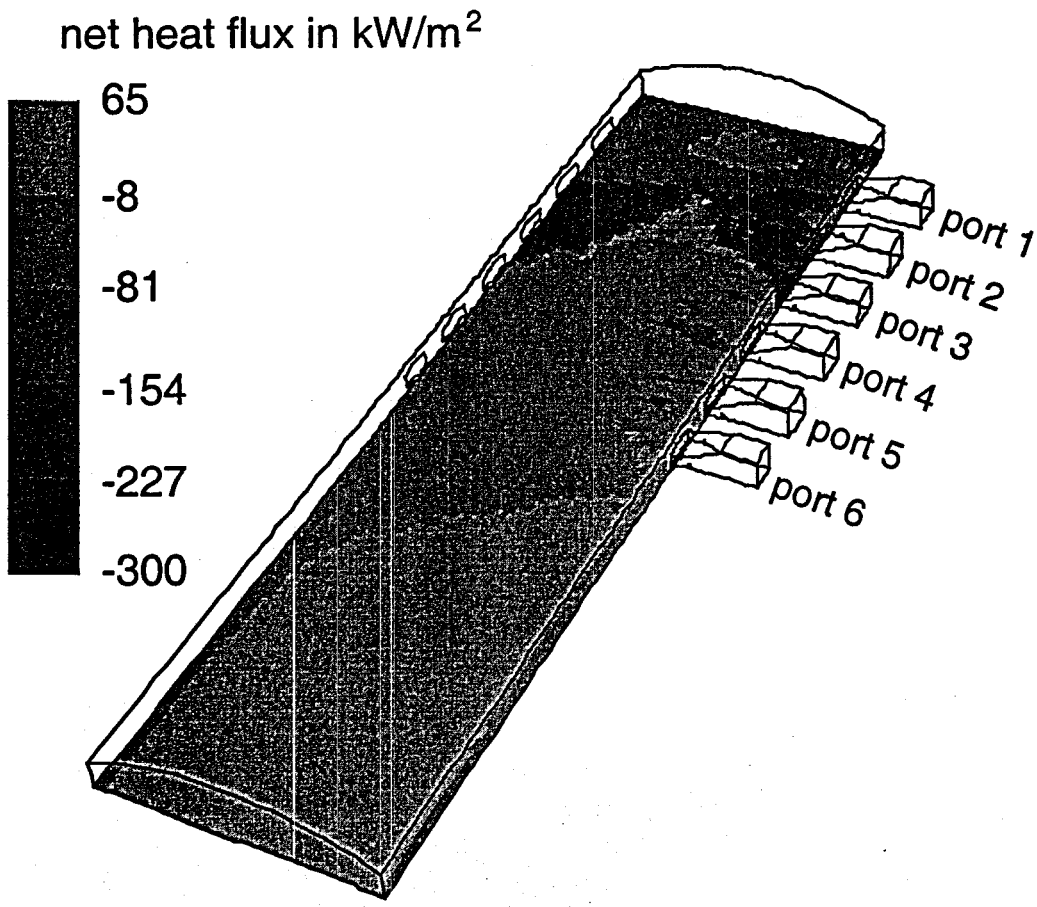

Figure 62. Predicted heat flux distribution from the combustion space to the batch and glass melt surfaces (85% batch coverage in the batch island zone).

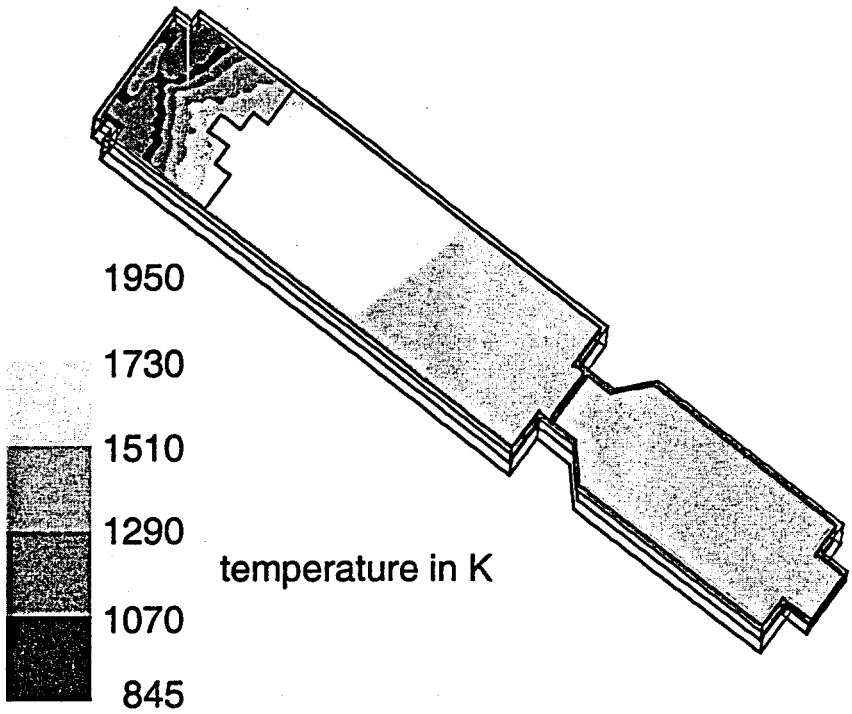

Figure 63. Predicted glass/batch surface temperature distribution (85% batch coverage in the batch island zone).

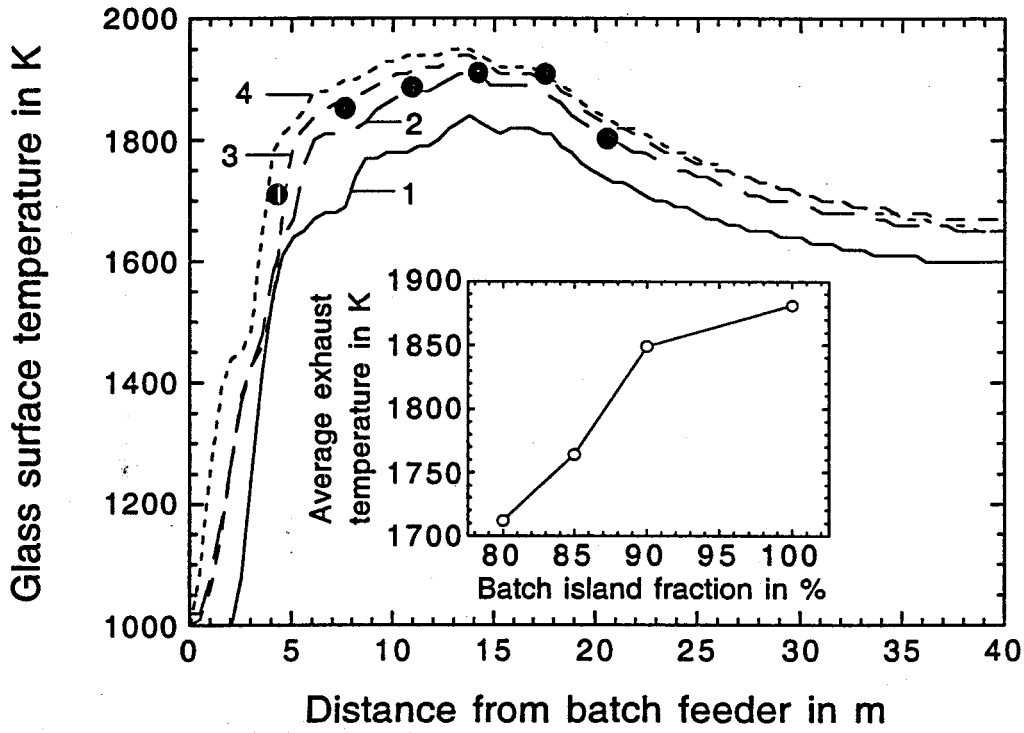

Figure 64. A comparison of predicted and measured glass surface temperatures along the furnace centerline for different batch coverage fractions in the batch island zone (●– experimental data, curve 1 – 80% batch fraction, curve 2 – 85% batch fraction, curve 3 – 90% batch fraction, and curve 4 – 100% batch fraction). Inset panel: Predicted average furnace exhaust temperature as a function of batch coverage fraction in the batch island zone.

furnace exhaust temperatures. The average predicted exhaust gas temperatures for all six ports was 1764 K for 85% coverage as compared with the measured value of 1758 K (McQuay *et al.*, 2000).

The model predicted two complex, buoyancy-driven, three-dimensional recirculation flow patterns in the glass tank. One was in the region between the batch feeder and the spring zone, and the other was located between the spring zone and the working end. Figure 65 shows the predicted velocity vectors on the glass surface for 85% coverage. The figure clearly illustrates the location of the spring zone where melt rising from the bottom of the tank reaches the free surface and bifurcates, flowing in opposite directions towards the batch feeder and the neck. Predicted maximum surface velocities reaching 7 mm/s occurred near the batch. The predicted melt velocity was large also at the neck zone of the tank. The asymmetry (about furnace axial centerline) in the predicted melt surface flow structure was a result of the imposed furnace firing configuration in the model (firing direction was from bottom to top in Figure 65). Also of note in the vector plot is the absence of surface backflow that often exists along the sidewalls between the refining section and the melter. It is critical that a full furnace simulation include both melting and refining sections in order to predict recirculation and its impact on glass quality.

The predicted and measured crown incident radiant flux profile along the furnace centerline is compared with experimental measurements in Figure 66. The experimental uncertainty in the measurements is ±15% (Hayes *et al.*, 2001). Generally speaking, the incident flux increased from the batch feeder to a maximum at a location 13 m from the doghouse, then decreased towards the refiner. The prediction for 85% batch coverage in the island zone agrees well with the experimental data in both profile shape and magnitude until approximately 15 meters downstream from the batch feeder. The location of peak heat flux was predicted well by the model. As the batch fraction increased, the incident radiant flux on the crown increased due to the higher melt surface temperatures. The predicted incident flux appears to be quite sensitive to the assumed batch fraction, particularly at low values (*i.e.*, 80% batch).

The predicted total heat transfer to the glass melt and batch surfaces as a function of batch island fraction is illustrated in the inset panel of Figure 66. As seen in the panel, the total transport decreased as the batch fraction increased. The differences are quite dramatic, with a 20% decrease in total heat transfer between 80% coverage and 100% coverage in the island zone. Greater low-temperature batch coverage on the melt surface resulted in increased total heat extracted from the flame and crown.

Figure 67 shows the predicted profiles of crown temperature along the furnace centerline. Measurements of crown temperature from plant furnace control measurements are also included in the figure. Not surprisingly, the location of predicted peak calculated crown temperature coincides with the location of maximum incident crown flux seen in Figure 66. The calculated crown temperature is only slightly lower than the glass surface temperature at the same location. Higher imposed batch fractions resulted in higher crown temperatures. Again, 85% coverage in the island zone compares most favorably with the experimental data.

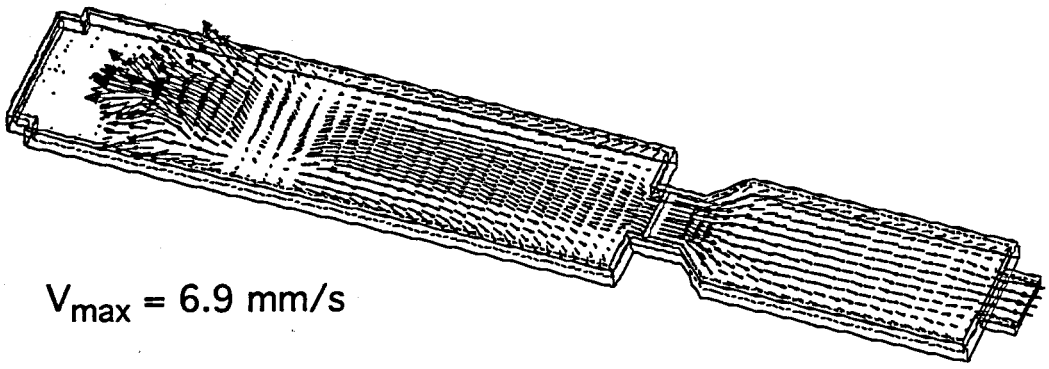

Figure 65. Predicted velocity vectors on the glass surface (85% batch coverage in the batch island zone).

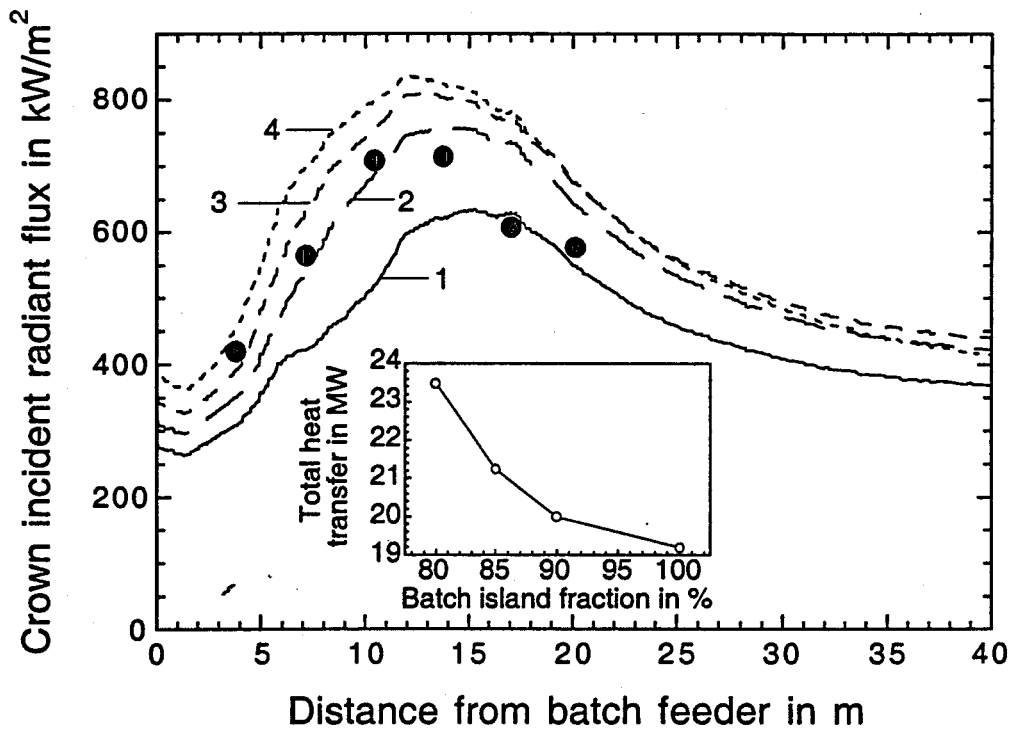

Figure 66. A comparison of predicted and measured crown incident radiation fluxes along the furnace centerline for different batch coverage fractions in the batch island zone (● – experimental data, curve 1 – 80% batch fraction, curve 2 – 85% batch fraction, curve 3 – 90% batch fraction, and curve 4 – 100% batch fraction). Inset panel: Predicted total heat transfer to batch and melt as a function of batch coverage fraction in the batch island zone.

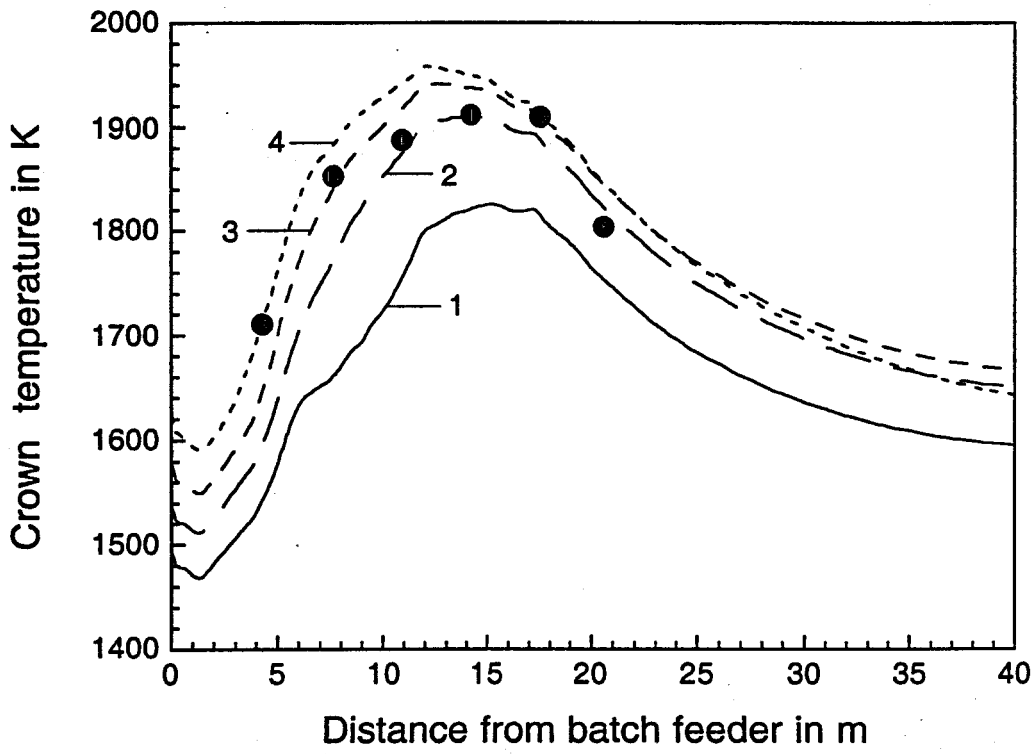

Figure 67. A comparison of predicted and measured crown temperatures along the furnace centerline for different batch coverage fractions in the batch island zone (● – experimental data, curve 1 – 80% batch fraction, curve 2 – 85% batch fraction, curve 3 – 90% batch fraction, and curve 4 – 100% batch fraction).

4. TECHNOLOGY TRANSFER

4.1 Ford Float Glass Furnaces

The majority of this report outlines the project effort targeting model development and validation for Ford Motor Company's Glass Division. These furnaces were regenerative, air/fuel-fired float glass furnaces. As has been outlined, the model was used to explore the possibility of changeover to oxygen/fuel firing. Further, the model was used by Ford to explore the impact of incremental design changes in the Tulsa No. 1 furnace prior to its rebuild. Several of these changes were made, improving air flow in the portnecks and combustion space. Modeling for these design changes has been summarized in foregoing sections.

4.2 Fiberglass Unit Melter Furnace

The coupled model developed as part of this study was extrapolated to the fiberglass unit melter modeling environment. This presented a significant extension to the modeling work which had been done previously, as it included bubblers and significant electrical boosting. The furnace, shown schematically in Figure 68, is a 177 ton/day oxygen-fuel fired furnace. The furnace features six burners on each breast wall, arranged in a staggered configuration. The furnace exhaust is located on the doghouse wall. A dual doghouse configuration feeds raw materials onto the melt surface. Significant electrical boosting is used to enhance motion of the molten glass and provide energy for batch melting. Bubbling was used to further enhance the mixing in a desired fashion. The molten glass exits the melt tank through a submerged throat to a conditioning channel before being distribution to a series of platinum bushings. The presence of the electrodes in the melt tank adds considerable geometric complexity to the furnace. Further, the boosting adds greater difficulty in achieving the coupling between tank and combustion space.

The fiberglass unit melter model extension has been used by the licensee to explore different bubbler locations, different electrode configurations and total power input, as well as unique tank designs. While the results of these design explorations are proprietary, they nevertheless underline the model's utility in investigating possible design changes.

4.3 Container Glass Furnace

A second extension has been made to the coupled model was a side-charging container glass furnace. The melt tank and combustion space are illustrated schematically in Figure 69. This configuration was developed for Tokyo Gas Company, a supplier of liquefied natural gas to glass manufacturers in Japan. This furnace is a 95 ton/day air/fuel fired furnace with significant cullet content. The furnace is under-fired and is non-regenerative. Air is mixed with natural gas in the inlet, follows a horseshoe path and exits through the exhaust duct located on the same furnace wall as the furnace inlet. The raw materials/cullet is introduced through the doghouse on the side wall of the furnace. The batch wall was modified to allow side-charging as shown in Figure 70. The batch is fed into the furnace from the doghouse that is located at the side wall of the furnace. In the batch model, it was assumed that the batch flow from the doghouse to the opposite side wall, then changes flow direction and flows to the front wall. The batch is fed into the furnace from the start point of the side wall to the end point of the doghouse (see Figure 69).

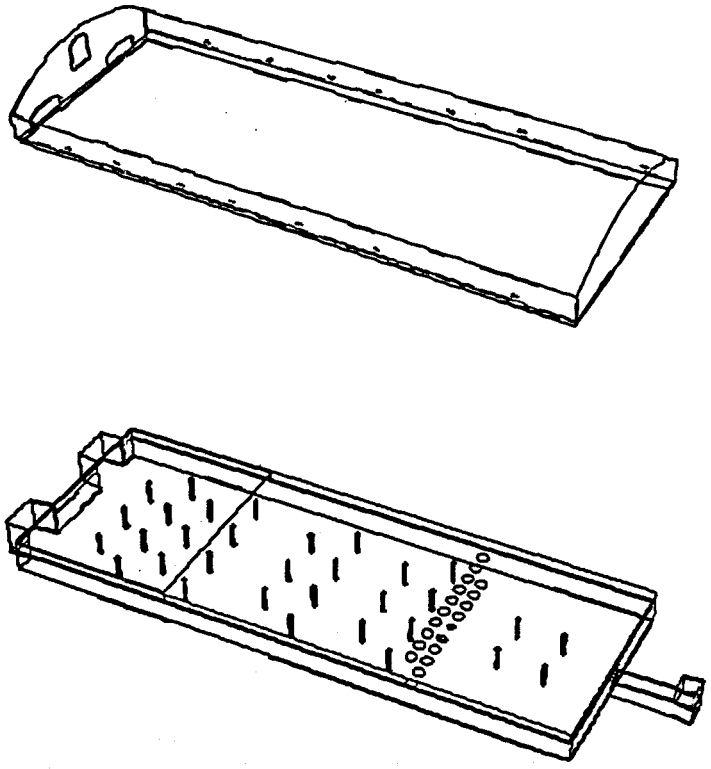

Figure 68. Schematic of fiberglass unit melter furnace modeled.

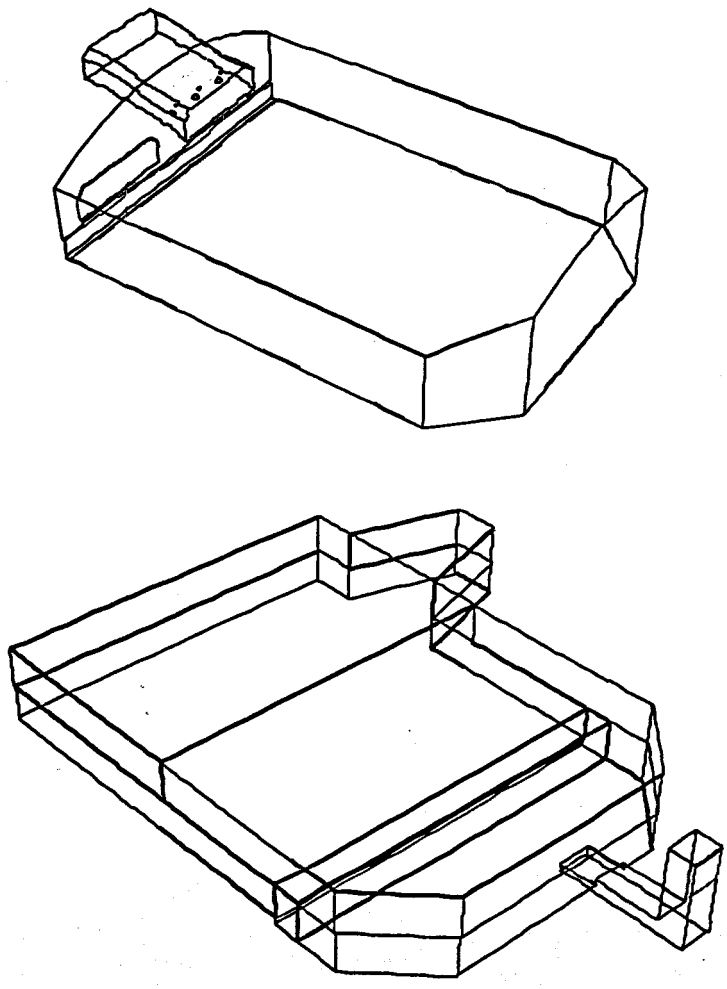

Figure 69. Schematic of side-charging container glass furnace modeled.

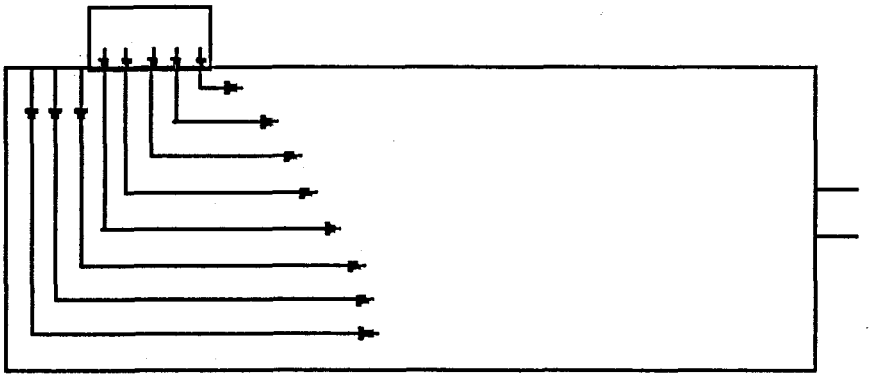

Figure 70. Illustration of batch feed model modification made for side-charging container glass furnace coupled model.

The side-charging batch modification represented a significant enhancement to the model's capability. The coupled model has been used by the licensee to explore oxy-natural gas combustion technology (Fujisaki *et al.*, 2001), and development of high radiative, low-NO_x oxy-natural gas burner designs for glass melting furnaces (Hashimoto *et al.*, 2001).

5. CONCLUSIONS

The experimental data reported in this study are unique. For the first time, profile measurements in the combustion space of an operating furnace have been reported. For the first time, the effect of rebuild on furnace performance has been investigated. And for the first time, glass surface temperature and crown heat flux have been measured.

The measured concentrations of O_2, CO, and CO_2 in the exhaust indicate incomplete combustion. Concentrations of CO_2 were significantly higher than predicted from chemical equilibrium of the fuel and oxidizer because of CO_2 generation by the batch melting reactions.

Steady state was established almost immediately after firing direction reversal. Only CO concentration required 4-5 minutes into the burn cycle to stabilize. The two firing directions showed good symmetry for velocities, crown heat flux, and CO_2. O_2 and CO showed relatively large deviations from symmetry.

Simulations of the combustion chamber based on furnace blueprint and plant operating values for fuel and air flowrates suggested that there was considerable error in the plant-measured air flowrate. Without furnace effluent measurements, the modeler must rely on data provided by the plant operators. Accurate boundary conditions (inlet air and fuel flow distribution, boundary surface temperatures, etc.) are critical in simulating industrial combustion systems.

The inclusion of soot radiation in the model increased the predicted heat loss and caused the predicted average exhaust gas temperature to decrease. The average NO_x concentration at the exit was also affected and decreased significantly. Soot radiation is significant in glass furnace modeling and should be included.

Modeling provides a cost-effective tool for investigating new pollutant reduction strategies. Use of an oxygen lance (intended to reduce NO_x by combustion staging) increased the NO_x formation by almost 100% through increasing the gas temperature. Using pure oxygen instead of preheated air reduced the total NO_x formation but increased the exit concentration because of the lower flowrate that came from removing nitrogen from the air.

Rebuilding the furnace made the exhaust species concentration profiles in the portnecks more uniform and lowered the required fuel flowrate significantly.

Predicted glass surface temperature agreed well with the experimental data, including the location of the spring zone. The predicted crown incident radiant heat flux during firing cycles qualitatively showed similar trends as the experimental results but was over predicted by 5-15%.

6. ACKNOWLEDGEMENTS

Financial support of the U.S. Department of Energy through Agreement DE-FC02-95CE41187 and Ford Motor Company's Visteon Glass Systems Division is gratefully acknowledged. DOE contract monitor is Mr. Edward Gallagher. Additional support of the National Science Foundation through the Advanced Combustion Engineering Research Center is also acknowledged. Ford Glass Plant support by Denny Fryz and Ken Traud is appreciated. The help and support of Todd Moss and Don Wallace of the BYU Mechanical Engineering Department during equipment procurement and instrument calibration is also appreciated.

7. REFERENCES

Boerstoel, G.P., van der Meer, T.H., Hoogendoorn, C.J. (1995) "Numerical Simulation of Soot Formation and Oxidation in High Temperature Furnaces," in the proceedings of ISTF-8, San Francisco.

Boerstoel, G.P., Wieringa, J.A., van der Meer, T.H. (1994) "Numerical Modeling of Soot Formation in Glass Melting Furnaces," *Heat Transfer in Radiating and Combusting Systems - 2,* Eurotherm Seminar, No. 37, pp. 167-180.

Butler, B.W. (1992) "An Experimental Evaluation of Radiant Energy Transport in Particle-Laden Flames," *Ph.D. Dissertation*, Brigham Young University, Provo, UT.

Butler, B.W., Webb, B.W. (1991) "Measurements of Local Temperature and Wall Radiant Heat Flux in an Industrial Coal-Fired Boiler," *Fuel* , Vol. 70, pp. 1457-1464.

Carvalho, M. G., Semião, V. S., Coelho, P. J. (1992) "Modeling and Optimization of the NO Formation in an Industrial Glass Furnace," *Journal of Engineering for Industry*, ol. 114 pp. 514-523.

Carvalho, M.G. (1983) "Computer simulation of a glass furnace," *Ph.D. Thesis*, Imperial College of Science and Technology, London, UK.

Carvalho, M.G. and Lockwood, F.C. (1990) "Thermal Comparison of Glass Furnace Operation with Oil and Natural Gas," *Glastech. Ber.*, Vol. 63 (9), pp. 233-243.

Carvalho, M.G., Durão, D.F.G., Pereira, J.C.F. (1987) "Prediction of the Flow, Reaction and Heat Transfer in an Oxy-Fuel Glass Furnace," *Engineering Computations*, Vol. 4 (1), pp. 23-34.

Carvalho, M.G., Lockwood, F.C. (1985) "Mathematical simulation of an end-port regenerative glass furnace," *Proceedings of the Institute of Mechanical Engineering*, Part C, Vol. 199, C2, pp. 113-120.

Carvalho, M.G., Nogueira, M. (1994) "Model-based study for improved oxy/fuel glass furnace conception," *The 9th Conference on Glass*, Hradec Kralove, Czech Republic.

Carvalho, M.G., Nogueira, M. (1995a) "Physically based modeling of an industrial glass melting end-port furnace," *4th International Conference on Advances in Fusion and Processing of Glass*, Worzburg, Germany, May 22-24.

Carvalho, M.G., Nogueira, M. (1995b) "Evaluation of the use of oxy/fuel firing technologies on the melting glass quality and furnace efficiency," *56th Annual Conference on Glass Problems GLASS 95*, University of Illinois at Urbana-Champaign, USA.

Carvalho, M.G., Nogueira, M., Wang, J. (1995a) "Mathematical modeling of the glass melting industrial process," *Proceedings of 17th International Congress on Glass*, Vol. 6, pp. 69-74, Beijing, China.

Carvalho, M.G., Nogueira, M., Wang, J. (1995b) "Assessment of Numerical Simulation of an Industrial Glass Melter," *Verre*, Vol. 1, pp. 9-13.

Carvalho, M.G., Nogueira, M., Wang, J., Ferlin, T., Malvos, H. (1996) "Model-Based Study of a Glass Melting Furnace for Reduced Particle Emission," *Proceedings of International Symposium on Glass Problems*, Vol. 1, pp. 398, Istanbul, Turkey, September 4-6.

Carvalho, M.G., Oliveira, P., and Semião, V. (1988) "A Three-dimensional Model of an Industrial Glass Furnace," *J. Inst. Energy*, Vol. 143, pp. 143-156.

Carvalho, M.G., Semião, V., Lockwood, F.C., Papadopoulos, C. (1990) "Predictions of Nitric Oxide Emissions from a Industrial Glass-Melting Furnace," *J. Inst. Energy*, March, pp. 39-42.

Carvalho, M.G., Speranskaia, N., Wang, J., Nogueira, M. (1997c) "Modeling of Glass Melting Furnaces: Applications to Control, Design and Operation Optimization," *Proceedings of Fifth International Conference on Advances in the Fusion and Processing of Glass*, Toronto, Canada, July 27-31.

Carvalho, M.G., Wang, J., Nogueira, M. (1997a) "Numerical simulation of thermal phenomena and particulate emissions in an industrial glass melting furnace," *Proceedings of Conference on Fundamentals of Glass Science and Technology*, pp. 416-421, Växjö, Sweden.

Carvalho, M.G., Wang, J., Nogueira, M. (1997b) "Physically-based numerical tool for the study of cleaner combustion in glass melting furnaces," *Proceedings of Fourth International Conference on Technologies and Combustion for a Clean Environment*, Vol. II, pp. 27.13-27.20, Lisbon, Portugal.

Cassiano, J., Heitor, M.V., Silva, T.F. (1994) "Combustion Tests on an Industrial Glass-melting Furnace," *Fuel*, Vol. 73 (10), pp. 1638-1642.

Chen, T., Goodson, R.E. (1980) "Computation of Three Dimensional Temperature and Convective Flow Profiles for an Electrical Glass Furnace," 18th AIAA Meeting on Aerospace Sciences, California.

Choudhary, M. (1985) "Three-dimensional mathematical model for flow and heat transfer in electric glass furnaces," *Heat Transfer Eng.*, Vol. 6, pp. 55-65.

Choudhary, M.K. (1997) "Needs of the glass industry defined for mathematical modeling," *The Glass Researcher*, 6, pp. 7-11.

Choudhary, M.K. (2000) "Mathematical modeling of transport phenomena in glass furnaces: an overview of status and needs," Proceedings ICG 2000 Amsterdam – Glass in the New Millennium, on CD-ROM, paper T1.1, pp. 1-12.

Choudhary, M.K.; Huff., N.T. (1997) "Mathematical modeling in the glass industry: an overview of status and needs," *Glastech. Ber.* 70, pp. 363-370.

Chui, E. H., Raithby, G. D. (1993) "Computation of radiant heat transfer on a non-orthogonal mesh using the finite-volume method", Numerical Heat Transfer, Part B, Vol. 23, pp. 269-288.

Costa, M., Mourão, M., Baltasar, J., Carvalho, M.G. (1996) "Combustion Measurements in an Industrial Glass Melting Furnace," *J. Inst. Energy*, Vol. 69, pp. 71-86.

Denison, M.K., Webb, B.W. (1995a) "The Spectral-Line Weighted-Sum-of-Gray-Gases Model in Non-Isothermal, Non-Homogeneous Media," *ASME J. Heat Transfer*, Vol. 117, pp. 359-365.

Denison, M.K., Webb, B.W. (1995b) "The Spectral-Line Weighted-Sum-of-Gray-Gases Model for H_2O/CO_2 Mixtures," *ASME J. Heat Transfer*, Vol. 117, pp. 788-798.

Denison, M.K., Webb, B.W. (1996) "The Spectral-Line Weighted-Sum-of-Gray-Gases Model – A Review," *Radiative Transfer, Proceedings of the First International Symposium on Radiation Transfer*, ed. M.P. Menguc, Begell House, New York, pp. 228-238.

Endrys, J. (1999) "Measurement of Radiative and Effective Thermal Conductivity of Glass," *Proceedings of the 5th ESG Conference*, Vol. A5, pp. 10-17.

Farmer, D., Heitor, M.V., Vasconcelos, A.T. (1992) "New Methodology for Furnace Monitoring, Analysis and Control," *Glass Ind.*, Vol. 10, pp. 10-16.

FLUENT NO_x Module User's Guide, Version 2 (1995c).

FLUENT User's Guide, Version 4.0 (1995a).

FLUENT User's Guide, Version 4.3 (1995b).

FLUENT User's Guide, Version 5.0 (1998).

Fuhrmann, H. (1973) "Contribution to the approximate calculation of the melting down of glass batch blanket", *Glastech. Ber.*, Vol. 46, pp. 201-208.

Gardon, R. (1961) "A Review of Radiant Heat Transfer in Glass," *J. American Ceram. Soc.*, Vol. 44, pp. 306-317.

Gosman, A.D., Lockwood, F.C., Megahed, I.E.A., Shah, N.G. (1980) "The Prediction of the Flow, Reaction, and Heat Transfer in the Combustion Chamber of a Glass Furnace," AIAA 18th Meeting on *Aerospace Sciences*, California.

Gosman, A.D., Lockwood, F.C., Megahed, I.E.A., Shah, N.G. (1982) "Prediction of the Flow, Reaction, and Heat Transfer in a Glass Furnace," *J. Energy*, Vol. 6 (6), pp. 353-360.

Gosman, A.D., Lockwood, F.C., Megahed, I.E.A., Shah, N.G. (1995) "The Prediction of the Flow, Reaction and Heat Transfer in the Combustion Chamber of a Glass Furnace," *Glass Tech*, **13**, pp. 161-167.

Hammel, J. (1986) "Some aspects of tank melting," *Advances in Ceramics*, Vol. 18, Commercial Glasses, D.C. Boyd and J.F. MacDowell, Eds., pp. 177-185, The American Ceramic Society, Columbus, OH.

Hayes, R. (1999) "Glass surface temperature and incident heat flux measurements in an industrial, regenerative gas-fired, flat-glass furnace," *M.S. Thesis*, Brigham Young University, Provo, Utah.

Hayes, R.R., Brewster, S., Webb, B.W., McQuay, M.Q., Huber, A.M. (2001) "Crown Incident Radiant Heat Flux Measurements in an Industrial, Regenerative, Gas-Fired, Flat-Glass Furnace," *Exp. Thermal Fluid Science*, Vol. 24, 2001, pp. 35-46.

Hayes, R.R., Wang, J., McQuay, M.Q., Webb, B.W., and Huber, A.M. (1999) "Predicted and measured glass surface temperature in an industrial, regenerative gas-fired, flat-glass furnace," *Glastech. Ber.* Glass Sci. Technol. 72 no. 12, pp. 367-377.

Hill, S., Smoot, L.D. (1993) "A comprehensive three-dimensional model for simulation of combustion systems: PCGC-3," *Energy and Fuels*, Vol. 7, pp.874-883.

Hill, S.C., McQuay, Newbold, J., M.Q., Webb, B.W., Bhatia, K. (1999) "Validation of numerical modeling of an industrial glass melting furnace," *J. Inst. of Energy* (in press).

Hill, S.C., Webb, B.W., McQuay, M.Q., Newbold, J. (2000) "Numerical modeling of an industrial glass melting furnace," *J. Inst. Energy* , Vol. 73, pp. 2-11.

Hoke, B.C. (1999) "Validation of CFD models for glass furnaces," *Proc. V International Seminar on Mathematical Simulation in Glass Melting*, Horni Becva (Czech Republic). pp. 16-25.

Hoogendorn, C.J., Koster, C.L., Wieringa, J.A. (1994) "Computational Modeling of Turbulent Flow, Combustion, and Heat Transfer in Glass Furnaces," *Sādhanā*, Vol. 19, pp. 723-749.

Hrma, P. (1982) "Thermodynamics of batch melting." *Glastech. Ber.*, 55, no. 7, pp. 138-150.

Hrma, P. (1988) "Complexities of batch melting," *Proc.1st Int. Conf. Advances Fusion and Processing of Glass*. Alfred, NY. pp. 10.1-10.18.

Lankhorst, A.M., Boerstoel, G.P., Muysenberg, H.P.H., Koram, K.K. (1997) "Complete simulation of the glass tank and combustion chamber of the formal Ford Nashville float furnace including melter, refiner and working end," *Proceedings of IV International Seminar on Mathematical Simulation in Glass Melting*, pp. 77-86, Horni Becva, Czech Republic.

Launder, B.E., Spalding, D.B. (1972) *Lectures in Mathematical Models of Turbulence*, Academic Press, London, UK.

Launder, B.E., Spalding, D.B. (1973) *The Numerical Computation of Turbulent Flows*, Imperial College of Science and Technology, London, UK, NTIS N74-12066.

Magnussen, B.F., Hjertager, B.H. (1976) "On mathematical models of turbulent combustion with special emphasis on soot formation and combustion," *Proceedings of 16th International Symposium on Combustion*, Cambridge, MA.

Mase, H. and Oda, K., (1980) "Mathematical Model of Glass Tank Furnace with Batch Melting Process," *J Non-Cryst Solids,* Vols. 38 and 39, pp. 807-812.

McConnell, R.R. Goodson, R.E. (1979) "Modeling of Glass Furnace Design for Improved Energy Efficiency," *Glass Tech.,* Vol. 20 (3).

McQuay, M.Q., Webb, B.W. (1996) "Internal report of an industrial float glass furnace measurement," Brigham Young University.

McQuay, M.Q., Webb, B.W., Huber, A.M. (2000) "The effect of rebuild on the combustion performance of an industrial gas-fired flat glass furnace," *Combust. Sci. Technol.*, Vol. 150, pp. 77-98.

Megahed, I.E.A. (1978) "The Prediction of Three-dimensional Gas-fired Combustion Chamber Flows," *Ph.D. Thesis*, University of London.

Newbold, J., McQuay, M.Q., Webb, B.W., Huber, A.M. (1997) "Combustion measurements in an in industrial gas-fired flat-glass furnace," *J. Inst. Energy*, Vol. 70, pp. 71-81.

Newbold, J.A. (1997) "Combustion Measurements and Modeling of an Industrial, Gas-Fired, Flat-Glass Furnace," *M.S. Thesis*, Brigham Young University, Provo, UT.

Nijnatten, P.A. van, Broekhuijse, J.T. (1999b) "A High-Temperature Optical Test Facility for Determining the Absorption of Glass at Melting Temperatures," *Proceedings of the 5th ESG Conference*, Vol. A5, pp. 51-58.

Nijnatten, P.A. van, Broekhuijse, J.T., Faber, A.J. (1999a) "Spectral Photon Conductivity of Glass at Forming and Melting Temperatures," *Proceedings of the 5th ESG Conference*, Vol. A5, pp. 2-9.

Novak, J.D. (1980) "Application of Combustion Space Energy Calculations to Commercial Glass Furnaces," *J Non-Cryst Solids*, **38** and **39**, pp. 819-824.

Patankar, S.V., (1980) *Numerical Heat Transfer and Fluid Flow*, Hemisphere, Washington, DC.
Post, L. (1988) "Modeling of Flow and Combustion in a Glass Melting Furnace," *Ph.D. Dissertation*, Delft University of Technology, Holland.

Prasad, R.S.O., Mukhopadhyay, A., Dutta, A. (1999) "Implementation of glass batch melting model in the general purpose three-dimensional CFD code FLUENT," *Proc. V International Seminar on Mathematical Simulation in Glass Melting*, Horni Becva (Czech Republic) pp. 1-9.

Raithby, G. D., Chui, E. H. (1990) "A finite-volume method for predicting a radiant heat transfer in enclosures with participating media", *J. Heat Transfer*, Vol. 112, pp. 415-423.

Rodi, W. (1984) *Turbulence Models and Their Application in Hydraulics*, Delft, The Netherlands, IAHR.

Schneppr, C., Marin, O., Champinot, C., Simon, J. (1998) "A modeling study comparing an air and an oxy/fuel fired float glass melting tank," *Proceedings of 18th International Congress on Glass*, San Francisco, USA.

Semião, V.S. (1986) "Simulação Numérica de uma Fornalha Industrial," *M.Sc. Thesis*, University of Lisbon, (in Portuguese).

Shah, N.G. (1979) "A new method of computation of radiant heat transfer in combustion chambers," *Ph.D. Thesis*, Imperial College of Science and Technology, London, UK.

Smoot, L.D. (1993) "Role of Combustion Research in the Fossil Energy Industry," *Energy & Fuels*, **7**, pp. 659-699.

Tesner, P.A., Snegiriova, T.D., Knorre, V.G. (1971) Kinetics of dispersed carbon formation, *Combustion Flame*, Vol. 17, pp. 253-271.

Twier, W. (1984) *Glass Furnaces—Design, Construction, and Operation*, Springer-Verlag.

Ungan, A. (1985) "Three-dimensional numerical modeling of the glass melting process," *Ph.D. Thesis*, Purdue University, West Lafayette, Indiana.

Ungan, A. Viskanta, R. (1986) "Melting behavior of continuously charged loose batch blankets in glass melting furnaces", *Glastech. Ber.*, Vol. 59, pp. 279-291.

Ungan, A., Viskanta, R. (1987) "Three-dimensional numerical modeling of circulation and heat transfer in a glass melting tank," *Glastech. Ber.*, Vol. 60, pp. 71-78;115-124.

Victor, A.S., Costeira, J.P., Tomé, J.A., Sentieiro, J. (1991) "A Computer Vision System for the Characterization of Flame in Glass Furnaces," *Proceedings of the 1991 IEEE Industry Applications Society Annual Meeting*, 9/28-10/4, Dearborn, MI, USA.

Viskanta, R.; Wu, X. (1983) "Effect of radiation on the melting of the glass batch," *Glastech. Ber.* 56, no. 6/7, pp. 138-147.

Wang J., Brewster, S., Webb, B. W., McQuay, M. Q. (2000b) "Validation of an improved batch model in a coupled combustion space/melt tank/batch melting furnace simulation", *Glastech. Ber.* (in press).

Wang, J. (1998) "Three-dimensional mathematical model of thermal phenomena occurring in industrial glass melting tanks," *Ph.D. Thesis*, Instituto Superior Técnico, Lisbon, Portugal.

Wang, J., Brewster, B. S., McQuay, M. Q. *et al.* (1999b) "Validation of advanced models for glass melting furnaces," *Sixtieth Conference on Glass Problems*, University of Illinois at Urbana-Champaign, October 19-20.

Wang, J., Brewster, S., Webb, B.W., McQuay, M.Q., Bhatia, K. (1999a) "A Coupled Combustion Space/Batch/Melt Tank Model for an Industrial Float Glass Furnace," *Proceedings of the 5th International Seminar on Mathematical Simulation in Glass Melting*, pp. 84-93, Horni Becva, Czech Republic, June 17-18.

Wang, J., Carvalho, M.G. (1998a) "Model-Based Study of Sand Grain Dissolution in Industrial Glass Furnaces," *Proceedings of 18th International Congress on Glass*, San Francisco, USA, July 5-10.

Wang, J., Carvalho, M.G., Nogueira, M. (1997b) "Physically-Based Numerical Tool for the Study of Glass Melt Quality," *Proceedings of IV International Seminar on Mathematical Simulation in the Glass Melting*, pp. 67-76, Vsetin, Czech, June 16-17.

Wang, J., Carvalho, M.G., Nogueira, M. (1997c) "Investigation of Glass Melting and Fining Processes by Means of Comprehensive Model," *Proceedings of Fifth International Conference on Advances in the Fusion and Processing of Glass*, Toronto, Canada, July 27-31.

Wang, J., Carvalho, M.G., Nogueira, M. (1998b) "An integrated methodology for glass furnace design," *Proceedings of 18th International Congress on Glass*, San Francisco, USA.

Wang, J., Farias, T.L., Carvalho, M.G., Nogueira, M. (1997a) "Radiation Modeling Procedures for Numerical Simulation of Glass Felting Furnaces," *Proceedings of IV International Seminar on Mathematical Simulation in the Glass Melting*, pp. 10-20, Vsetin, Czech, June 16-17.

Wang, J., Webb, B.W., McQuay, M.Q., Bhatia, K. (2000a) "Numerical simulation of an oxy/fuel-fired float glass furnace by means of a model coupling the combustion space and the glass tank," *J. Comb. Tech. Clean Env.* (in press).

Webb B.W., McQuay, M.Q., Wang, J., and Brewster, S. (1999b) "Validation of Advanced Models for Glass Melting Furnaces," *Sixtieth Conference on Glass Problems*, University of Illinois at Urbana-Chanpaign, October 19 and 20.

Webb, B.W. (1997a) "Measuring and modeling combustion in glass melting furnaces," *Proceedings of Modeling for the Glass Industry Workshop*, Alfred University.

Webb, B.W. (1997b) "Measuring and modeling combustion in glass melting furnaces," *The Glass Researcher*, Vol. 6, No. 2, pp. 16-18, Center for Glass Research, Alfred University, Alfred, New York.

Webb, B.W., McQuay, M.Q., Gera, D., Bhatia, K. (1998) "Numerical simulations on the effect of operating parameters on NO_x prediction in an industrial flat glass furnace," *Proceedings of 1998 American – Japanese Flame Research Committees International Symposium Environmental Control of Combustion Processes: Innovative Technology Towards the 21st Century*, Maui, Hawaii, USA.

Webb, B.W., McQuay, M.Q., Gera, D., Bhatia, K. (1999a) "The Effect of Operating Parameters on NO_x Production in an Industrial Flat Glass Furnace: Numerical Predictions," *Proceedings of Glass Science and Technology for the 21st Century*, Prague, Czech Republic, June 21 - 24.